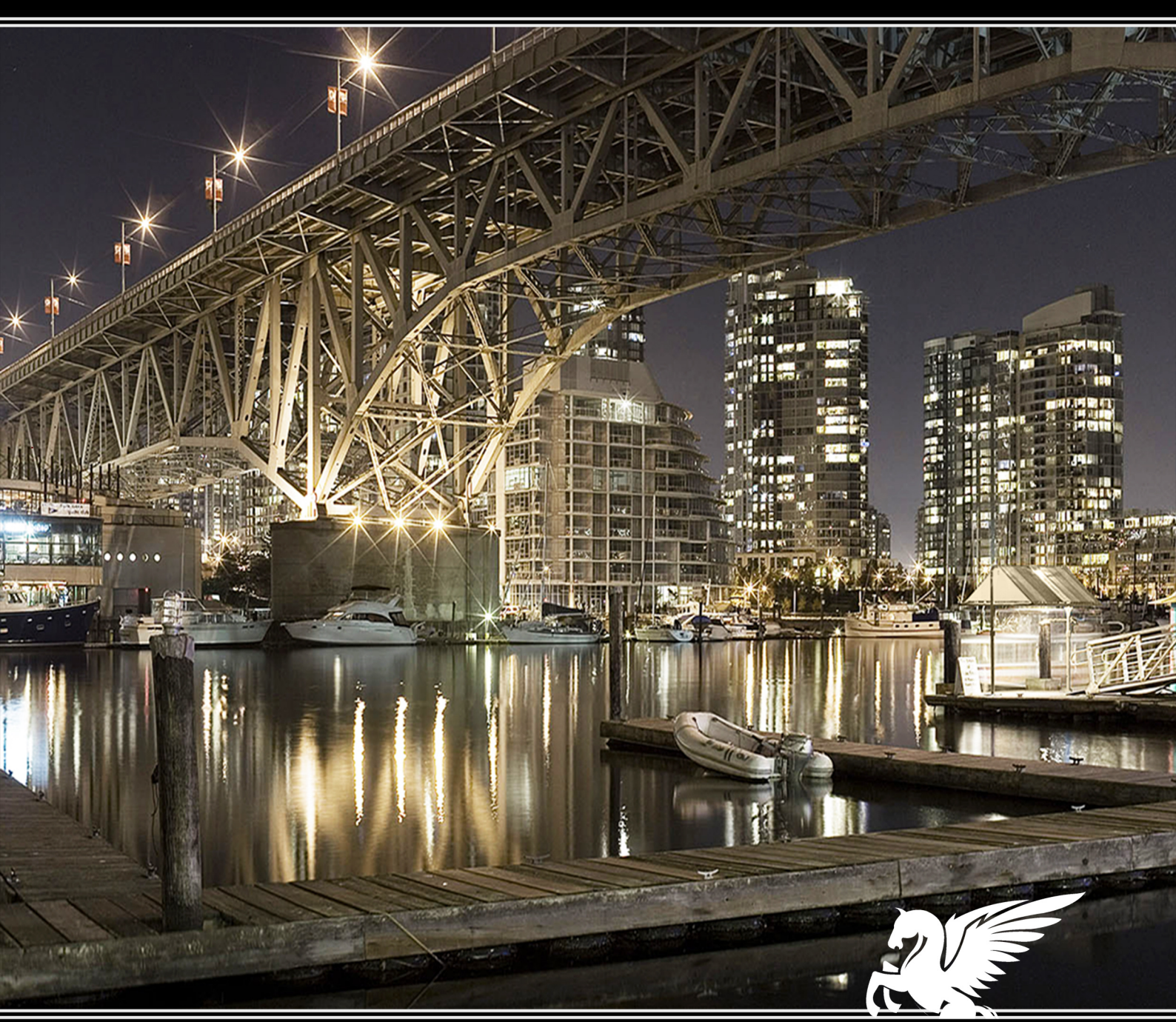
Challenge Journal of STRUCTURAL MECHANICS

Vol.1 No.4 (2015)





EDITOR IN CHIEF

Prof. Dr. Ümit UZMAN Karadeniz Technical University, Turkey

ASSOCIATE EDITOR

Prof. Dr. Yi-Lung MO
University of Houston, United States

EDITORIAL ADVISORY BOARD

Prof. Dr. A. Ghani RAZAQPUR *McMaster University, Canada*

Prof. Dr. Paulo B. LOURENÇO *University of Minho, Portugal*

Prof. Dr. Özgür EREN Eastern Mediterranean University, Cyprus

Prof. Dr. M. Asghar BHATTI University of Iowa, United States

Prof. Dr. Reza KIANOUSH Ryerson University, Canada

Assoc. Prof. Dr. Habib UYSAL Atatürk University, Turkey

Assoc. Prof. Dr. Khaled MARAR Eastern Mediterranean University, Cyprus

Assoc. Prof. Dr. Hong SHEN Shanghai Jiao Tong University, China

Assoc. Prof. Dr. Nunziante VALOROSO Parthenope University of Naples, Italy

Dr. Zühal ÖZDEMİR The University of Sheffield, United Kingdom Prof. Dr. Halil SEZEN

The Ohio State University, United States

Prof. Dr. Adem DOĞANGÜN Uludağ University, Turkey

Prof. Dr. Gilbert Rainer GILLICH

Eftimie Murgu University of Resita, Romania

Prof. Dr. Long-Yuan LI University of Plymouth, United Kingdom

Prof. Dr. Željana NIKOLIĆ University of Split, Croatia

Assoc. Prof. Dr. Filiz PİROĞLU İstanbul Technical University, Turkey

Assoc. Prof. Dr. Bing QU
California Polytechnic State University, United States

Assoc. Prof. Dr. Naida ADEMOVIĆ University of Sarajevo, Bosnia and Herzegovina

Assoc. Prof. Dr. Anna SAETTA IUAV University of Venice, Italy

Dr. Saverio SPADEA
University of Bath, United Kingdom

Dr. Hakan YALÇINER Erzincan University, Turkey

Dr. Chien-Kuo CHIU

National Taiwan University of Science and Technology, Taiwan, Province of China

Dr. Teng WU

University at Buffalo, United States

Dr. Togay ÖZBAKKALOĞLU The University of Adelaide, Australia

Dr. Fabio MAZZA
University of Calabria, Italy

Dr. Sandro CARBONARI

Marche Polytechnic University, Italy

Dr. José SANTOS University of Madeira, Portugal

> Dr. Taha IBRAHIM Benha University, Egypt

Dr. Fatih Mehmet ÖZKAL Erzincan University, Turkey

Dr. Syahril TAUFIK
Lambung Mangkurat University, Indonesia

Dr. J. Michael GRAYSON
Florida A&M University, United States

Dr. Pierfrancesco CACCIOLA University of Brighton, United Kingdom

Dr. Marco CORRADI Northumbria University, United Kingdom

Dr. Alberto Maria AVOSSA Second University of Naples, Italy

Dr. Susanta GHOSH

Duke University, United States

Dr. Amin GHANNADIASL University of Mohaghegh Ardabili, Iran

E-mail: cjsmec@challengejournal.com

Web page: cjsmec.challengejournal.com

TULPAR Academic Publishing www.tulparpublishing.com





CONTENTS

A substructure based parallel dynamic solution of large systems on homogeneous PC clusters Semih Özmen, Tunç Bahçecioğlu, Özgür Kurç	156
Dynamic analysis of pre-stressed elastic beams under moving mass using different beam models Hüseyin Bilgin	161
Evaluation of material properties by NDT methods and FEM analysis of a stone masonry arch bridge Emre Ercan, Ninel Alver, Ayhan Nuhoğlu	168
Nonlinear finite element analysis of strength and durability of reinforced concrete and composite structures	
A. Ghani Razaqpur, O. Burkan Isgor, Afshin Esfandiari	173
Resolution of torsional effects in prestressed girders of railway viaducts through use of diaphragms or proper section design	
Niyazi Özgür Bezgin	185
Dynamic vibration analysis of ballastless track: Istanbul Aksaray-Airport LRT System	
Veysel Arlı, Turgut Öztürk, Zübeyde Öztürk	192
Seismic analysis of offshore wind turbine including fluid-structure-soil interaction	
Kemal Hacıefendioğlu, Fahri Birinci	198
Effects of shape factor on the behaviour of elastomeric roadway bridge bearings and benefits of circular bearing cross section	
Niyazi Özgür Bezgin	202





A substructure based parallel dynamic solution of large systems on homogeneous PC clusters

Semih Özmen, Tunç Bahçecioğlu, Özgür Kurç*

Department of Civil Engineering, Middle East Technical University, 06531 Ankara, Turkey

ABSTRACT

This study focuses on developing a parallel solution framework for the linear dynamic analysis of large structural models on homogeneous PC clusters. The framework consists of two separate stages where the former is preparing data for the parallel solution that involves partitioning. The latter is a fully parallel finite element analysis that utilizes substructure based solution approach with direct solvers to perform implicit integration. The linear dynamic analysis of a large scale model was performed on a homogeneous PC cluster and the number of computers was varied in order to demonstrate the performance and the efficiency of the overall solution framework. The performance of the implemented framework was also compared with the widely acknowledged parallel direct solver, MUMPS.

ARTICLE INFO

Article history: Received 13 May 2015 Accepted 8 July 2015

Keywords:
Dynamic analysis
Parallel solution
Substructure
Workload balancing
PC clusters

1. Introduction

Parallel computing techniques have been implemented in many finite element codes in consequence of parallel computers becoming more available and affordable. Over the last thirty years, extensive research on parallel solution algorithms has been performed. For the time being, there are numerous parallel solution methods based on different strategies with iterative or direct solvers (Sotelino, 1993) but their performance may be limited depending on the type of the analysis, the parallel environment, and the structural properties of the system.

In many structural engineering design offices, the most readily available computer system for parallel computing is the network of PC's (PC cluster). Thus, the civil engineering industry will benefit significantly from a parallel solution framework that utilizes the existing computer system at these offices. This way, not only the time spent during the analysis will decrease but also the existing computer system will be utilized more efficiently without the need of purchasing any additional hardware.

This study focuses on developing an efficient parallel solution framework for the linear dynamic solution of large structural models on homogeneous PC clusters. Homogeneous PC clusters are composed of identical computers having the same computational characteristics. The parallel solution

is performed by a substructure based solution method (Kurç, 2008) where the substructures are condensed by a multifrontal solver and the interface equations are solved with a block-cyclic parallel dense solver (Blackford et al., 1997).

2. Method

2.1. Overview of the framework

The solution framework is composed of two main steps: data preparation and parallel solution. The aim of the data preparation step is to equalize the nodes at each substructure to balance the distribution of data among computers for the improvement of the performance of the parallel solution. Two main tasks at this stage is preparing the graph representation of the structure and then partitioning it into substructures. After the preparation of the substructures, the parallel solution is performed by a fully parallel finite element program which is capable of performing element stiffness, mass and damping matrix computations, assembly, solution, and element force computations in parallel. When the program completes the solution, it prepares the output for post-processing. All programs were developed with C++ programming language and utilized MPICH2, message passing library (MPICH2, 2010) for parallelization.

2.2. Data preparation

In order to divide the structure into substructures, graph partitioning algorithms are utilized. The objective of many existing partitioning algorithms (Hendrickson and Kolda, 2000) is to minimize the communication volume while keeping the number of nodes balanced in each substructure. The imbalances in local assembly and condensation times (local solution) can significantly decrease the efficiency of the parallel solution because the interface solution can not initiate until all local solutions are finalized. Thus, the time spent during the local solution step is governed by the substructure with the slowest assembly and condensation time. By partitioning the substructures with equal nodes in each substructure, it was expected that the imbalance among the local solution times would decrease and as a result the time spent during the parallel solution decreased.

The data preparation algorithm first partitions the structure into 'p' substructures where 'p' is equal to the number of available computers after preparing the nodal graph representation of the structural model. Partitioning is performed by recursive partitioning algorithm of METIS (Karypis and Kumar, 1998), a multilevel graph partitioning library. The data is prepared for the parallel solution. The node and element definitions of the substructures are created using the structural and the selected partitioning information. During that process, the interface elements, whose nodes are on two or more substructures, are assigned to one of their adjacent substructure.

Then, each computer orders the equations of their substructures utilizing MSMD ordering algorithm (Liu, 1989) to optimize the solution. MSMD algorithm numbers the vertices by stages, in other words, the vertices belonging to stage i are numbered before the vertices belonging stage i+1. Thus, during numbering, the internal and interface vertices are assigned to stages 0 and 1, respectively.

2.3. Parallel solution

2.3.1. Overview

Implicit Newmark method (Newmark, 1959) is a numerical integration method presented by Newmark for the solution of dynamic structural problems. The equation of motion that represents a dynamic structural system can be written as

$$[M]\{\ddot{U}\}_n + [C]\{\dot{U}\}_n + \{R^{int}\}_n = \{R^{ext}\}_n,$$
 (1)

where for linear systems,

$${R^{int}}_n = [K]{U}_n.$$
 (2)

Implicit Newmark method is implicit as the solution of $\{U\}_{n+1}$ depends on variables both at time n+1 and n whereas in explicit methods solution of $\{U\}_{n+1}$ depends on only variables at time t. The general formulation of Implicit Newmark method (Wilson, 1962) can be written as

$$\begin{split} & \left[\overline{K}\right]\{U\}_{n+1} = \left\{R^{ext}\right\}_{n+1} + \left[M\right] \left\{\frac{1}{\beta \Delta t^2} \{U\}_n + \frac{1}{\beta \Delta t} \left\{\dot{U}\right\}_n + \left(\frac{1}{2\beta} - 1\right) \left\{\ddot{U}\right\}_n\right\} + \left[C\right] \left\{\frac{\gamma}{\beta \Delta t} \{U\}_n + \left(\frac{\gamma}{\beta} - 1\right) \left\{\dot{U}\right\}_n + \left(\frac{\gamma}{2\beta} - 1\right) \left\{\ddot{U}\right\}_n\right\}, \ (3) \end{split}$$

where

$$\overline{[K]} = \frac{1}{\beta \Delta t^2} [M] + \frac{\gamma}{\beta \Delta t} [C] + [K]. \tag{4}$$

As $[\overline{K}]$ involves the stiffness matrix it cannot be a diagonal matrix. Thus full factorization of $[\overline{K}]$ is needed to solve Eq. (3). For linear systems $[\overline{K}]$ matrix can be factorized once and then repeatedly solved for each time step. It can be shown (Hughes, 1983) that Implicit Newmark method is unconditionally stable when $2\beta \geq \gamma \geq 1/2$. In this study $\gamma=1/2$ and $\beta=1/4$ values are used.

2.3.2. Implementation

The parallel solution initiates by creating separate data structures at each computer from the input file prepared by the data preparation program. Then, each computer assigns degrees of freedom to its nodes. The nodes of each substructure were written into the input file according to their optimized order. Hence, during the assignment process, each node is visited one by one and the nodes' active degrees of freedom are numbered consecutively. After that, stiffness and force vectors are assembled.

Besides the global stiffness matrix and load vector, mass and damping matrices shall be assembled prior to the initialization of repetitive solution by the implicit Newmark integration algorithm. These matrices are assembled at the element level to minimize the in-core memory consumption. Stiffness and mass matrices of every finite element of the structural model are computed and assembled to global matrices. Elemental mass matrices can be either lumped or consistent according to the model needs. The damping matrix is computed as a linear combination of the elemental stiffness and elemental mass matrices according to the Rayleigh damping method (Rayleigh, 1894).

Due to the nature of linear dynamic solution, the [K] matrix is factorized once and then this system is solved repeatedly at each time step. Factorization of $[\overline{K}]$ matrix consists of two steps as; condensation and interface system factorization. The first step of the factorization is static condensation of each substructure which means that contributions from internal nodes are reflected to the interface nodes. The condensations are performed by using a parallel direct solver, MUMPS (Amestoy et al., 2000) which performs LDL^T factorization of positive definite symmetric matrices. Up to this point, neither communication nor synchronization among computers is required.

As a second step; the interface stiffness matrix is assembled, where each computer sends and receives some portion of the interface stiffness matrix. In order to utilize the parallel dense matrix solver of ScaLAPACK library (Blackford et al., 1997), the interface matrix is distributed as 2D rectangular blocks in a cyclic manner. First each computer prepares a data distribution scheme

and data buffers that involves the parts of the matrix that will be sent to a particular computer. Then, the data transfer initiates in such a way that none of the computers stays idle. As the distribution of the interface stiffness matrix is finalized, it is factorized by utilizing parallel LDL^T factorization method.

Similarly, right hand side of the Eq. (3) is computed in substructure level, condensed to interface nodes and then it is re-assembled to form interface system load vector. At each time step interface system load vector is computed and then it is solved with the factorized interface system matrix and the displacements at interface level are obtained. By recovering the interface displacements back to substructure level, right hand side vector can be computed for the next time step. In this manner, algorithm continues until the last time step reached. In addition to the nodal displacements, at each time step, the forces and the stresses for each element in a substructure can be computed.

3. Results and Discussions

The efficiency of the presented framework was tested on the homogeneous PC cluster composed of eight computers with identical hardware. The cluster is composed of eight Intel Core2Quad Q9300@2.5 GHz processors and 3.23 GB RAMs. Intel Core2Quad family processors involve four processors that are working at 2.5 GHz and are able to share the memory. However, this feature of this cluster is not utilized during these tests. All computers were running Windows XP and were connected with an ordinary 1 GBit network switch.

2D square mesh is a mathematical model having 40000 quadrilateral shell elements (Fig. 1) with 40401 nodes and \sim 130000 equations. Dynamic loading is applied to the system at certain time steps and behaviour is monitored for 20 seconds with 0.02 seconds intervals.

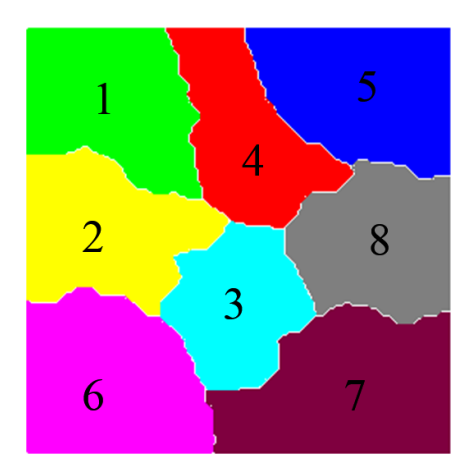


Fig. 1. 2D square mesh model with a sample partitioning among computers.

Fig. 2 presents the substructure assembly, dynamic system matrix factorization and back substitution timings for the dynamic solution of the test model by utilizing 1, 2, 4, 6 and 8 computers for FEMLib solver and MUMPS solver, respectively.

For both solution methods, substructure assembly timings are decreasing almost in the same order of the increase in number of computers utilized. For example, while assembly timing for a single computer was 94.6 seconds, this timing dropped to 46.1 seconds and 24.3 seconds for the solution with FEMLib by two and four computers, respectively. This is certainly expected due to the fact that the number of elements for each substructure is decreasing almost in the same order.

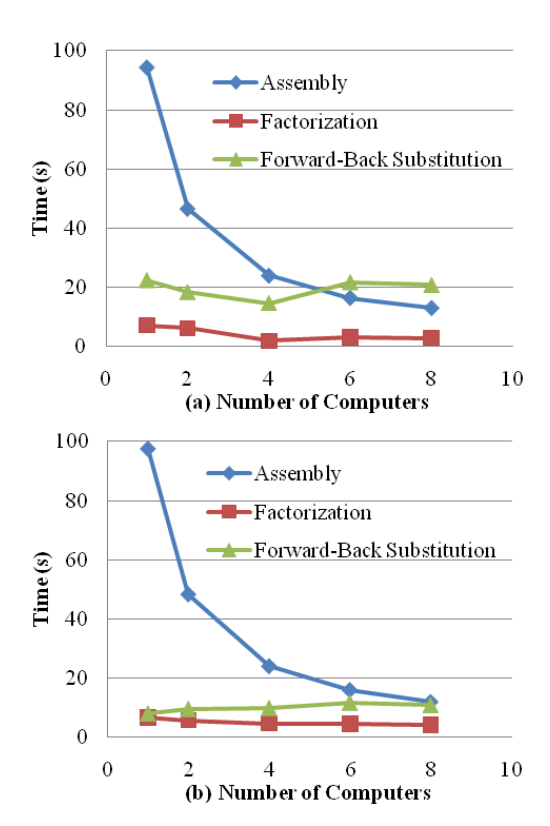


Fig. 2. Timings of main stages for FEMLib (a) and MUMPS (b) solvers.

Factorization stage, although it was one of the most time consuming stage for a static solution, was not a governing factor in dynamic solution, because it was computed only once compared to the forward and back substitutions for a thousand time-steps. Fig. 2, verifies this fact and also reveals a mild decrease in factorization stage with the increasing number of computers. When the timings of FEMLib and MUMPS solvers are compared, obviously the forward and back substitution stages were faster in the latter one. For solution by eight computers, back substitution for thousand iterations was computed by FEMLib in 20.1 seconds. However, the same computation was done by MUMPS in 10.8 seconds.

Fig. 3 illustrates the timings of different steps of dynamic system matrix factorization and those of dynamic system solution with FEMLib solver, respectively, for the various numbers of computers. For both, obviously condensation is decreasing as the number of computers utilized increase. On the contrary, interface assembly, interface factorization, load assembly and interface solution timings are gradually increasing. This behaviour is expected because the number of interface nodes is increasing with the increase in the number of substructures.

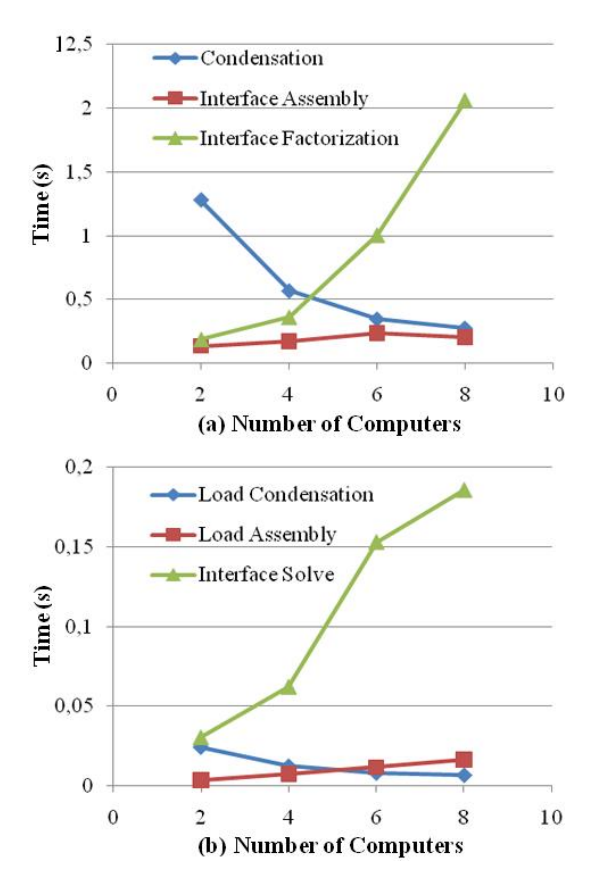


Fig. 3. Timings of factorization (a) and forward - back substitution (b) for FEMLib.

Assembly of the interface matrix and load vector increase as the number of computers increase because more communication is required among the computers to assemble a bigger system. These detailed timings are conclude the fact that by increasing the substructure size one can gain from condensation timings, but should lose from assembly and factorization because of the increasing interface system size.

Fig. 4 presents the total dynamic solution timings of the test model (a) and the speed-up values obtained (b) by utilizing 2, 4, 6 and 8 computers for FEMLib solver and MUMPS solver, respectively.

The dynamic solution by utilizing single computer completed in 123.1 seconds and 112.8 seconds for FEM-Lib and MUMPS solvers, respectively. From the previous figures it was revealed that this difference is mainly because the difference during the back substitution stage. By utilizing two, four and eight computers in parallel, the dynamic solution timings reduced to 71.0 seconds, 43.6 seconds and 35.9 seconds, respectively. Speed-up value which is the fraction of parallel solution timings to single computer solution timings are also given in Fig. 4(b). For the solution with two, four, six and eight computers, speed-up values 1.74, 3.06, 2.90 and 3.48 were obtained. Thus, although the speed-up values for two and four computers are close to theoretical values of 2.0 and 4.0, speed-up values for the six and eight computers are half of the theoretical values of 6.0 and 8.0. Because when the number of substructures is increased, interface system size is increasing.

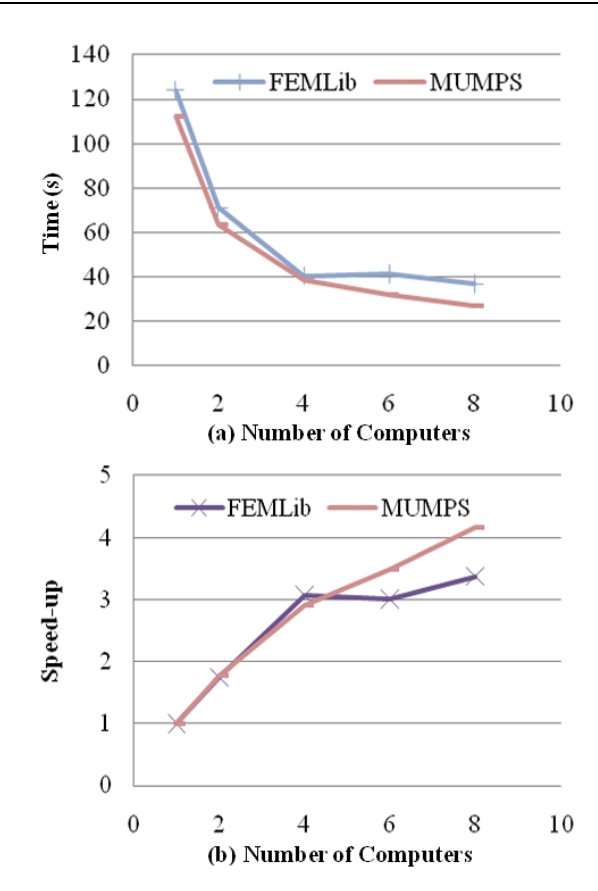


Fig. 4. Total Timings (a) and Speed-ups (b) for FEMLib and MUMPS solvers.

4. Conclusions

This study presented a parallel solution framework for the linear dynamic analysis of large structures on homogeneous PC clusters. For the example problem considered, the presented method achieved almost comparative results to widely acknowledged parallel direct solver, MUMPS. Furthermore, the total solution time decreased as the number of computers increased. Thus, this framework is very efficient and can be utilized to solve large problems on cheap and ordinary PC clusters of homogeneous type.

Acknowledgements

Funding provided by TÜBİTAK under grant number 108M586 is gratefully acknowledged.

REFERENCES

Amestoy PR, Du IS, Koster J (2000). MUMPS: A general purpose distributed memory sparse solver. *In Proceedings of PARA2000, 5th International Workshop on Applied Parallel Computing,* 122-131.

Blackford LS, Choi J, Cleary A, D'Azeuedo E, Demmel J, Dhillon I, Hammarling S, Henry G, Petitet A, Stanley K, Walker D, Whaley RC (1997). ScaLAPACK User's Guide, Society for Industrial and Applied Mathematics, USA.

Hendrickson B, Kolda TG (2000). Graph partitioning models for parallel computing. *Parallel Computing*, 26, 1519-1534.

- Hughes TJR (1983). Analysis of transient algorithms with particular reference to stability behaviour. *Computational Methods for Transient Analysis*, T. Belytschko and T.J.R. Hughes, eds., pp. 67-155.
- Karypis G, Kumar V (1998). METIS: A software package for partitioning unstructured graphs, partitioning meshes, and computing fill-reducing orderings of sparse matrices, version 4.0.
- Kurc O (2008). Parallel Computing in Structural Engineering. VDM Verlag, Germany.
- Liu JWH (1989). On the minimum degree ordering with constraints. SIAM Journal on Scientific Computing, 10, 1136-1145.
- MPICH2 Library (2010). Message Passing Interface Standard v2.0 retrieved from http://www-unix.mcs.anl.gov/mpi.
- Newmark NM (1959). A method of computation for structural dynamics. *ASCE Journal of the Engineering Mechanics Division*, 85, No. EM3.
- Rayleigh JWS (1894). The theory of sound. 2nd ed. (reprinted by Dover Publications, New York, 1945), vol. I, pp. 102, vol. II, pp. 312.
- Sotelino ED (2003). Parallel processing techniques in structural engineering applications. ASCE Journal of Structural Engineering, 29(12), 1698-1706.
- Wilson E (1962). Dynamic response by step-by-step matrix analysis. *Proceedings, Symposium on the Use of Computers in Civil Engineering,* Labortotio Nacional de Engenharia Civil, Lisbon, Portugal.



Seismic performance evaluation of an existing school building in Turkey

Hüseyin Bilgin*

Department of Civil Engineering, Epoka University, 1039 Tirana, Albania

ABSTRACT

A great part of existing RC structures built in Turkey is that they have been designed without considering seismic-induced actions and seismic criteria for strength and ductility design. In this context, after the recent devastating earthquakes in Turkey, there has been a concerted effort to address the seismic vulnerability of existing public buildings in Turkey. The need for the evaluation and strengthening of these public buildings have come into focus following the enormous loss of lives and property during the past earthquakes. This study aims to assess the seismic performance evaluation of a typical school building in accordance with the rules of Turkish Earthquake Code-2007. The performance analysis is carried out by using nonlinear static analysis. The analytical solutions show that the intended performance level has not been satisfied for this building and decided to retrofit the structural system. The proposed procedure is applied to the retrofitted system and the obtained results are tabulated and discussed.

ARTICLE INFO

Article history: Received 11 May 2015 Accepted 2 July 2015

Keywords:
Public buildings
Performance evaluation
Pushover analysis
Retrofit

1. Introduction

Earthquakes are of concern to cities in Turkey. Because many existing structures in this region are inadequate based on the current seismic design codes, it is important to assess these structures and improve the seismic resistance of systems that are found to be vulnerable. In general, buildings designed without seismic considerations have significant deficiencies such as discontinuity of positive moment reinforcement in beams and wide spacing stirrups. Besides the design deficiencies poor quality material and workmanship are the other important factors.

The projects and the construction of existing public buildings that were built before 1998, were constructed in accordance with the regulations Turkish Building Code-1984, (TBC-1984) and Turkish Earthquake Code, (TEC-1975), which were in effect at that time. However, the earthquake and the construction regulations underwent significant changes with the revisions made in 1998, 2000 and 2007 (TEC-1998, TBC-2000, TEC-2007). The strengthening of existing public buildings in conjunction with new contract specifications, thereby reducing loses of life and property to a minimum in case of an earthquake has become one of the most important

issues on the agenda of Turkish Government. In addition, a number of major earthquakes during the last two decades have underlined the importance of mitigation to reduce seismic risk.

Seismic strengthening of existing structures is one method to reduce the risk to vulnerable structures. Recently, a significant amount of research has been devoted to the study of various retrofit techniques to enhance the seismic performance of RC structures (ASCE/SEI 41-06, Eurocode 8, FEMA 356, and FEMA 440). However, few studies have been conducted to assess the seismic performance of representative concrete structures in Turkey using the criteria of Turkish Earthquake Code-2007 (TEC-2007).

The accepted analysis procedures in the analysis include two types of linear elastic methods: equivalent lateral force analysis and modal response spectrum analysis, and two type of nonlinear methods: pushover analysis, and non-linear time history analysis. Since force based approaches have some shortcomings for seismic evaluation, displacement based design procedures are used. Linear-elastic methods have some shortcomings, since they aimed to provide a conservative estimate of building performance during an earthquake. Response of buildings to earthquakes is not typically linear; hence

convenient nonlinear analysis methods should provide a good representation of buildings' response and performance. When nonlinear methods are used, since performance limits on permissible response are less-conservative than the linear elastic ones, lower construction costs may be fulfilled. Structural performance of the existing buildings are determined by applying nonlinear static procedures defined in most earthquake design codes; ATC-40, FEMA-356, Turkish Earthquake Code-2007 (TEC-2007).

2. Turkish Earthquake Codes

The earthquake resistance consideration for building design in Turkey has a history of more than fifty years. Beginning as legal provision in mid 1940's after a series of destroying earthquakes, Turkey's earthquake code is developed to its present state in 2007 after a number of evolutionary revisions respectively in 1959, 1975, 1998. The final version of the code includes regulations on repairing and retrofitting existing buildings (Chapter 7). Chapter 7 of TEC-2007 has many similarities to the new modern codes (ATC-40, FEMA-356, Eurocode 8, etc) consists of linear and nonlinear methods to evaluate the seismic performance of existing buildings.

3. Structural Properties of the Analyzed School Building

Schools likewise the other buildings intended for governmental services are generally constructed by applying

template designs developed by the Ministry of Public Works. Therefore, a considerable number of buildings have the same template designs in different parts of Turkey.

A field survey was carried out in the western part of Turkey to select the most common types of school buildings. These cities are located in a seismically active part of Turkey. According to the survey, a most common type of template design (TD-10419) for school buildings was selected to represent these public buildings in medium-sized cities.

This is a four-story school building with a plan area of 613 square meters at the base. All floor slabs are reinforced concrete with a thickness of 0.2 m. The story heights are 3.4 m for each story. There exists no exact data about the roofing and the masonry partitions of the building. From the architectural drawing plotted at the time of construction, reasonable values are assumed for both in dead load and other calculations, considering probable changes made during the construction.

The building has a typical structural system, which consists of reinforced concrete frames with masonry infill walls of hollow clay brick units. The structural system is free of shear walls in longitudinal direction and composed of shear wall-frame system in transverse direction. There are no structural irregularities such as soft story, weak story, heavy overhangs, great eccentricities between mass and stiffness centers. One of the possible deficiencies for this building designed per TEC-1975 is the strong beam-weak column behavior as it is not regarded by that code. Fig. 1 and Fig. 2 provide a typical floor plan and 3-D view of this case study structure respectively.

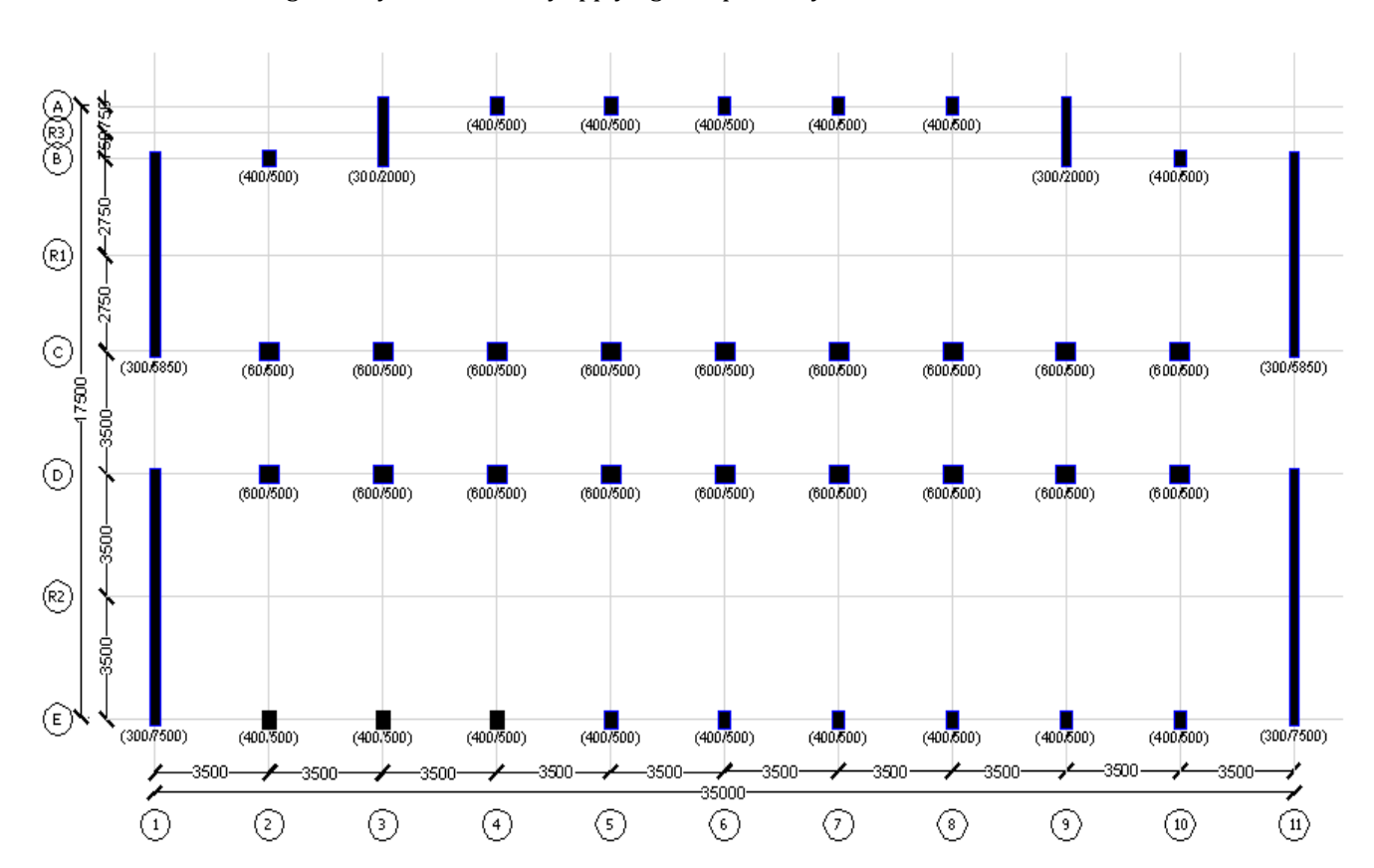


Fig. 1. Typical structural floor plan view of the TD-10419 building.

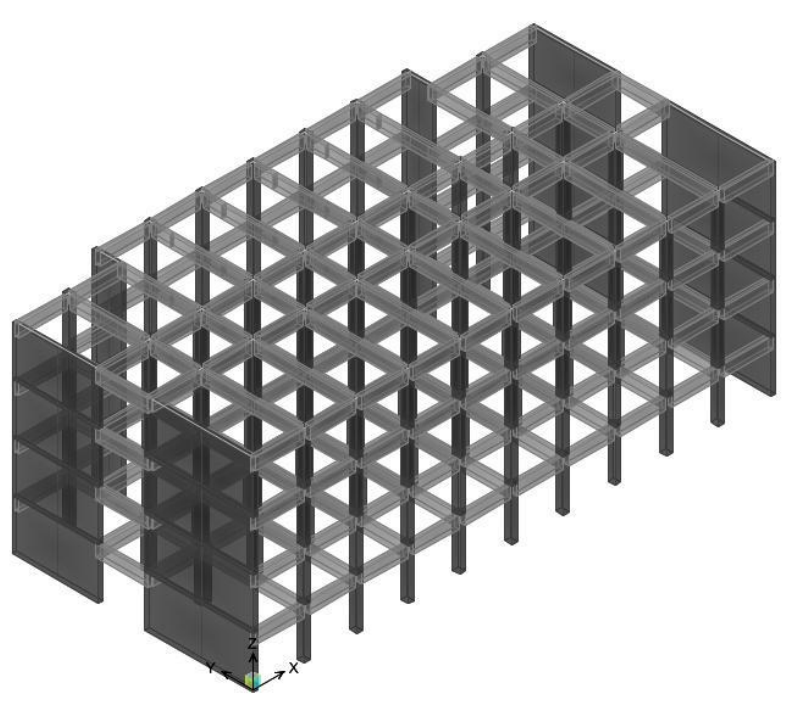


Fig. 2. Three dimensional view of the TD-10419 building.

4. Analytical Modeling of the School Building

4.1. Analytical modeling

SAP2000 (CSI, 2003) is employed for the modeling and analysis of the structure. The building is modeled as 3-D frame-shear wall system formed by beams, columns and shear walls. The joints connecting the base columns and shear walls to the foundation are restrained for all degrees of freedom. The calculation of the masses, dead and live loads are made according to the Turkish Standards for Reinforced Concrete (TBC-2000), Turkish Standards for Design Loads (TS-498) and TEC-1975.

For nonlinear analysis, as-built material properties determined from field investigation and experiment are taken into account. Modeling properties of the investigated building is tabulated in Table 1.

Table 1. Structural properties of the investigated building.

	TD10419
Number of stories	4
Story height (m)	3.4
Floor area (m²)	612.5
Total building weight (t)	3323
Concrete Class	C10, C16
Steel Grade	S220
Stirrup spacing at the plastic hinge locations (mm)	150 and 250
X- period (s)	0.54
Y- period (s)	0.24
Mass participation ratios in x- and y-, respectively	0.86 - 0.75

4.2. Determination of nonlinear parameters

Member size and reinforcements in the template design are used to model the school building for nonlinear analysis. The structural modelling is carried out with the beam, column and shear wall elements, considering the nonlinear behaviour concentrated in plastic hinges at both ends of beams and columns. SAP2000 provides default or the user-defined hinge properties options to model nonlinear behaviour of components. In this study, user-defined hinge properties are used.

The definition of user-defined hinge properties requires moment-curvature relationships for beams and columns and axial force moment capacity data for the columns are necessary for the SAP2000 input as nonlinear properties of elements (Fig. 3).

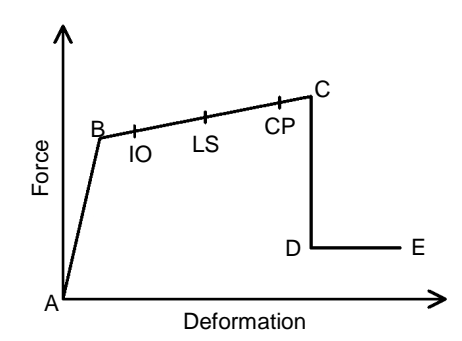


Fig. 3. Typical force deformation relationship.

Mander model (Mander el al., 1988) is used for unconfined and confined concrete while typical steel stress-strain model with strain hardening for steel is implemented in moment-curvature analyses. The input required for SAP2000 is moment-rotation relationship instead of moment-curvature. Also, moment rotation data

have been reduced to five-point input that brings some inevitable simplifications. Plastic hinge length is used to obtain ultimate rotation values from the ultimate curvatures. Plastic hinge length definition given in Eq. (1) which is proposed by Priestley et al. (1996) is used in this study.

$$L_p = 0.008L + 0.022f_{ve}d_{bl} \ge 0.044f_{ve}d_{bl}. \tag{1}$$

In Eq. (1), L_p is the plastic hinge length, L is the distance from the critical section of the plastic hinge to the point of contraflexure, f_{ye} and d_{bl} are the expected yield strength and the diameter of longitudinal reinforcement.

In existing reinforced concrete buildings, especially with low concrete strength and insufficient amount of transverse steel, shear failures of members should be taken into consideration. For this purpose, shear hinges are introduced for beams and columns. Shear hinge properties are defined such that when the shear force in the member reaches its shear strength, member immediately fails. The shear strength of each member (V_r) is calculated according to TBC-2000.

$$V_r = 0.182bd\sqrt{f_c} + \left(1 + 0.07\frac{N}{A_c}\right) + \frac{A_{sh}f_{yhd}}{S}.$$
 (2)

In Eq. (2), b is section width, d is effective section depth, f_c is concrete compressive strength, N is compression force on section, A_c is area of section, A_{sh} , f_{yh} and s are area, yield strength and spacing of transverse reinforcement.

5. Performance Evaluation of the School Building by Using Pushover Analysis

In order to apply this method, TEC-2007 requires some limitations on the building height ad torsional irregularity and the mass participation ratios for the first mode. Pursuant to TEC-2007, mass participation ratios must be greater than 70%. For the addressed building, this value is 86% in *x*-direction more than proposed.

The pushover analysis consists of the application of gravity loads and a lateral load pattern. The applied lateral forces are proportional to the product of mass and the first mode shape amplitude at each story level and P- Δ effects are taken into account.

In the capacity curve plots, base shear is normalized by building seismic weight on the vertical axis, while global displacement drift is normalized by building height on the horizontal axis. Capacity curves of the school building is obtained for different concrete strength and transverse reinforcement spacing mentioned in previous section; two concrete strength and two transverse reinforcement spacing values are taken into account.

Two extreme cases are considered in order to have a more accurate understanding in the boundaries of behavior for the case study building with the considered template design. The first one represents the buildings in poor condition having poor concrete quality (10 MPa) with non-ductile detailing (250 mm transverse rein-

forcement spacing). The second one refers to the buildings in average condition having average concrete quality (16 MPa) with ductile detailing (150 mm transverse reinforcement spacing). Capacity curves corresponding to poor and average conditions are illustrated in Fig. 4 for longitudinal (x) and transverse (y) directions.

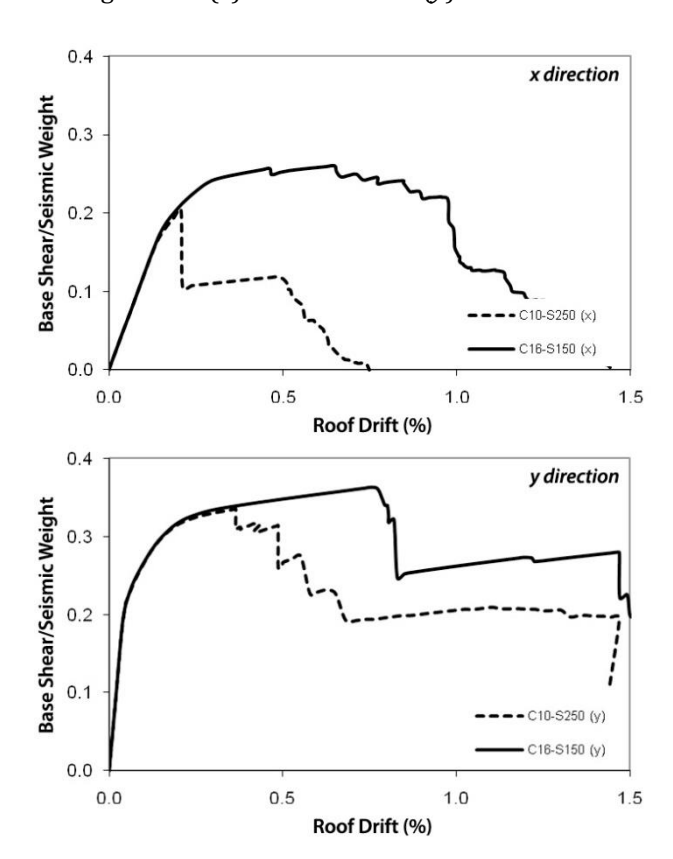


Fig. 4. Capacity curves of the building TD-10419 for different concrete strength and transverse reinforcement spacing obtained by pushover analysis.

Evaluation of the capacity curves for the investigated building points out that concrete quality and detailing has significant role in both displacement and lateral strength capacity of buildings. The displacement capacity for the average condition is more than twice of that for poor condition.

5.1. Performance evaluation according to TEC-2007

Capacity assessment of the investigated school building is performed using TEC-2007. Three performance levels, immediate occupancy (IO), life safety (LS), and collapse prevention (CP) are considered as specified in this code and several other international guidelines such as FEMA-356, ATC-40, and FEMA-440.

Pushover analysis data and criteria of TEC-2007 are used to determine global displacement drift ratio of each building corresponding to the performance levels considered. Table 2 lists global displacement drift ratios of the building. Small displacement capacities at LS and CP performance levels are remarkable for the building with poor concrete quality and less amount of transverse reinforcement due to shear failures in columns (C10-S250).

The displacement capacity values are solely not meaningful themselves. They need to be compared with demand values. According to the Turkish Earthquake Code, school buildings are expected to satisfy IO and LS performance levels under design and extreme earthquakes, corresponding to 10% and 2% probability of exceedance in 50 years, respectively. Response spectrum for the design and extreme earthquakes is plotted in Fig. 5 for high seismicity region and soil class Z3. Displacement demand estimates and capacities corresponding to IO and LS performance levels are compared.

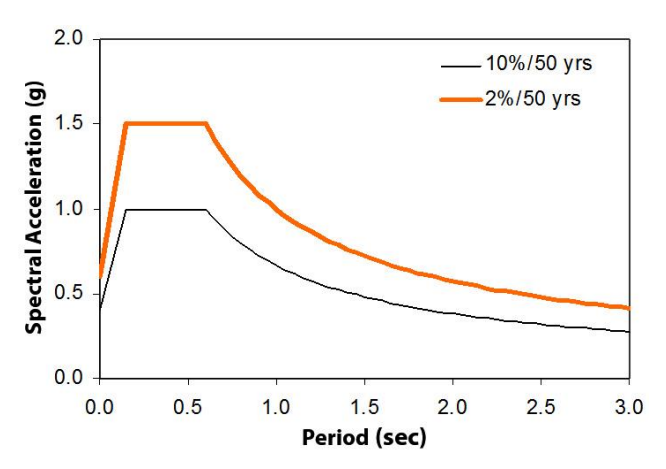


Fig. 5. Response spectrum for design and extreme earthquake events provided in TEC-2007.

Displacement demand estimates are obtained (Table 3) as described in TEC-2007. The results obtained show

that school building does not provide IO in both directions whereas LS performance level is satisfied in *y*- direction which means that the structural system should be strengthened.

5.2. Performance evaluation according to TEC-2007

As it is seen that existing structural system of the school building does not satisfy the expected performance levels and it is decided to strength the structural system. For strengthening, shear walls are added to the existing structural system of the building. Six in x- direction and one in y- shear walls are added to the existing structural system (Fig. 6). The material classes for reinforced concrete shear walls are considered to be C25 (f_{ck} =25 MPa) and S420 (f_{yk} =420 MPa).

The 3-D model of the new system is analyzed by SAP2000. The first and second mode periods in *x*- and *y*-directions are found to be 0.28 s and 0.19 s, respectively. As it is seen that the while the stiffness increases, fundamental vibration period decreases. Similar performance evaluation procedure for existing structural system is repeated for new system. Pushover curves for the new and existing are given in Fig. 7.

Capacity assessment and seismic displacement demand calculations are repeated for the new structural system according to TEC-2007 and the results are tabulated in Table 4.

Obtained results show that strengthened school building satisfies IO performance levels under the design earthquake and provides LS performance level under maximum earthquake.

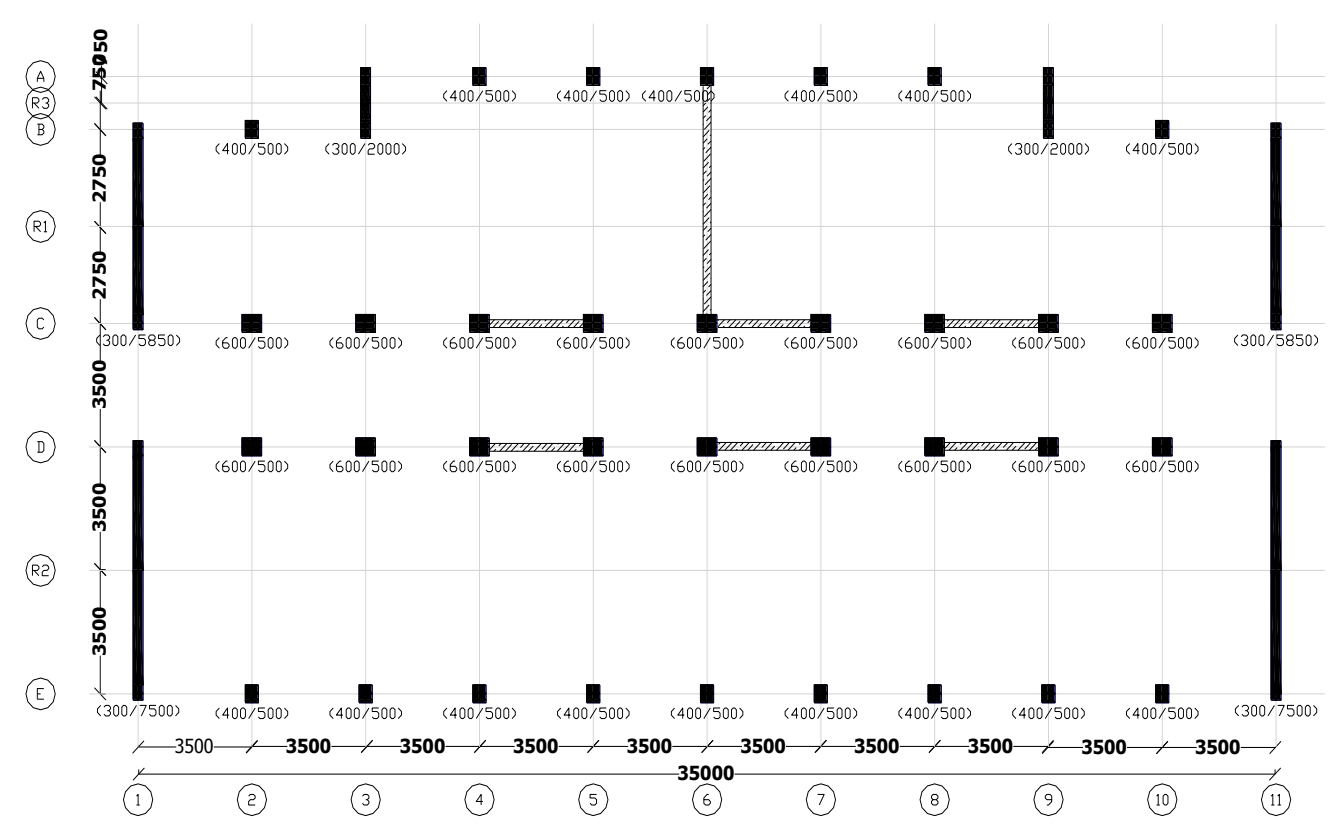


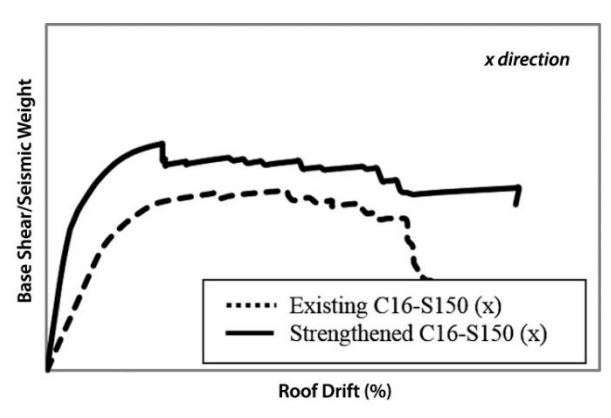
Fig. 6. Structural floor plan view of strengthened TD-10419 building.

Table 2. Global displacement drift capacities (%) of the investigated building obtained from capacity curves for considered performance levels.

		$\Delta_{ m roof}/I$	$\mathcal{H}_{ ext{building}}$	
Material Quality	x-dire	x-direction		ection
	Ю	LS	IO	LS
C10-S150	0.16	0.40	0.16	0.47
C10-S250	0.16	0.19	0.14	0.36
C16-S150	0.19	0.52	0.23	0.55
C16-S250	0.17	0.25	0.21	0.51

Table 3. Global demand drift ratios (%) of the investigated building according to TEC-2007.

$\Delta_{ m roof}/H_{ m building}$				
x-dire	ection	<i>y</i> -dire	ection	
Ю	LS	10	LS	
0.76	1.15	0.28	0.46	



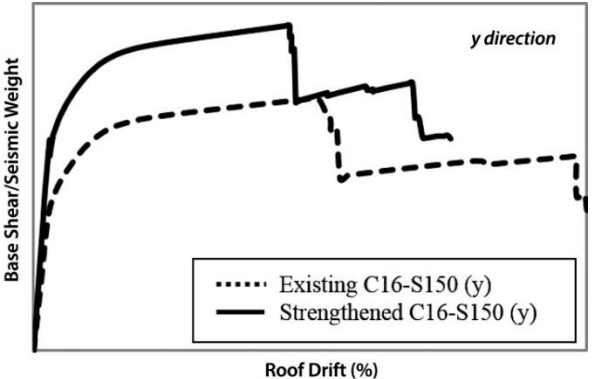


Fig. 7. Capacity curves of the strengthened school building obtained by pushover analysis.

Table 4. Comparison of global displacement drift capacities and global drift demand ratios of the investigated school building for considered performance levels according to TBC-2007(%).

				$\Delta_{ m roof}/c$	Houilding			
Material	x-direction				<i>y</i> -dire	ection		
Quality	I)	L	S	10)	L	S
	Demand	Capacity	Demand	Capacity	Demand	Capacity	Demand	Capacity
C10-S250	0.38	0.38	0.60	0.97	0.21	0.24	0.36	0.36
C16-S150	0.36	0.37	0.59	1.05	0.20	0.27	0.35	0.38

6. Conclusions

In this study, seismic performance assessment of an existing school building with the selected template design is studied according to TEC-2007. SAP2000 is employed for modeling and analyzing of the building. Existing structural system is evaluated by nonlinear methods to evaluate the performance levels. Analytical solutions have shown that the structural system of the school building does not satisfy the intended criteria in TEC-2007. To strengthen the structural system, shear walls are added in x- and y- directions. In order to find the economical solution for the new strengthening system, nonlinear analyses are repeated with different number of shear wall options. Performance evaluation for each analyses result has been done for the new system and the most appropriate strengthened system is proposed. The following conclusions can be drawn from numerical results:

- Based upon site investigation and laboratory test results; two strength values, 10 and 16 MPa, are considered for concrete and Grade 220 considered for reinforcement in this study.
- Two stirrup spacing values are considered as 150 and 250 mm to reflect ductile and non-ductile detailing, respectively.
- Evaluation of the capacity curves for the investigated building points out that concrete quality and detailing has significant role in displacement and lateral strength capacity of buildings in both directions. Although the difference of poor (C10 and s250) and average (C16 and s150) conditions on lateral strength capacity is limited, the difference in displacement capacity is noteworthy.
- Shear failures of columns are common problems in case of poor concrete and low amount of transverse reinforcement, resulting in brittle failure for existing school buildings.

- As material quality gets better, performance of buildings improves. The displacement capacities obtained for different performance levels evidently indicates that concrete quality and transverse reinforcement spacing have limited effect on IO level while amount of transverse reinforcement plays an important role in seismic performance of buildings for LS level.
- According to TEC-2007, school buildings are expected to satisfy IO and LS performance levels under design and extreme earthquakes. The existing school building is far from satisfying the expected performance levels; therefore it is strengthened by adding shear walls in both directions. After retrofitting desired performance levels are provided in both directions.
- Addition of shear walls increases lateral load capacity and decreases displacement demands significantly. Thus, existing deficiencies in frame elements are less pronounced and poor construction quality in buildings is somehow compensated (Bilgin, 2007).

REFERENCES

- ASCE/SEI 41-06 (2007). Seismic Rehabilitation of Existing Buildings. American Society of Civil Engineers, Reston, VA, USA.
- ATC-40 (1996). Seismic Evaluation and Retrofit of Concrete Buildings (Volume 1-2). Applied Technology Council, Redwood City, CA, USA. Bilgin H (2007). Seismic Performance Evaluation of Public Buildings Using Non-Linear Analysis Procedures and Solution Methods. *Ph.D. thesis*, Pamukkale University, Turkey.

- Eurocode-8 (2005). Design of Structures for Earthquake Resistance Part 3: Assessment and Retrofitting of Buildings. European Committee for Standardization, Brussels, Belgium.
- FEMA-273 (1997). NEHRP Guidelines for the Seismic Rehabilitation of Buildings. American Society of Civil Engineers, Federal Emergency Management Agency, Washington, USA.
- FEMA-356 (2000). Prestandard and Commentary for the Seismic Rehabilitation of Buildings. American Society of Civil Engineers, Federal Emergency Management Agency, Washington, USA.
- FEMA-440 (2005). Improvement of Nonlinear Static Seismic Procedures. American Society of Civil Engineers, Federal emergency management agency, Washington, USA.
- Mander JB, Priestly MJN, Park R (1988). Theoretical stress-strain model for confined concrete. ASCE Journal of Structural Division, 114(8), 1804-1826.
- Priestley MJN, Seible F, Calvi GMS (1996). Seismic Design and Retrofit of Bridges. John Wiley & Sons, New York.
- SAP2000 (2003). Integrated Finite Element Analysis and Design of Structures. Computers and Structures Inc., Berkeley, California.
- TBC-1984 (1984). Requirements for Design and Construction of Reinforced Concrete Structures. Ankara, Turkey.
- TBC-500 (2000). Requirements for Design and Construction of Reinforced Concrete Structures. Ankara, Turkey.
- TEC-1975 (1975). Regulations on Structures Constructed in Disaster Regions. Ministry of Public Works and Settlement, Ankara, Turkev.
- TEC-1998 (1998). Specifications for Structures to be built in Disaster Areas. Ministry of Public Works and Settlement, Ankara, Turkey.
- TEC-2007 (2007). Turkish Earthquake Code: Regulations on Structures Constructed in Disaster Regions. Ministry of Public Works and Settlement, Ankara, Turkey.
- TS-498 (1997). Design Loads for Buildings. Turkish Standard Institute, Ankara, Turkey.



Evaluation of material properties by NDT methods and FEM analysis of a stone masonry arch bridge

Emre Ercan*, Ninel Alver, Ayhan Nuhoğlu

Department of Civil Engineering, Ege University, 35100 İzmir, Turkey

ABSTRACT

Masonry is the oldest building technique that still finds wide use in today's building industries. The variety and natural availability of the materials that is needed for masonry combined with the easiness of the construction, has resulted in usage of masonry for thousands of years. The lack of research and underdeveloped codes in masonry results in poor applications of masonry technique which causes invaluable loss of lives of people in earthquakes. Today modeling of stone masonry structures is still very difficult because of unknown material properties. This study focuses on estimation of the material properties by destructive testing methods (DT) and non-destructive testing methods (NDT) and analysis of a historic stone masonry arch bridge. After visual investigation, the geometry of the structure is determined and 3D model of the structure was generated and meshed for Finite Element Method (FEM). For evaluation of material properties, NDT methods such as; impact-echo and ultrasonic pulse velocity testing methods were used. Schmidt hammer test was applied for estimation of the hardness of the stones. Fallen stone and mortar samples from the bridge were taken to the laboratory and destructive tests applied on them to determine the properties of masonry components. The test results for the materials obtained from the DT and NDT methods were compared with each other. Using these results mechanical properties of the masonry were estimated using standards and codes. The gathered material properties were assigned to FE model and the model was analyzed.

ARTICLE INFO

Article history: Received 3 June 2015 Accepted 14 August 2015

Keywords: Stone masonry arch Non destructive testing Finite element method Impact-echo

1. Introduction

Modeling of masonry structures is still very difficult because of unknown material properties. In this study a historic stone masonry arch bridge in Urla, Zeytinler village was studied. This study focuses on estimation of the material properties by destructive testing methods (DT) and non-destructive testing methods (NDT) and analysis of this bridge. First, visual investigation established and the geometry of the structure is determined. For testing of material properties for finite element method (FEM) model, NDT methods such as; impact-echo and ultrasonic pulse velocity testing methods were used. Stack imaging of spectral amplitudes based on impact-echo (SIBIE) technique was applied to evaluate the inner structure of the bridge. Schmidt hammer test was applied for

estimation of the hardness of the stones by an L type Schmidt hammer. The uniaxial compressive and indirect tension tests were applied to samples taken from the bridge to determine the strength and modulus of elasticity of the masonry components. The test results for the materials obtained from the DT and NDT methods were compared with each other. Using these tests' results a macro model of the masonry was created by homogenization approach for the FE model. Then, the masonry bridge was analyzed under static loads.

2. Mathematical Model

The structure is 3 spanned stone masonry arch bridge and is located in Urla Zeytinler village. It is on the road

to Çeşme crossing a river. The bridge is not in use since new İzmir-Çeşme (Tepekahve) road opened in 1950's. The bridge has a 42.5 meters length 6.15 meter width and has 7 meters long 3 spans (Fig. 1). The spandered walls and the arches have 1.00 meter and 0.65 meter thickness, respectively. There is rubble stone filling concrete between spandrel walls. The stones used in the masonry are grey and pink andesite. After visual investigation, 3D model of the structure was generated and meshed for Finite Element Method (FEM) (Fig. 2).



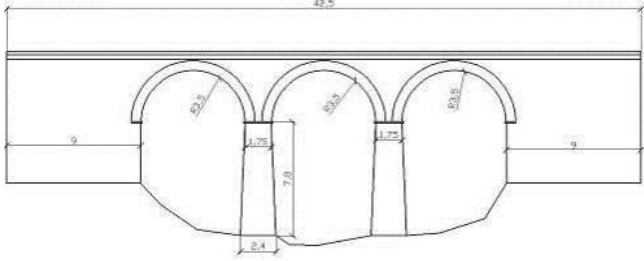


Fig. 1. Stone masonry arch bridge in Zeytinler.

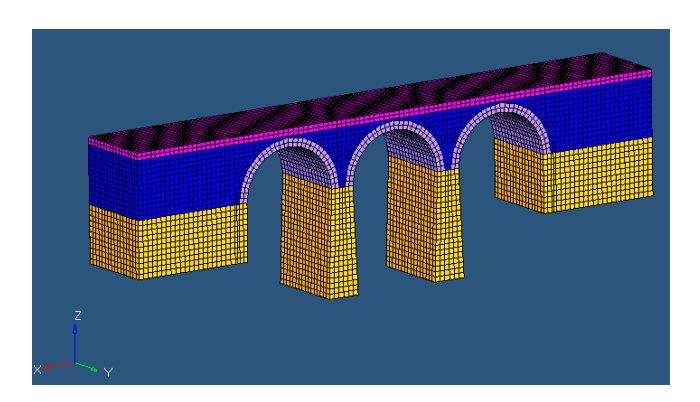


Fig. 2. 3D FE model of the bridge.

2.1. Material tests on stone and mortar

In order to determine the parameters needed for finite element modeling, material nondestructive and destructive tests were applied on constituents of masonry.

For the destructive tests fallen stones from the structure were taken. Stone samples which were strong enough to cut out core samples of diameter 54 mm were selected. Fallen stones were taken to the laboratory and cylinder core samples of diameter 54 mm were drilled out (Fig. 3). The heads of samples were cut with "cut of

machine". Test samples for indirect tension test (Brazilian test) with height of 27-54 mm and samples for uniaxial compression test with height of 108-120 mm were prepared (TS 699, 1987; Ulusay et al., 2001). The heads of the cylinder core samples were grinded in order to have appropriate cylinder samples in emery machine (TS 699, 1987). After samples had been prepared, uni-axial compression and indirect tension tests were applied as shown in Fig. 3. The loading rate was 0.2 mm/minute which satisfies the failure time 1 to 10 minutes (TS 699, 1987). The average results are shown in Table 1.







Fig. 3. Drilling out core samples, uni-axial compression and Brazilian test.

For the nondestructive tests, before taking the samples to the laboratory, L type Proeq Schmidt Hammer was used to find surface hardness values of the stone samples. Schmidt Hammer test was also applied to the stones of the whole structure (Fig. 3). The compressive strength was calculated from the scheme of Ulusay et al. (2001). In the laboratory before indirect and uniaxial compression tests were applied to the stone samples, ultrasonic wave velocity tests had been conducted by CNS Farnel Electronic's Pundit type equipment (Fig. 4). The modulus of elasticity values of stone samples were also determined by Eq. (1) (ASTM 1997, C597).

Tahl	<u> 1</u>	Test	reculte	of stone.
1 417	IC I.	1 525	resurs	or stone.

Sample	Number of Samples	Density ρ (g/cm³)	Rebound Value, <i>R</i>	σ_c from R (MPa)	UAC fc (MPa)	E (GPa)	Tensile Strength f_t (MPa)	Ultra Velocity (m/sec)	E from U.V. (GPa)
Stone	20	2,49	51.89	80	50.35	11.40	5,89	4010	34.88



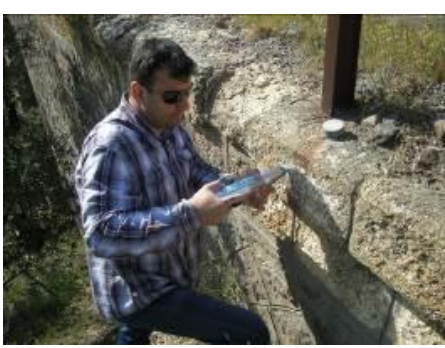




Fig. 4. In situ Schmidt test and ultrasonic wave velocity test on stone samples.

$$E = V^2 \rho (1+m) \frac{1-2m}{1-m},\tag{1}$$

where V, ρ , and m are ultra sonic pulse velocity, density and Poisson's ratio, respectively. The Poisson's ratio is taken as 0.21 for the Andasite stone. The estimated modulus of elasticity values from ultra velocity tests are higher than the values obtained by destructive tests (Table 1).

The mortar samples were weak and too small for drilling so only point load tests could be applied on arbitrary shape samples. By use of the point load index, the uni-axial compressive strengths of mortars were estimated. The average estimated uni-axial strength of mortars was calculated to be 11.95 MPa from point load tests. Tensile strength and modulus of elasticity of mortar was also estimated from literature by the help of

point load test results. Tensile strength and modulus of elasticity σ_t , 1.11 MPa and E, 180 MPa are taken, respectively. The density of the mortar was calculated $\rho = 1.80$ gr/cm³.

2.2. Impact-echo on the stone masonry arch bridge

Impact-echo is one of nondestructive testing methods for concrete based on multiple reflections of an acoustical wave between the test surface of concrete and an interface between materials with different mechanical impedances. An impact load is applied at the surface of the concrete and vibrations caused by this impact are recorded by a receiver. As a result, a waveform is built up in the time domain. In the traditional impact-echo analysis, this waveform is transformed into the frequency domain by applying FFT. Peak frequencies are identified in the frequency spectrum and corresponding depth is calculated by the given formula where C_p is longitudinal wave velocity, f is the measured frequency and d is the corresponding depth (Sansalone and Streett, 1997; Sansalone, 1997).

$$d = C_p/2f. (2)$$

However, in most of the practical applications, due to the complex information existing in the data, it is difficult to interpret the frequency spectrum. Consequently, SIBIE (Stack Imaging of spectral amplitudes Based on Impact-Echo) procedure has been developed to improve impact-echo method. Impact-echo has been applied for evaluation of masonry structures. In this study, a stone masonry bridge was tested by applying impact-echo and SIBIE.

2.2.1. SIBIE Procedure

Based on the inverse scattering theory in elastodynamics (Nakahara and Kitahara, 2002), the SIBIE procedure has been developed at Kumamoto University (Ata et al., 2007; Ohtsu and Watanabe, 2002). This is an imaging technique for detected waveforms in the frequency domain. In the procedure, first, a cross-section of sample is divided into square elements as shown in Fig. 5. Then, resonance frequencies due to reflections at each element are computed. The travel distance from the input location to the output through the element is calculated as (Ohtsu and Watanabe, 2002),

$$R = r_1 + r_2. (3)$$

Resonance frequencies due to reflections at each element are calculated from,

$$f_2' = \frac{c_p}{R_2}$$
 and $f_R = \frac{c_p}{R}$. (4)

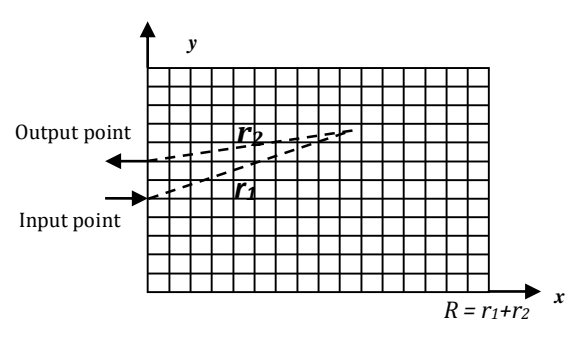


Fig. 5. Spectral imaging model.

Spectral amplitudes corresponding to these two resonance frequencies in the frequency spectrum are summed up at each mesh. Thus, reflection intensity is estimated as a stack image at each element. The minimum size of the square mesh for the SIBIE analysis should be approximately equal to $C_p\Delta t/2$, where C_p is the velocity of P-wave and Δt is the sampling time of a recorded wave.

2.2.2. Results of SIBIE

The stone masonry bridge tested is shown in the Fig. 6. The tests were carried out at several locations of the bridge. A hammer was used in the tests to generate elastic waves. Since the depth of the section to be tested was large, a hammer was used instead of a steel sphere to generate high impact energy. An accelerometer was used to detect surface displacements caused by reflections of the elastic waves. The frequency range of the accelerometer system was from DC to 50 kHz. Fourier spectra of accelerations were analyzed by FFT (Fast Fourier Transform). Sampling time was 4 μ sec and the number of digitized data for each waveform was 2048. The cross-section of the bridge part tested was divided into square elements to perform SIBIE analysis. In this study, the size of square mesh for SIBIE analysis was set to 10 mm.

A result of SIBIE analysis of the impact applied above the center of the arch is depicted in Fig. 6(a). The SIBIE figure corresponds to the cross-section of the element that is tested. Here, red color zones indicate the higher reflection due to the interface between materials with different mechanical impedances. In the figure, impact and detection locations are indicated with arrows. The distance between impact and detection was selected as 5 cm. The depth of the section tested was 120 cm. The back wall reflection of red color zone is very clearly observed at the bottom of the SIBIE figure. The other red color regions are also clearly observed corresponding to the material interfaces. These reflections might be due to air existence between layers which means bonding between layers is not well.

There is another SIBIE result shown in Fig. 6(b). Impact-echo test location is different in this case. As can be seen from the figure the back wall reflection is very clearly observed. Other reflection is observed between two stones at the bottom of the section. The reason of existence of this reflection can be the existence of air between two layers. There are no other high reflections observed in the figure.



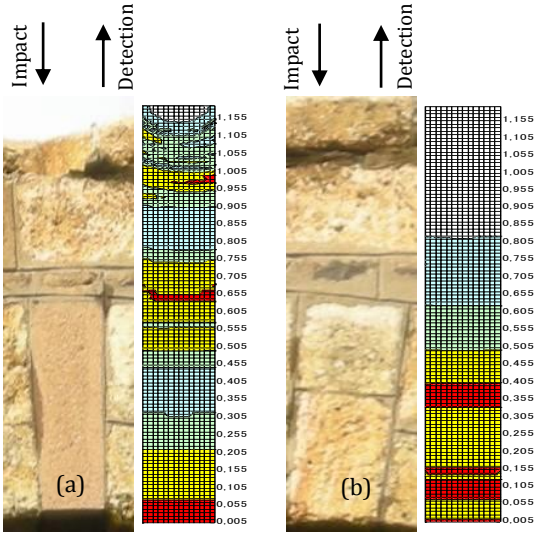


Fig. 6. SIBIE result of the bridge section above the center of the arch (a) and close to the center of the arch (b).

According to the test results it can be said that SIBIE procedure can be applied to stone masonry structures to evaluate the structure non-destructively. The discontinuities in the structure are appeared at the SIBIE results as relevant regions (red zones in this case). Here, by evaluating the results, the dimensions of the stones, thickness of the mortars and thickness of the spandrel walls can be estimated and also it can be said that there are some flaws between layers. These flaws decrease the strength of the material and thus affect the durability of the structure.

3. Finite Element Analyses of the Stone Masonry Arch Bridge

3.1. Determination of material parameters for FE model

The masonry is a composite and this composite material consists of two or more different constituent materials. By the use of homogenization approach, behavior of mortar and stone were assumed together so an overall behavior of the composite media has been taken into account. While determining the elastic parameters of masonry, the homogenization equations which depend on the strength parameters of constituents were used.

The compressive strength of masonry is determined by Eq. (5) (Eurocode 6, 1995).

$$f_k = K f_b^{0.65} f_m^{0.25} \,, \tag{5}$$

where K is a constant, f_b is the compressive strength of stone, f_m is compressive strength of mortar. K is in the range of 0.4 to 0.6 and depends on the morphology of the masonry (Eurocode 6, 1995). K was taken 0.5 in this study.

The modulus of elasticity of masonry was determined by the use of Eq. (6) (Lourenço, 2001).

$$E = \frac{t_m + t_u}{\frac{t_m}{E_m} + \frac{t_u}{E_u}} \rho \,, \tag{6}$$

where t_m , t_u , E_m , E_u are the thickness of mortar and height of the unit the coefficient ρ varies with the bond between mortar and unit and was taken 0.5 for this study (Lourenço, 2001).

The shear modulus can be taken as 40% of the modulus of elasticity (Eurocode 6, 1995). The tensile strength of masonry can be taken as 10% of compressive strength (Koçak, 1999).

The density of BM and fill were calculated as $2.1 \, \text{kg/cm}^3$ and $1.75 \, \text{kg/cm}^3$, respectively. The Poisson's ratio was taken as $0.17 \, \text{for masonry}$ (Koçak, 1999). Elastic material parameters of SM and Fill for finite element model are shown in Table 2.

Table 2. Material parameters of masonry for FE model.

	Stone Masonry	Fill
Compressive Strength (MPa)	11.88	9.49
Tensile Strength (MPa)	1.18	0.76
Modulus of Elasticity (MPa)	1164.3	600
Shear Modulus	465.7	240
Density (kg/m³)	2100	1950
Poisson Ratio	0.17	0.05

4. 3D FEM Analysis of the Bridge

The data gathered from destructive and nondestructive tests were used for FE analysis of the bridge. Linear elastic self weight analysis of the structure was conducted in order to check the safety of the structure under its own weight. The stress results of the FEM analysis were very small compared to its allowable stress proving that the structure is safe.

5. Conclusions

In this paper, numerical analysis of a stone masonry arch bridge is presented and performed by means of a FEM. The material properties of the masonry were estimated by NDT and DT methods. By using SIBIE the inner parts of structure were identified and it can be said that SIBIE procedure can be applied to stone masonry structures to evaluate the structure non-destructively. By evaluating the results, the dimensions of the stones, thickness of the mortars and thickness of the spandrel walls can be estimated. According to the FE analysis structure is safe under its self weight. The results of a FEM analysis can be useful, in case of restoration of masonry arches.

REFERENCES

ASTM-C597-97 (1997). Standard Test Method for Pulse Velocity through Concrete. American Society of Testing and Materials, Pennsylvania.

ASTM-D2845-97 (1969). Standard Method for Laboratory Determination of Pulse Velocities and Ultrasonic Elastic Constants of Rock.

Ata N, Mihara S, Ohtsu M (2007). Imaging of ungrouted tendon ducts in prestressed concrete by improved SIBIE. *NDT&E International*, 40(3), 258-264.

Eurocode 6 (1996). Design of Masonry Structures. European Committee for Standardization, Brussels.

Koçak A (1999). Linear and Nonlinear Analysis of Historical Masonry Structures Under Static and Dynamic Loads Case Study: Küçük Ayasofya Mosque. *Ph.D. thesis*, Yıldız Technical University, İstanbul.

Lourenço PB (1996). Computational Strategies for Masonry Structures. *Ph.D. thesis*, Delft University Press, Netherlands.

Lourenço PB (2001). Assessment of the stability conditions of Cistercian Cloister. 2nd International Congress on Studies in Ancient Structures, İstanbul.

Nakahara K, Kitahara M (2002). Inversion of defects by linearized inverse scattering methods with measured waveforms. Proceedings International Symposium on Inverse Problems in Engineering Mechanics (ISIP2000), Springer, Berlin, 9-18.

Ohtsu M, Watanabe T (2002). Stack imaging of spectral amplitudes based on impact-echo for flaw detection. *NDT&E International*, 35(3), 189-196.

Sansalone MJ, Streett WB (1997). Impact-echo, Ithaca. NY Bullbrier Press, New York.

Sansalone M, Impact-echo (1997). The complete story. *ACI Structural Journal*, 94(6), 777-786.

SAP2000 (2005). Integrated Finite Element Analysis and Design of Structures, Computers and Structures Inc., Berkeley, California, IISA.

TS 699 (1987). Methods of Testing Naturel Building Stones. Institute of Turkish Standards, Ankara.

Ulusay R, Gökçeoğlu C, Binal A (2001). Rock Mechanics Laboratory Experiments. Turkish Chambers of Geology Engineers, Ankara.



Nonlinear finite element analysis of strength and durability of reinforced concrete and composite structures

A. Ghani Razaqpur ^{a,*}, O. Burkan Isgor ^b, Afshin Esfandiari ^c

- ^a Department of Civil Engineering, McMaster University, Hamilton, Ontario L8S 4L8, Canada
- ^b Department of Civil and Environmental Engineering, Carleton University, Ottawa, Ontario K1S 5B6, Canada
- ^c Department of Civil Engineering, University of British Columbia, Vancouver, British Columbia V6T 1Z4, Canada

ABSTRACT

The finite element method has emerged as the most powerful and versatile numerical method for solving a wide range of physical problems in science and engineering. Today a large number of commercial programs exist that can be used to solve diverse problems in structural and fluid mechanics, heat transfer and many other phenomena. However, certain critical problems related to durability of concrete structures, especially corrosion of reinforcement, cannot be readily solved using the available software. This paper presents two finite element formulations, developed by the writers, one dealing with the nonlinear analysis of composite concrete-steel bridges, and the other with the durability of concrete structures, with emphasis on the corrosion of reinforcement. The validity and accuracy of the proposed models are demonstrated by comparing their results with appropriate experimental data.

ARTICLE INFO

Article history:
Received 31 July 2015
Accepted 7 September 2015

Keywords:
Finite element method
Nonlinear analysis
Composite structures
Durability
Corrosion

1. Introduction

The finite element method (FEM) was developed nearly half a century ago (Turner et al., 1956) to solve two dimensional stress analysis problems; since then it has evolved as the most powerful numerical method for the solution of a wide range of problems in many areas of science and engineering (Zienkiewicz and Taylor, 1989). Today it is routinely used by many practicing engineers to solve diverse problems which cannot be otherwise solved due to their complex boundary conditions or anisotropic and nonlinear properties. While existing commercial software can be used to solve a wide spectrum of problems, certain practical problems in civil engineering, such as those dealing with durability of concrete structures, cannot be solved readily using current commercial software. Among these are the prediction of alkali-aggregate reaction, sulphate attack, and corrosion of reinforcement. In this paper, a summary of the basic FEM formulation for two problems that the writers have worked on will be presented. The two problems are among topics of current interest in the structural engineering community; namely, durability, serviceability and safety of concrete bridges and other exposed structures.

2. Nonlinear Analysis of Composite Bridges

Due to the noticeable increase in the permissible live load of bridges over the last 50 years, there is need for the accurate assessment of their serviceability and strength. Composite bridges, comprising steel girders attached to a concrete slab, Fig. 1(a), are common in many countries, and their serviceability and strength depend on the interaction between the concrete slab and the steel girders. Various types of connectors can be used to attach the slab to the girders, including welded steel sections and headed studs, Fig. 1(b), but today the latter type of connector is most commonly used. These connectors may achieve different levels of composite action, varying from practically no interaction to full composite action. The level of interaction may also depend on level of applied load on the bridge. Although the FEM analysis of such bridges can be performed under the assumption of full composite action, the analysis of partial interaction, caused by relative movement at the slab-girder interfaces requires more effort. Continuum contact elements, available in some FEM commercial programs, can be used to model the interaction, but the model parameters need to be carefully selected by transforming the

^{*} Corresponding author. Tel.: +1-905-525-9140; E-mail address: razaqpu@mcmaster.ca (A. G. Razaqpur) ISSN: 2149-8024 / DOI: http://dx.doi.org/10.20528/cjsmec.2015.09.030

properties of the connector to equivalent properties that can characterize the interface. Alternatively, a discrete element can be developed whose properties could be directly obtained from the geometry and material properties of the actual connector. Razaqpur and Nofal (1989) originally developed such a discrete element, which was subsequently improved by Esfandiari (2001) and its accuracy was verified by comparing its results with several sets of experimental data. The improved model and its verification are described below.





Fig. 1. (a) Typical steel-concrete composite bridge, (b) Steel girder with stud shear connectors.

2.1. Shear connector finite element

Shear connectors, as shown in Fig. 2(a), can be modeled as truss element with five degrees of freedom, where the usual sixth degree of freedom is constrained by assuming the connector to be axially rigid. This constraint is optional, but if not enforced the connector would allow for separation normal to the slab-girder interface. The derivation of the stiffness matrix for this element requires the shear force-slip relationship of the connector. One such relationship was proposed by Yam and Chapman (1968) based on their test data, viz.

$$F = a(1 - e^{-b\lambda}), \tag{1}$$

where F is the shear force acting on either end of the connector in one of the two orthogonal directions (kN) and λ (mm) is the corresponding relative displacement or slip in the direction of F, Fig. 2(b); a and b are experi-

mental constants, which depend on the connector geometry and strength; and e is base of the natural logarithm. For stud connectors, Yam and Chapman suggested a and b to be 30 kN and 4.72 mm. Using these values, Eq. (1) is plotted in Fig. 3. Note that assuming different values for a and b allows one to model connectors with different strength and stiffness.

Using Eq. (1) and assuming that shear connectors only allow slip at the interface, the stiffness matrix can be written as:

$$[K] = \begin{bmatrix} k_1 & 0 & -k_1 & 0 & 0\\ 0 & 0 & 0 & 0 & 0\\ 0 & 0 & k_2 & 0 & -k_2\\ -k_1 & 0 & 0 & k_1 & 0\\ 0 & 0 & -k_2 & 0 & k_2 \end{bmatrix}, \tag{2}$$

where k_1 and k_2 are the shear stiffness coefficients in the two orthogonal directions in the plane of the connector cross-section, and are given by

$$k_j = \frac{\partial k_j}{\partial \lambda_j} = abe^{-b\lambda},\tag{3}$$

where F_j is the component of shear force acting on the connector cross-section in direct j(j=1,2) and λ_j is its associated slip (Fig. 2(b)). As stated earlier, the bar is assumed to be axially rigid, which is enforced by imposing equal axial displacement at the two ends of the element as shown in Fig. 2(a).

In using the above stiffness matrix, there is another problem which must be considered. As illustrated in Fig. 2(b) the shear forces acting on a shear connector equilibrate each other ($\sum F_x = 0$, $\sum F_y = 0$), but they create unbalanced moments F_1L and F_2L , where L is the connector length, and these moments violate the equilibrium requirement. To overcome this problem, in this study the unbalanced moments are reversed and applied as nodal forces at the end of each iteration during the solution process (Esfandiari, 2001). These moments are

$$(dM_1)_i = (K)_{i-1}(d\lambda_1)_i L,$$
 (4a)

$$(dM_2)_i = (K)_{i-1} (d\lambda_2)_i L,$$
 (4b)

where $(dM_1)_i$ and $(dM_2)_i$ are unbalanced moments for ith iteration, $(K_1)_{i-1}$ and $(K_2)_{i-1}$ are stiffness elements of shear connector corresponding to the results of previous iteration and $(d\lambda_1)_i$, $(d\lambda_2)_i$ are incremental slip values. Note that

$$\lambda_1 = u_4 - u_1 \,, \tag{5a}$$

$$\lambda_2 = u_3 - u_5 \,, \tag{5b}$$

$$d\lambda_1 = du_1 - du_4 \,, \tag{6a}$$

$$d\lambda_2 = du_3 - du_5 \,, \tag{6b}$$

where u_j and du_j are, respectively, the total and incremental displacement of the *j*th degree of freedom.

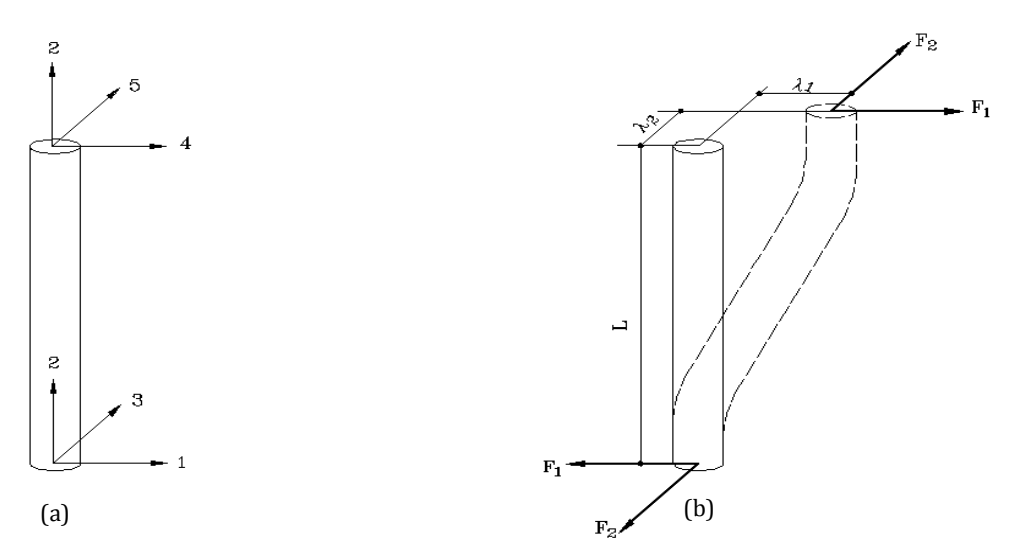


Fig. 2. Shear connector element; (a) Nodal degrees of freedom, (b) Deformed shape.

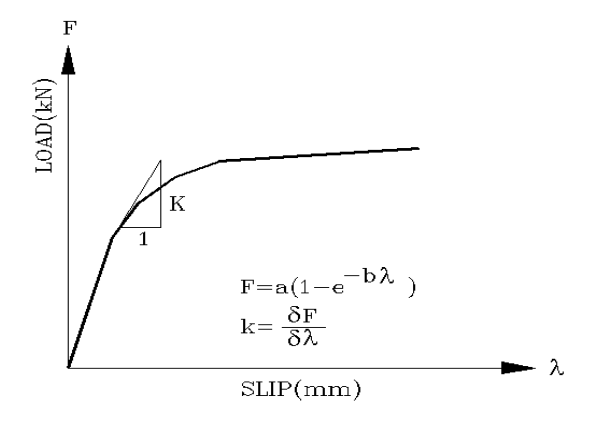


Fig. 3. Typical load slip curve for shear connector element.

2.2. Experimental verification of the model

To verify the above method, the experimental results of Yam and Chapman's continuous beam (1972), tested at Imperial College, and Razaqpur and Nofal's bridge model (1988) will be compared with the finite element results. This element is implemented in the nonlinear finite element program NONLACS (Razaqpur and Nofal, 1990), which can be used to analyze any three dimensional reinforced/prestressed concrete, steel or composite structure that can be idealized as an assemblage of thin shell elements. The program uses theory of plasticity in conjunction with Von Mises' yield criterion for the steel elements and the so-called equivalent strain concept and the Kupfer and Gerstle (1973) biaxial failure criterion for concrete. Steel reinforcement is modeled as either discrete truss bars or as smeared steel layer. The program uses the smeared crack approach and includes tension stiffening.

2.2.1. Imperial College continuous beam

Yam and Chapman reported the experimental data for a number of continuous beams. One of those beams, analyzed in this study, had the loading and geometry illustrated in Fig. 4 and the material properties shown in Table 1. The beam has two spans of 3.355 m each and consists of a 152 mm deep I-section attached to a 60 mm thick and 920 mm wide concrete slab by means of stud shear connectors. The properties in Table 1 were taken from Yam and Chapman's report, but some properties that were not given by them had to be assumed. The finite element mesh was similar to the one used for the bridge model of Razaqpur and Nofal that will be described in the next section.

Figs. 5, 6, and 7 compare the experimental and computed deflected shape, slip along concrete-steel interface, and strain along the bottom flange of the girder from the left support to the centerline at load P=108.5 kN. We see good agreement between the two sets of results, which corroborate the accuracy of the proposed model.

2.2.2. Razaqpur and Nofal bridge model

This 1/3 scale bridge model was built and tested by Razaqpur and Nofal (1988). It was the model of a two-lane bridge, 6.24 m wide and 18.00 m long. It has three W840 x 170 compact steel girders spaced at 1.86 m. The concrete slab has a total thickness of 182mm. Figs. 8 and 9 show the geometry and loading of the bridge model and Table 2 shows its material properties. The material strength values were obtained by Razaqpur and Nofal from ancillary tests performed on concrete cylinders and steel coupons. The bridge is simply supported with three girders (3 W250x39) on 6 m span. The supports are roller at one end and hinged at the other and the slab is 70 mm thick and 2060 mm wide.

The actuator loads were applied through $83\ mm\ x\ 200\ mm$ steel plates, placed above the central girder flange on the concrete slab.

2.2.3. Finite element idealization

The finite element idealization of the bridge is shown in Fig. 10. The finite element mesh consists of 20 elements along the span and 24 in the cross section. The top and bottom steel reinforcement in the slab was modeled

as smeared layers, and the slab mid-plane nodes were connected to the top flange nodes directly below them by the shear connector elements. As shown in Fig. 10, the steel girders webs and flanges were idealized by elements with a

single layer, while the concrete slab was divided into 10 layers through its thickness. The applied load was divided into 20 increments and the bridge was analyzed over the entire loading range up to failure.

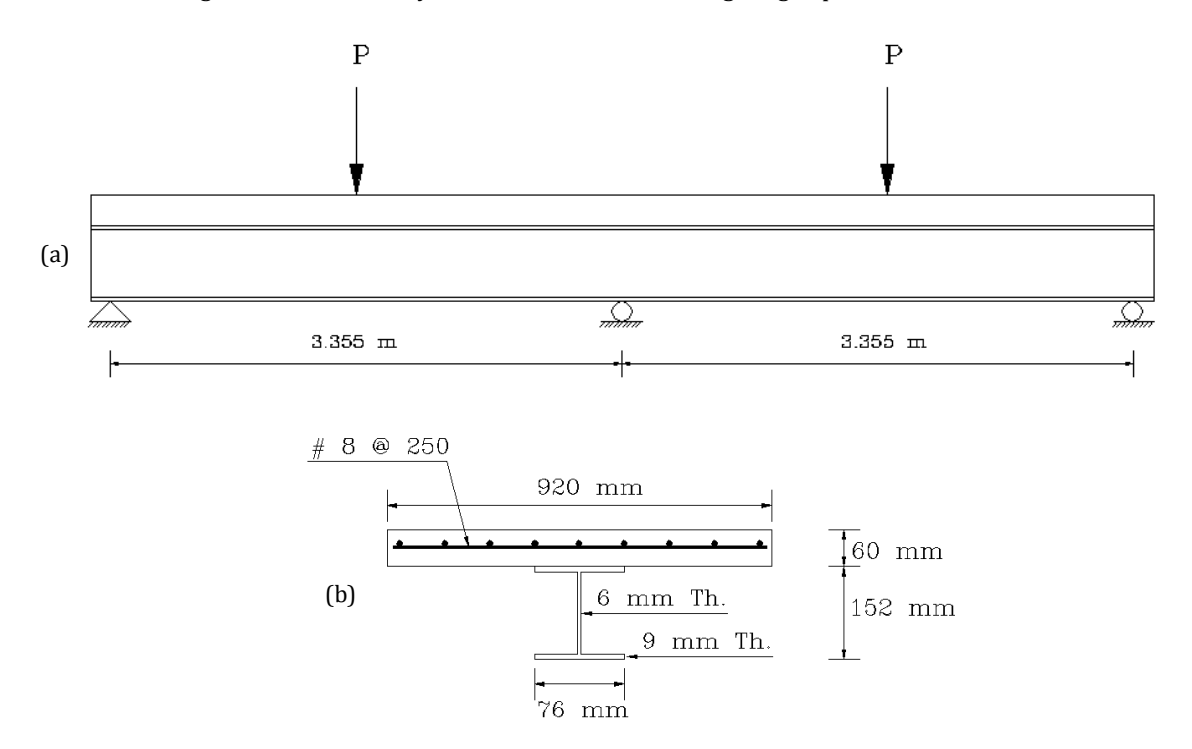


Fig. 4. Imperial College continuous beam details; (a) Elevation, (b) Cross section.

Table 1. Material properties of Imperial College continuous beam.

Material Constants	Concrete	Reinforcing Steel	Steel Girder	
f_y (MPa)	-	270	270	Given
E_s (MPa)	-	200000	200000	Given
E_{s}^{*} (MPa)	-	5000	5000	Given
f'_c (MPa)	47.6	-	-	Given
\mathcal{E}_{max}	0.035	-	-	Assumed
€ cu	0.002	-	-	Assumed
Connector Details		$\frac{3'}{8} \times 2'$ Headed studs,	two rows at 5.72	inch

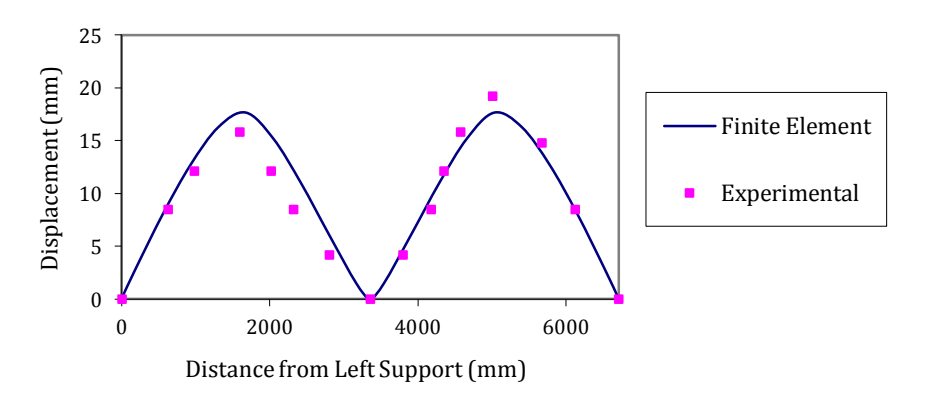


Fig. 5. Deflected shape of Imperial College continuous beam at *P*=108.5 kN.

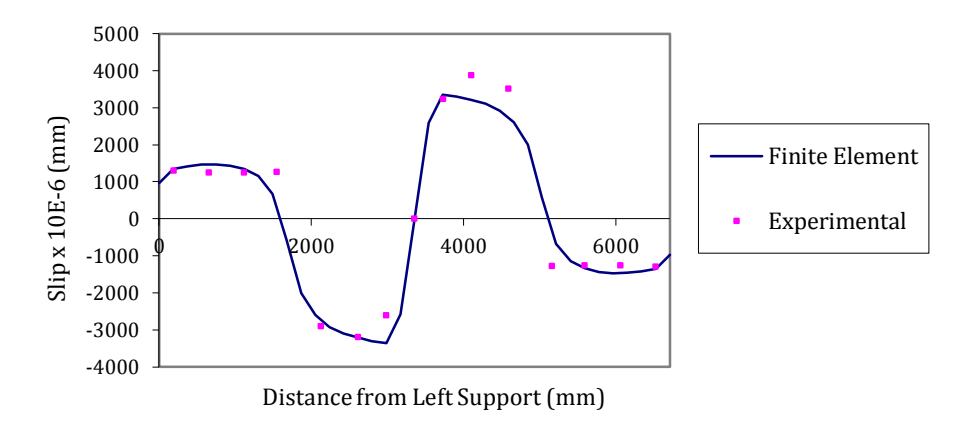


Fig. 6. Concrete-steel interface slip in continuous beam at *P*=108.5 kN.

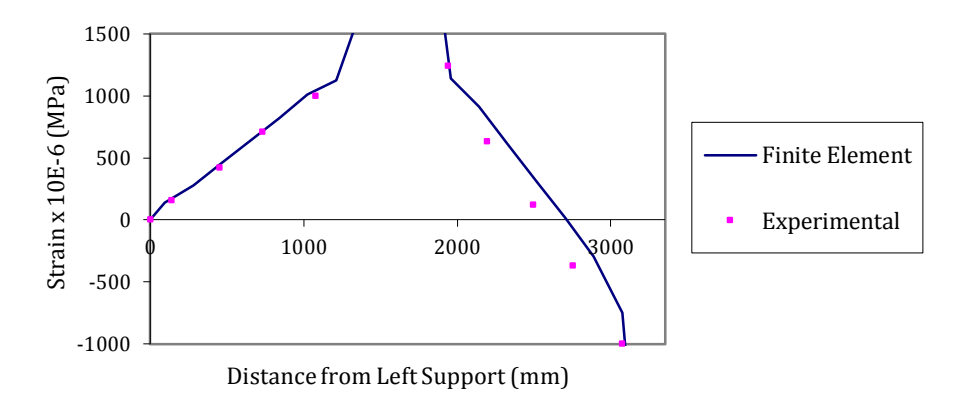


Fig. 7. Strain along the bottom flange of the continuous beam at *P*=108.5 kN.

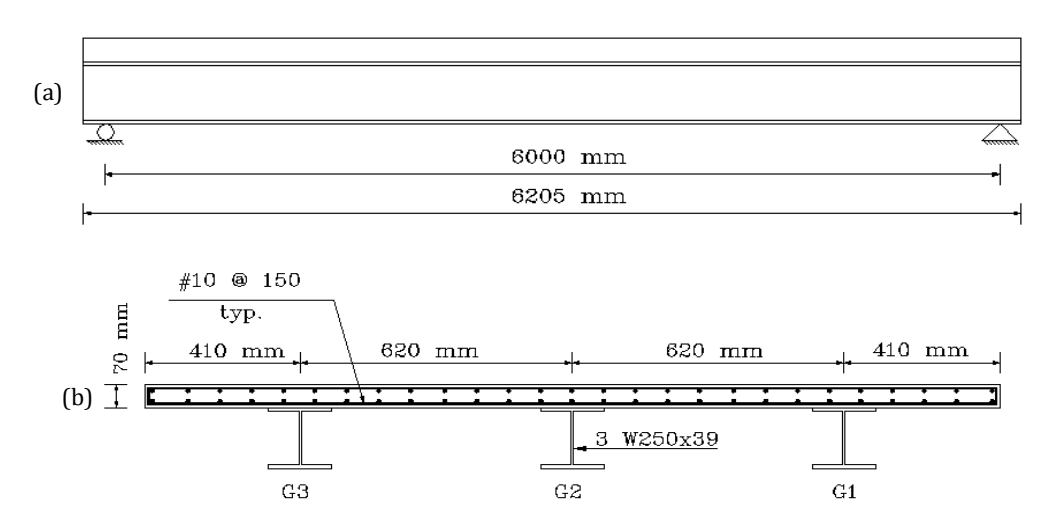


Fig. 8. Geometry of bridge model; a) Elevation, b) Cross section.

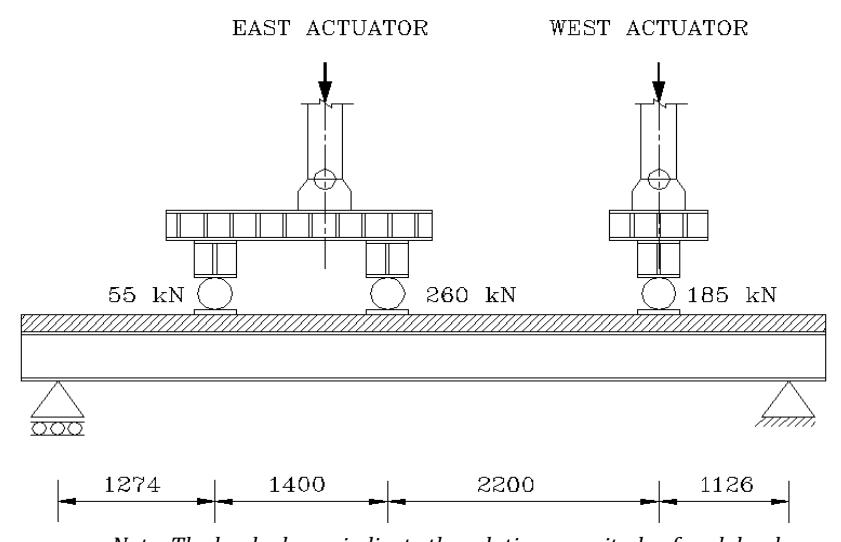
2.2.4. Comparison of FEM results with experimental data

For brevity, selective FEM results are compared with the corresponding experimental data. Fig. 11(a) shows the full load- deflection curve of Girder 3 while Fig. 11(b) shows the deflected shape of the same girder under increasing load. The ultimate load predicted by finite element was calculated to be 800 kN, which is 4% higher than the corresponding experimental load of 766 kN.

Actually, the test had to be stopped because the actuator stroke was exhausted, albeit at the end of the test,

large deformations and a visible plastic hinge had formed in the central girder. Thus, it is possible that the bridge could still carry some extra load before total collapse.

The variation of the longitudinal strain along the centerline of the top and bottom flanges of Girder G3 is plotted for different load levels in Fig. 12(a) and (b), respectively. Considering the rather large strain values in the bottom flange, it is obvious that the bridge has practically reached its ultimate capacity and is on the verge of failure. Similarly good comparison was observed for the concrete and steel reinforcement strains.



 $Note: The \ loads \ shown \ indicate \ the \ relative \ magnitude \ of \ each \ load$

Fig. 9. Loading of bridge model.

Table 2. Material properties of bridge model.

Material Constants	Concrete	Reinforcing Steel	Steel Girder	
f _y (MPa)	-	400	300	Given
E_s (MPa)	-	200000	200000	Given
E_{s}^{*} (MPa)	-	0	0	Given
f_c (MPa)	40	-	-	Given
ε_{max} (at peak stress)	0.002	-	-	Assumed
\mathcal{E}_{cu} (at peak failure)	0.0035	-	-	Assumed
Connector Details	15 mi	m × 60 mm Headed s	tuds, two rows at	150 mm

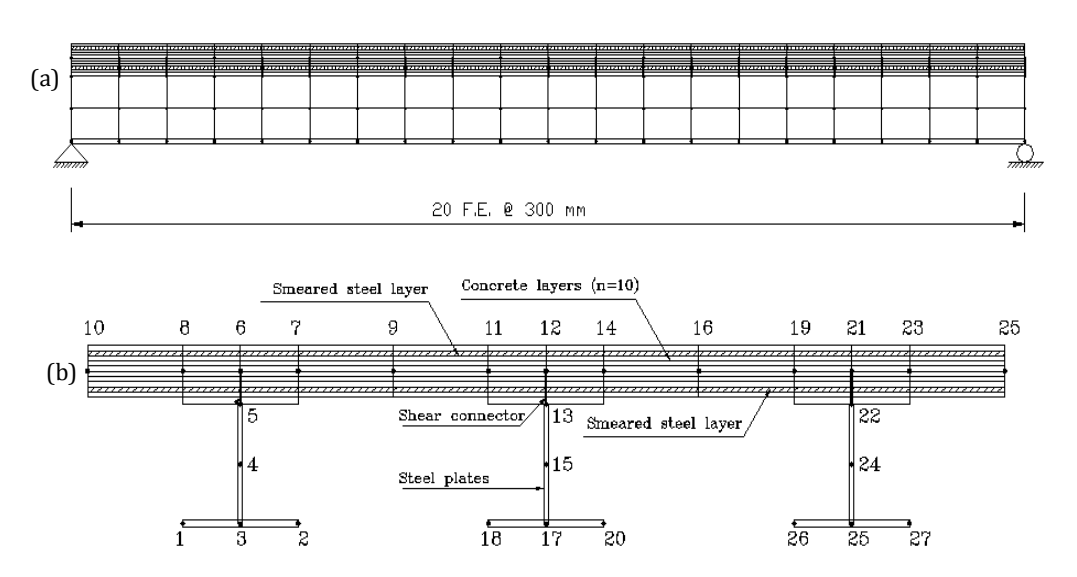


Fig. 10. Finite element idealization of bridge model; a) Elevation, b) Cross section.

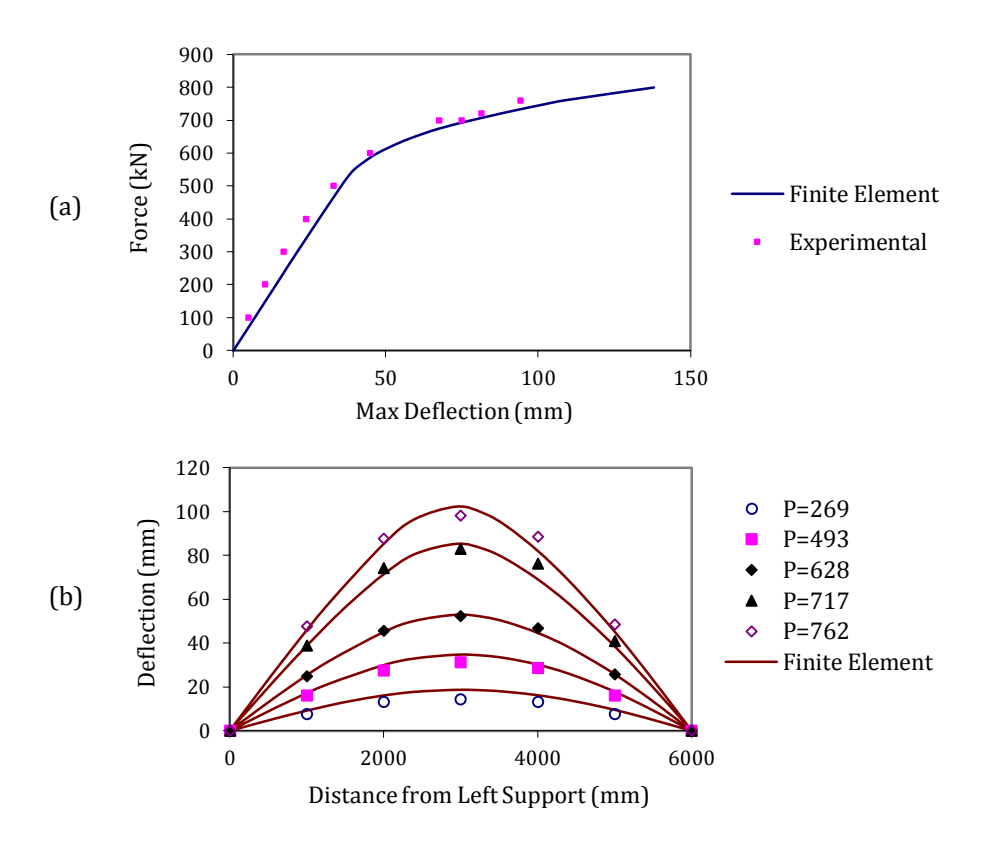


Fig. 11. Comparison of FEM and experimental results for girder G3; (a) Load-maximum deflection curve, (b) Deflected shape.

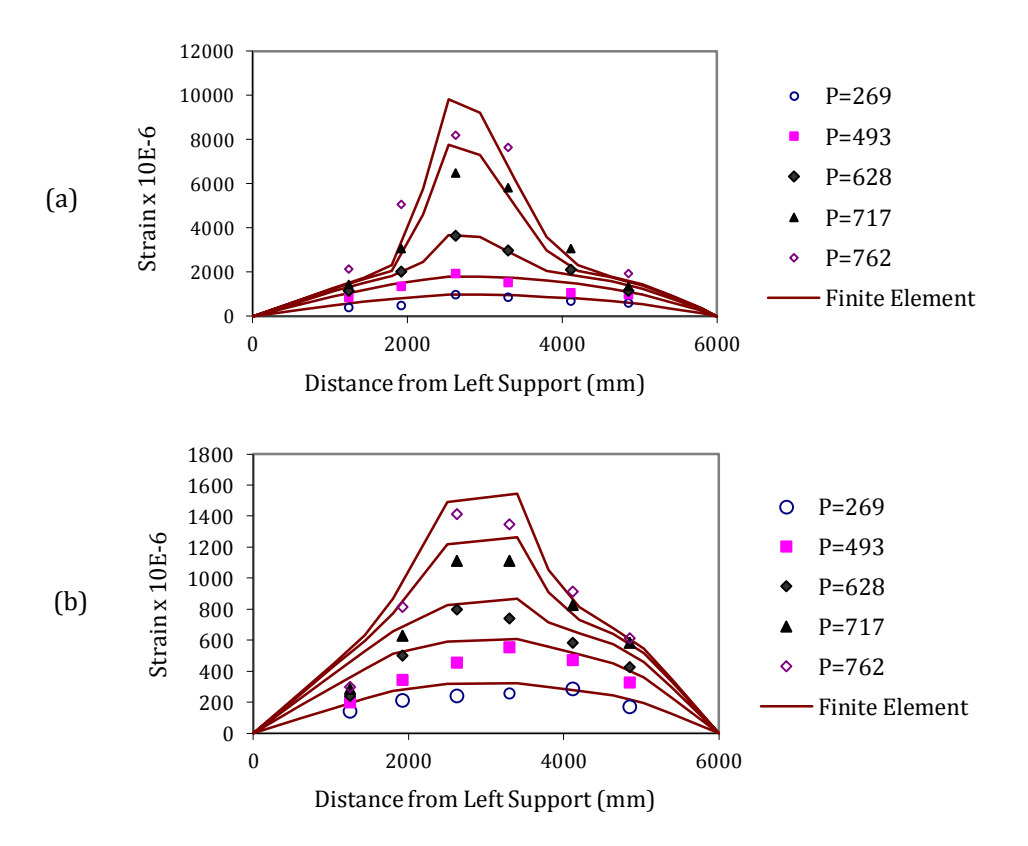


Fig. 12. Comparison of girder G3 top and bottom flanges longitudinal strain values obtained by FEM analysis with the corresponding experimental data; (a) Top flance, (b) Bottom flance.

Again, it is clear that program NONLAC and the proposed shear connector model predicts the response of these bridges accurately.

Next, the finite element formulation of chloride diffusion, carbonation and reinforcement corrosion in concrete structures is presented.

3. FEM Modelling of Concrete Durability

To prevent steel reinforcement corrosion and the ensuing deterioration of concrete, it is useful to have tools that would enable designers to predict the performance of structures under prescribed environmental/chemical conditions. Here a model is proposed and is implemented in a finite element program. The results of the model are validated by comparing them with available experimental data. The model includes consideration of the various phenomena which influence both the initiation and propagation stages of the corrosion process. This includes temperature, moisture, chloride ions, and oxygen transport within concrete. The model accounts for the effects of changes in exposure conditions on the rate of corrosion and the effects of the corrosion reactions on the transport properties of concrete.

3.1. Steel reinforcement corrosion process

Within the initially high alkaline environment of concrete, reinforcing steel is covered with an insoluble film of iron oxides (passive layer) which normally protects the steel from further corrosion. The loss of the passive layer, termed depassivation, leads to further corrosion. The presence of chloride ions, the carbonation of concrete, the physical and the chemical properties of concrete, the surface characteristics and the chemical composition of steel, and sustained mechanical stresses are key factors influencing the depassivation and rate of corrosion of steel in concrete (Neville, 1996; Broomfield, 1997; Uhlig and Revie, 1985).

It has become common practice to divide the corrosion process in concrete into two successive stages. The first stage, called the initiation stage, is defined as the period during which corrosive agents, such as chloride ions or carbon dioxide, enter concrete and move towards the reinforcement from the surface of concrete, while the steel remains passive. The loss of passivity marks the onset of the second, or propagation, stage during which active corrosion of steel occurs (Tutti, 1982). Existing models define the beginning of the propagation stage in terms of the free chloride concentration at the surface of the steel. Once this concentration exceeds a prescribed threshold, corrosion is assumed to commence. Subsequent entry of more chlorides is assumed to be inconsequential insofar as corrosion rate and amount is concerned. The problem with this approach is neglecting the symbiotic relationship between the initiation and propagation stages (Maruya et al., 2003).

In the present study, which is based on the writer's previous work (Isgor and Razaqpur, 2004, 2005, 2006a

and 2006b), the initiation and propagation stages are unified and are treated with the same level of detail. In existing models, the initiation stage parameters, such as concrete temperature, moisture content, chloride ions and oxygen concentrations normally vary within this stage, but not in the propagation stage. On the contrary, in the proposed model these parameters are assumed to vary in both stages, which allows for the consideration of the effects of corrosion reactions on the properties of concrete and the chemical composition of the pore solution around the reinforcement (e.g. changes in electrical resistivity, pH, and oxygen concentration).

3.2. Proposed model

As discussed previously, the proposed model consists of initiation and propagation stages as described below.

3.2.1. Initiation stage

The governing equations of the phenomena considered in the initiation stage of the model are shown in Table 3. Fig. 13 illustrates the solution strategy that is used, and it allows the distribution of the following environmental / chemical quantities in a member: temperature, moisture, pH (OH- concentration), and oxygen concentration.

3.2.2. Finite element solution of governing equations

As indicated in Table 3, the distribution of each parameter in concrete is governed by a quasi-harmonic equation of the form:

$$k_x \frac{\partial^2 \phi}{\partial x^2} + k_y \frac{\partial^2 \phi}{\partial y^2} + Q = m \frac{\partial \phi}{\partial t},\tag{7}$$

where k_x and k_y are the appropriate conductivities, Q is the sink/source term, and m is a coefficient representing the pertinent material properties. The quantity φ denotes a potential which may be due to chemical concentration, thermal, electrical or hydraulic fields. The term on the right-hand side of Eq. (7) represents the change in potential with time. Following Logan (1992), the functional corresponding to Eq. (7) may be written as π_b :

$$\pi_{h} = \frac{1}{2} \iiint_{V} \left[k_{x} \left(\frac{\partial \varphi}{\partial x} \right)^{2} + k_{y} \left(\frac{\partial \varphi}{\partial y} \right)^{2} - 2 \left(\mathcal{Q} - c \rho \frac{\partial \varphi}{\partial t} \right) \varphi \right] dV - \iiint_{S_{1}} q^{*} \varphi dS + \frac{1}{2} \iint_{S_{2}} h_{c} (\varphi - \varphi_{\infty})^{2} dS , \quad (8)$$

where h_c is the coefficient of convection, ϕ_{∞} is the value of the field variable away from the boundary, V is the volume of the domain of interest (finite element), S is its surface, S_1 and S_2 are portions of the boundary over which flux q^* , and convective transfer are specified, respectively. Using customary finite element notation, Eq. (2) can be written in matrix form as:

$$\pi_{h} = \frac{1}{2} \{\phi\}^{T} \iiint_{V} \left[[B]^{T} [D] [B] \right] dV \{\phi\} - \{\phi\}^{T} \iiint_{V} [N]^{T} Q dV + \iiint_{V} \rho c[N]^{T} \{\phi\}^{T} [N] \frac{\partial \{\phi\}}{\partial t} dV - \{\phi\}^{T} \iint_{S_{1}} [N]^{T} q * dS + \frac{1}{2} \iint_{S_{2}} h_{c} \left[(\{\phi\}^{T} [N]^{T} [N] \{\phi\} - (\{\phi\}^{T} [N]^{T} + [N] \{\phi\}) \phi_{\infty} + \phi_{\infty}^{2} \right) \right] dS,$$

$$(9)$$

where $\{\phi\}$ is the vector representing the nodal values of the field variable, [N] is the shape function matrix, [D] is the material property matrix and [B] is a matrix whose elements are derivatives of the shape functions.

Table 3. The governing equations of the initiation stage of the model.

Process	Governing Equation	Definitions	Explanations
Heat Transfer $\phi = T$	$k\nabla^2 T + Q_T = \rho c \frac{\partial T}{\partial t} + \frac{hP}{A} (T - T_{\infty})$	T : temperature k : Thermal conductivity Q_T : sink / source term ρ : density c : specific heat of concrete t : time h : coeff. of conductive heat transfer $A(P)$: area(perimeter)	Includes convective and radiative boundary conditions Assumed to be unaffected by the moisture tranfer
Moisture Transfer $\phi = h$	$D_h \nabla^2 h + Q_h = \frac{\partial w_e}{\partial h} \frac{\partial h}{\partial t}$	h : relative humidity D_h : moisture diffusion coefficient Q_h : sink / source term w_e : evaporable water content t : time	 Dh is a function of temperature Production of water in the carbonation reaction provides the source term for the moisture transfer analysis Equilibrium between vapour and liquid phases is monitored by using equilibrium isotherms
Chloride Transport $\phi = C_f$	$D_{Cl}\nabla^2 C_f + Q_{Cl} = \frac{\partial C_f}{\partial t}$	C_f : free [Cl-] D_{cl} : Chloride diffusion coefficient Q_{cl} : sink / source term representing chloride binding or release t : time	A number of Chloride binding isotherms are implemented in the model through the sink term Chloride release under low pH is implemented by using the source term
CO_2 Transport $\phi = C_c$	$D_c \nabla^2 C_c + Q_c = \frac{\partial C_c}{\partial t}$	C_c : CO ₂ concentration D_c : CO ₂ diffusion coefficient Q_c : sink / source term representing carbonation reactions t: time	1) The source term represents the carbonation reactions 2) The concentration changes of chemical compounds and the pH are monitored at each time step 3) Changes in pore structure due to carbonation is considered
O_2 Transport $\phi = C_o$	$D_o \nabla^2 C_o + Q_o = \frac{\partial C_o}{\partial t}$	$C_o: O_2$ concentration $D_o: O_2$ diffusion coefficient $Q_o: sink / source term$ t: time	Oxygen diffusion is considered to be a function of moisture content, temperature and porosity of concrete

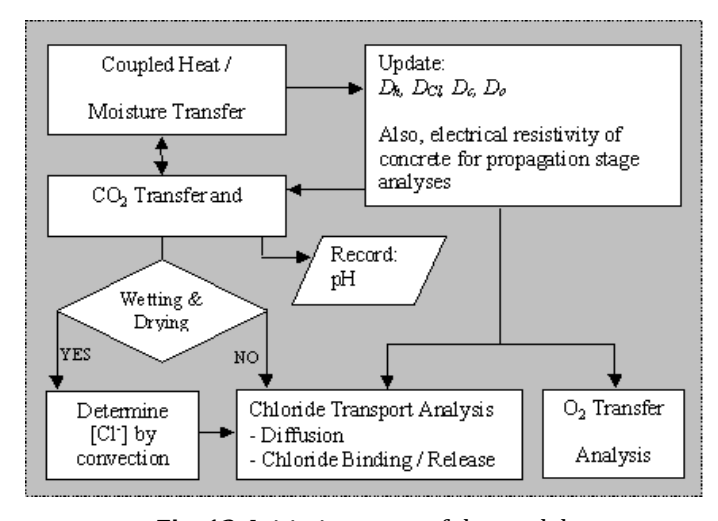


Fig. 13. Initiation stage of the model.

Using the principle of stationary potential, the following equations of equilibrium are obtained:

$$[k]\{\phi\} + [m]\{\dot{\phi}\} = \{f\},$$
 (10)

where the superscript dot denotes differentiation with respect to time. Eq. (10) can be written in expanded form as:

$$\left[\iiint_{V} \left[[B]^{T}[D][B] \right] dV + \iint_{S_{2}} h[N]^{T}[N] dS \right] \{\phi\} + \\
\left[\iiint_{V} c\rho[N]^{T}[N] dV \right] \{\dot{\phi}\} = \iiint_{V} [N]^{T} Q dV + \\
\iint_{S_{1}} [N]^{T} q^{*} dS + \iint_{S_{2}} [N]^{T} h_{c} \varphi_{\infty} dS . \tag{11}$$

Using well known finite element techniques, the global balance equations are set-up by assembling the element balance equations, and they are solved using numerical time integration schemes; the details of the solution procedure and more information on the initiation stage can be found in Martín-Pérez (1999) and Dhatt and Touzot (1984).

3.2.3. Propagation stage

The corrosion rate of steel is a function of the current density, which can be determined at any point on the steel if the electrochemical potential (abbreviated henceforth as "potential") distribution around that point is known. Knowing the potential distribution, the current density, i [A/cm²], at any point on the steel surface can be calculated using:

$$i = -\frac{1}{r} \frac{\partial \phi}{\partial n}. \tag{12}$$

 ϕ [volts] is the potential, r [Ω -cm (ohm-cm)] is the resistivity of the pore solution and n is the direction normal to the bar surface.

The rate of rust production at the anodic regions, J_{rust} [kg/m²·s], is related to the current density by Faraday's law. Consequently, the rate of ferrous oxide, Fe(OH)2, production, J_{Fa} , at the anodic regions can be written as:

$$J_{Fa} = \frac{i_a}{z_F} = 4.656 \times 10^{-7} i_a \,, \tag{13}$$

where i_a is the anodic current density, F is the Faraday's constant (9.65x10⁴ C/mol), and z is the number of electrons exchanged in the reaction (z=2 for steel corrosion). Fe(OH)₂, can be further oxidized, and this will result in the production of Fe(OH)₃. Since one mole of Fe(OH)₂, which is 89.845 g, produces one mole of Fe(OH)₃ (106.845 g), the rate of rust production, J_{rust} , at the anodic regions can be calculated as:

$$J_{rust} = \frac{106.845}{89.845} J_{Fa} = 5.556 \times 10^{-7} i_a.$$
 (14)

The main difficulty in this process is the calculation of current densities on the steel surface. According to Eq. (12), the calculation of current densities requires knowledge of the electrochemical potential distribution in the vicinity of the reinforcement.

Based on the law of electrical charge conservation and isotropic conductivity, the potential distribution can be represented by the Laplace's equation (Munn, 1982):

$$\nabla^2 \phi = 0. \tag{15}$$

To determine the potential distribution on the surface of the steel, one must solve Eq. (15) subject to prescribed boundary conditions. The boundary conditions comprise the relationship between potential and current density for the anodic and cathodic regions as well as prescribed current densities. For the anodic and cathodic regions of the steel surface, the boundary condition are defined as $\phi = \phi_a$ and $\phi = \phi_c$, where ϕ_a and ϕ_c are polarized anodic and cathodic potentials which can be expressed as (Stern and Geary, 1957):

$$\phi_a = \phi_{Fe} + \beta_a \log \frac{i_a}{i_{oa}} + i_a R_e , \qquad (16)$$

$$\phi_c = \phi_{O_2} + \beta_c \log \frac{i_c}{i_{oc}} - \frac{2.303RT}{zF} \log \frac{i_L}{i_L - i_c} + i_c R_e$$
, (17)

where ϕ^o_{Fe} and $\phi^o_{O_2}$ are the standard half-cell potentials of Fe and O₂, respectively, β_a is the Tafel slope of the anodic reaction, and i_{0a} is the anodic exchange current density, β_c is the Tafel slope of the cathodic reaction, i_{oc} is the exchange current density of the cathodic reaction, i_L is the limiting current density, and R_e is the resistance (Ohms) of the pore solution around the cathodic sites. For more information about the polarization behavior of steel, reference can be made to Uhlig and Revie (1985) and Stern and Geary (1957). The prescribed current boundary conditions on the steel surface are non-linear because current densities i_a and i_c are functions of the polarized potential, which is the state variable of Eq. (9). In the following sections, we will present our solution strategy to solve this problem in order to determine the corrosion rate in a given structure.

Eq. (15) is a special case of Eq. (7), hence the finite element formulation of Eq. (7) follows the same steps as those described for Eq. (7). However, due to the non-linear boundary conditions given by Eqs. (16) and (17), Eq. (15) must be solved by using an iterative technique.

3.2.4. Numerical example

To illustrate the accuracy of the proposed procedure, Li's (2001) experimental work is simulated. The experiment consists of a large scale beam, as illustrated in Fig. 14, exposed to a chloride solution on its top surface. To increase the concrete permeability, the beam was precracked by subjecting it to the loading shown. The exposure conditions in the test and other details of the experimental program can be obtained from Li (2001).

Using the input data given in Table 4, the corrosion rate in the top reinforcement is determined using the proposed model. The beam was discretized by 3091 four node elements. Due to space limitations, other details of the simulation are not shown, but Fig. 15(a) compares the predicted and measured half-cell potential values. While in the experiment, the actual amount of corrosion was not measured, in the simulation it was calculated as shown in Fig. 15(b). From Fig. 15(a) we can see that the simulation results are in good agreement with the experimental data.

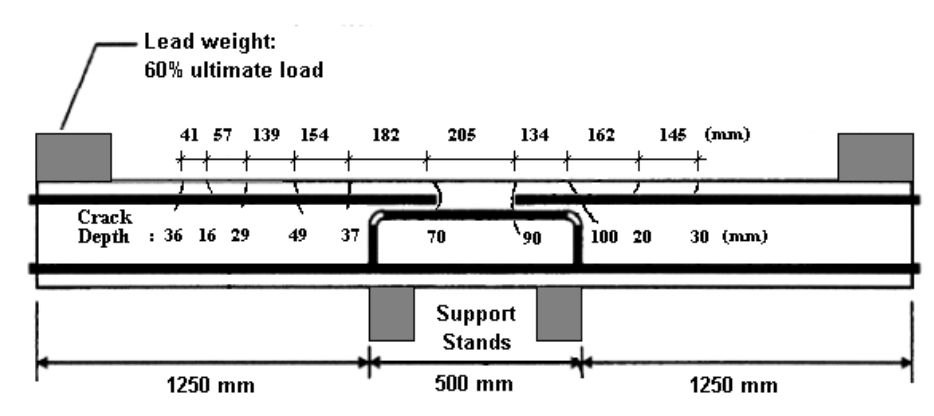


Fig. 14. Geometry and crack distribution of the modelled beam.

Table 4. Parameters used in the proposed model.

Initiation Stage Parameters	Value
Specific heat	1000 J/kg°C
Coefficient of conduction	2 W/m°C
Density of concrete	2400 kg/m^3
Adsorption isotherm	BET
Chloride binding isotherm	Langmuir
Chloride release	No release
Chloride threshold value	0.06% of concrete wt.
Propagation Stage Parameters	Value
Reference concrete resistivity	14000 Ω-cm at 25°C
Initial oxygen concentration	$0.005 kg/m^3 solution$
External oxygen concentration	0.0085 kg/m³ solution
Oxygen diffusion coefficient	Calculated
Fugacity of oxygen	0.2
Cathodic exchange current density	6.25 x 10 ⁻¹⁰ A/cm ²
Anodic exchange current density	1.875 x 10 ⁻⁸ A/cm ²
Thickness of the stagnant layer around the steel surface	0.05 cm
Transference number	1
Cathodic limiting current density	Calculated
Tafel slope for the cathodic reaction	Calculated
Tafel slope for the anodic reaction	Calculated

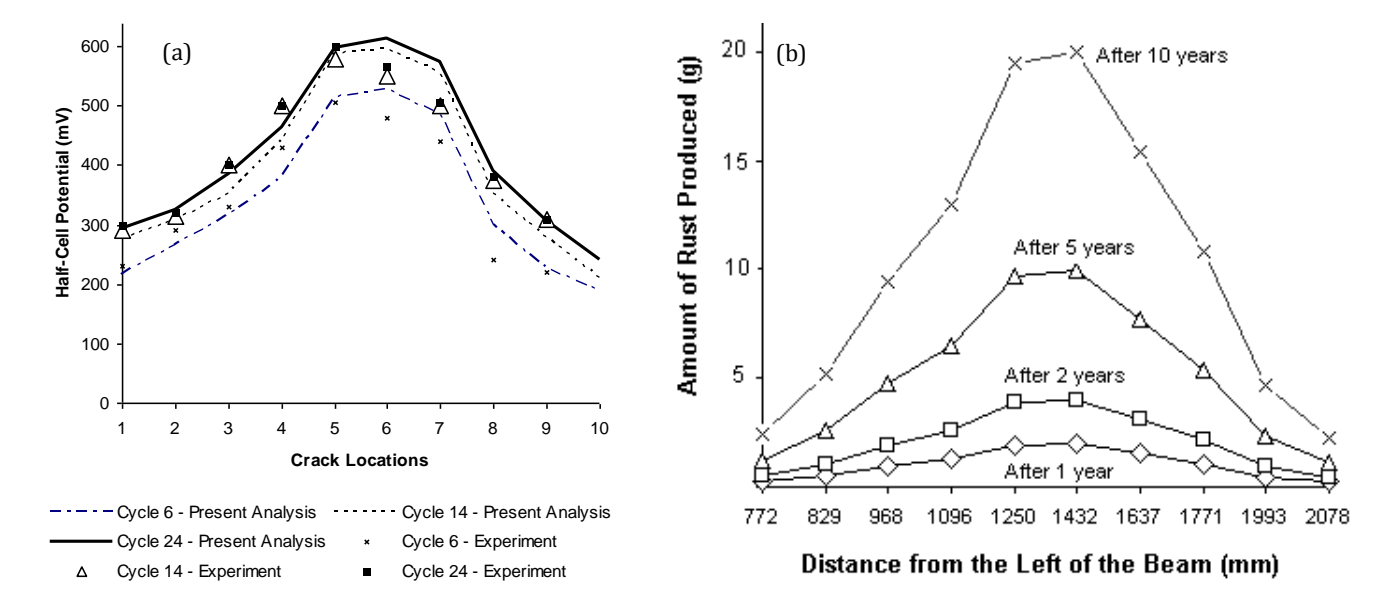


Fig. 15. (a) Comparison of the finite element analysis results for half–cell potential with the experimental data for the beam at the crack locations, (b) Predicted amount of corrosion along the top reinforcement in Li's test beam.

4. Conclusions

Two finite element modelling methods and their experimental validation are presented. The first model deals with the nonlinear response and ultimate strength capacity of composite concrete-steel bridges while the second one deals with durability of reinforced concrete structures, with particular emphasis on the corrosion of reinforcement.

The objective of the paper is to demonstrate that the utilization of suitable theoretical/empirical models, in conjunction with the powerful nonlinear finite element technique, can provide engineers with useful simulation tools, and the ability to predict the response of structures under variable loading, environmental and material degradation conditions. The current results show that although the phenomenon of corrosion in concrete is complex, nevertheless, the electrochemical principles that govern its initiation and propagation can be captured by means of numerical simulations.

REFERENCES

- Broomfield JP (1997). Corrosion of Steel in Concrete. E&FN Spon, London, UK.
- Dhatt G, Touzot G (1984). The Finite Element Method Displayed. J. Wiley & Sons, New York, USA.
- Esfandiari A (2001). Redistribution of Longitudinal Moment in Straight Continuous Concrete Slab-Steel Girder Composite Bridges. *M.Sc. thesis*, Department of Civil and Environmental Eng., Carleton University. Ottawa. Canada.
- Isgor OB, Razaqpur AG (2004). FE modelling of coupled heat transfer, moisture transport and carbonation processes in concrete structures. *Journal of Cement and Concrete Composites*, 26, 57-73.
- Isgor OB, Razaqpur AG (2005). Verification and application of a comprehensive model for predicting steel corrosion in concrete structures. *Proceedings of ConMat '05*, Vancouver, Canada.
- Isgor OB, Razaqpur AG (2006a). Advanced modelling of concrete deterioration due to reinforcement corrosion. *Canadian Journal of Civil Engineering*, 33, 707-718.

- Isgor OB, Razaqpur AG (2006b). Modelling reinforcement corrosion in concrete structures. *International Journal of Materials and Structures*, 39, 291-302.
- Kupfer H, Gerstle KH (1973). Behavior of concrete under biaxial stresses. *Journal of the Engineering Mechanics Division, ASCE*, 99(4).
- Li CQ (2001). Initiation of chloride-induced reinforcement corrosion in concrete structural members – Experimentation. ACI Structural Journal, 98(4), 502-510.
- Logan DL (1992). A First Course in Finite Element Method. PWS Publishing, Boston, USA.
- Martín-Pérez B (1999). Service Life Modeling of RC Highway Structures Exposed To Chlorides. *Ph.D thesis*, University of Toronto, Toronto, Canada.
- Maruya T, Hsu K, Takeda H, Tangtermsirikul S (2003). Numerical modelling of steel corrosion in concrete structures due to chloride ion, oxygen and water movement. *Journal of Advanced Concrete Technology*, 1(2), 147-160.
- Munn RS (1982). A mathematical model for galvanic anode cathodic protection system. *Materials Performance*, 21, 29-41.
- Neville A (1996). Properties of Concrete. 4th ed., J. Wiley & Sons, New York, USA.
- Razaqpur AG, Nofal ME (1988). Transverse load distribution at ultimate limit states in single span slab on girder bridges with compact steel girders. Final Report, Proj: 23182, Ministry of Transportation of Ontario, Downsview, Ontario.
- Razaqpur AG, Nofal M (1989). A finite element for modeling the nonlinear behavior of shear connectors in composite structures. *Journal of Computers and Structures*, 32(1), 169-174.
- Razaqpur AG, Nofal M (1990). Analytical modeling of nonlinear behavior of composite bridges. *Journal of Structural Engineering*, ASCE, 116(6), 1715-1733.
- Stern M, Geary AL (1957). Electrochemical polarization: a theoretical analysis of the shape of the polarization curves. *Journal of the Electrochemical Society*, 104(1), 56-63.
- Turner MJ, Clogh RW, Martin HC, Topp LJ (1956). Stiffness and deflection analysis of complex structures. *Journal of Aeronautical Science*, 23, 805-823.
- Tuutti K (1982). Corrosion of Steel in Concrete. Technical Report, Swedish Cement and Concrete Research Institute, Stockholm.
- Uhlig HH, Revie RW (1985). Corrosion and Corrosion Control. 3rd ed., J. Wiley & Sons, New York, USA.
- Yam LCP, Chapman JC (1972). The inelastic behavior of continuous composite beams of steel and concrete. *Proceedings, Institute of Civil Engineers*, 53, 487-501.
- Zienkiewicz OC, Taylor RL (1989). The Finite Element Method. Vol. 2, 4th ed., McGraw-Hill International, UK.



Resolution of torsional effects in prestressed girders of railway viaducts through use of diaphragms or proper section design

Niyazi Özgür Bezgin*

Deparment of Civil Engineering, İstanbul University, 34320 İstanbul, Turkey

ABSTRACT

Need for elevated railways may arise when capacity of bus transit and light rail transit that share the right of way with roadways becomes insufficient and the cost of railways with dedicated right of ways such as underground railways becomes costly. A similar need arose in the city of Makah and in 2010 an 18-km long; elevated railway transit service began servicing between the districts of Mina, Arafat and Muzdalifah. Today the two-track elevated system serves along the route constructed by posttensioned 25-m long U-sections spanning between piers. This paper presents the analytical studies and the finite element model of an alternative 30-m long pretensioned boxed-section evaluated during the tender stage. Following a comparison with the applied choice, benefits of the U-section with respect to the analyzed alternative will be discussed.

ARTICLE INFO

Article history:
Received 12 August 2015
Accepted 28 September 2015

Keywords: Railways Elevated railways Prefabrication Prestressing Viaducts

1. Introduction

Makah is an important religious city with a population of 1.6 million residents. The roadway networks between the religious sites became insufficient under the increased transportation demand especially during the holy month of Hajj and months of Umrah. Population of the city increase roughly 2 million during the month of Hajj. The capacity of the roadway between the holy sites of Mina and Arafat was insufficient to supply the increased demand during the holy months and therefore an increased mass transit capacity through a two-track elevated railway was proposed.

As a part of the Makah Metro, the 18 km long section between Mina and Arafat serves along 9-stations. Fig. 1 shows the plan of the route that opened to service in November 2010 (Wikipedia, 2015).

The 12-wagon trains serving along the tracks can carry 250 passengers in each wagon and with 24-trips per hour; the capacity of the railway is 72,000 passengers per hour (Railway Technology, 2015).

The route supported by a viaduct today is composed mainly of 25-m long prestressed sections. However during the tender stage of the project an alternative viaduct composed of 30 m long sections were evaluated to reduce the number of spans and the number of supporting piers. This study presents a 3D finite element model of the proposed section and structural analysis for the effects of the expected torsion along the section (Bezgin, 2008).

2. The Proposed Cross-Section of the Track

Fig. 2 presents the section evaluated in the 2008 tender study. The evaluated section is composed of a prefabricated section with $0.95~\text{m}^2$ cross section area and a shaded cast in place slab section with $1~\text{m}^2$ cross section area that is composite with the prefabricated section (Bezgin, 2008). Figure also shows the vertical location of the center of gravity of the composite section.

The moment of inertia of the prefabricated section and the composite section is $0.24~\text{m}^4$ and $0.58~\text{m}^4$ respectively. Mass of the 30 m long prefabricated girder and the composite girder with the cast in place deck is 71 Ton and 146 Ton respectively.

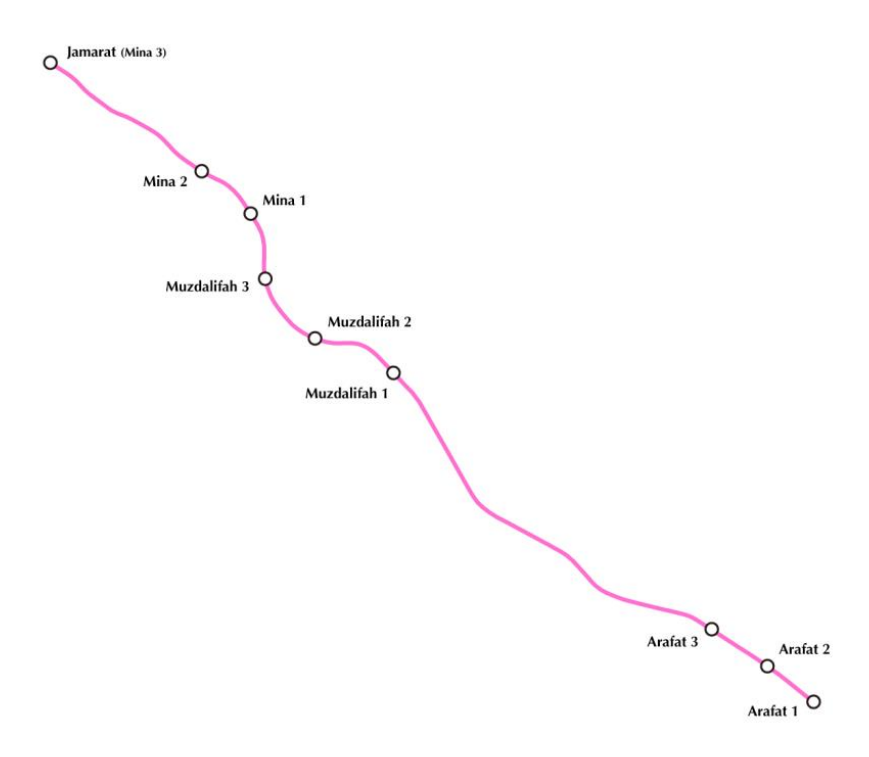


Fig. 1. Elevated railway plan of the proposed route (Wikipedia, 2015).

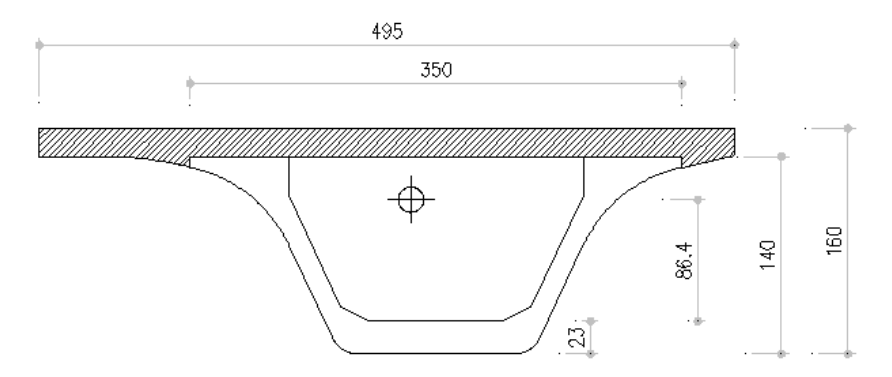


Fig. 2. Evaluated cross-section.

3. Loads Acting on the Girder

Fig. 3 shows the general attributes of the designed track. The track that is supported by special L-shaped beams cast in place with the slab is flanked to the left by a cable duct that also serves as a platform.

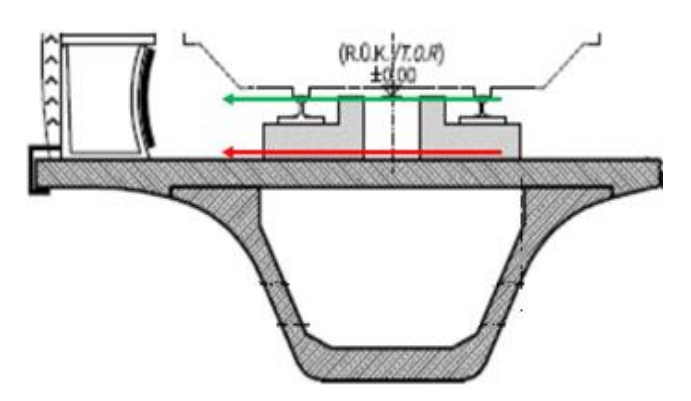


Fig. 3. General attributes of the track cross-section.

The design speed of the train is 80 km/h and the design static axle load is 17 Ton. Dynamic load factor is considered as 1.3 and the quasi-static estimate of the dynamic wheel load is 11 Ton (Lichtberger, 2011). For a design radius of 500 m, the centripetal loads are estimated as 5.3 Ton/axle. Additional dead load on the composite girder due to rail-beams, cable ducts and railings is 0.6 Ton/m. Eq. (1) represents the value of the equivalent load couple acting at the ends of the cross-section, representing the moment generated as the lateral loads applied at the railheads induce a longitudinal bending action at the slab surface 25 cm below.

$$F * 4.9 m = 5400 kg * 0.25 m$$

$$\rightarrow F = 276 kg = 0.3 Ton,$$
(1)

Fig. 4 shows the vertical and lateral axle loads applied onto the girder. Longitudinal loads due to acceleration and deceleration is estimated at 15% of the vertical loads (Lichtberger, 2011).

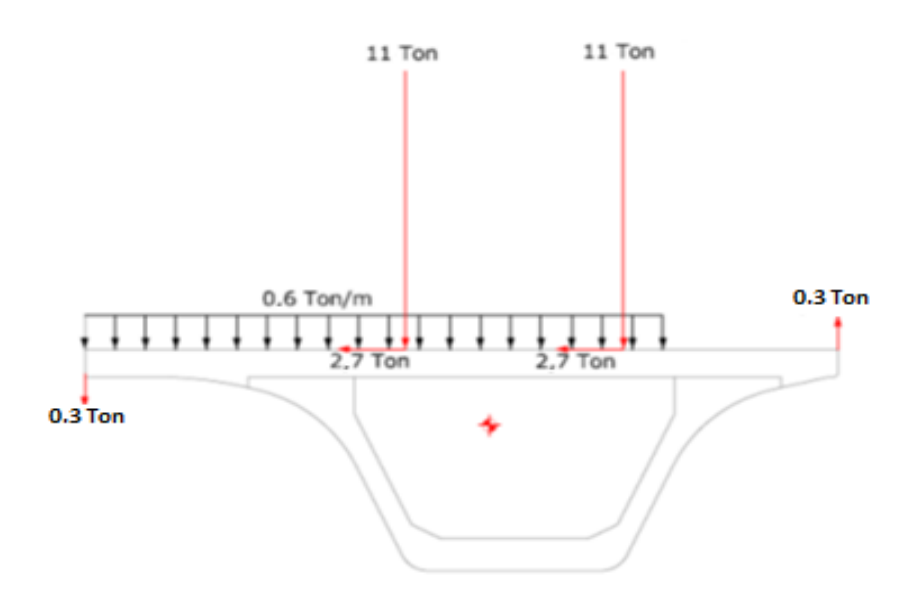


Fig. 4. Application of vertical and lateral loads on the cross section (Bezgin, 2008).

4. Finite Element Analysis of the Prestressed Girder Under the Action of Estimated Loads

A long-term prestressing loss under the humidity and temperature conditions of Makah was estimated at 35%. Fig. 5 shows the perspective view of the design prestressed girder with estimated initial 140 kN initial prestressing force. Using the linear and elastic analysis

capability of the SAP2000 program, the prestressing forces were introduced at the respective nodes into the section along the transfer lengths of the prestressing wires as shown in Fig. 6. The model was generated by 8-node linear solid elements. The estimated prestressed force is introduced into the section as shown in Fig. 6 along a transfer length of 130 cm through count-74, 1.6 cm diameter wires with 1800 MPa tensile strength (PCI, 1992).

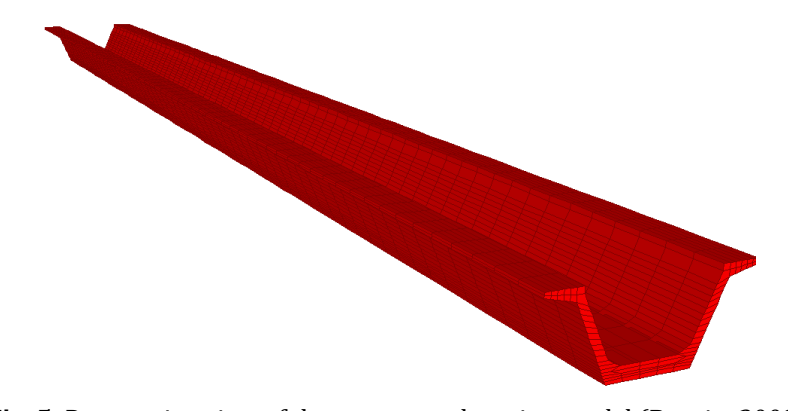


Fig. 5. Perspective view of the prestressed section model (Bezgin, 2008).



Fig. 6. Prestressing forces introduced into the section gradually from its ends (Bezgin, 2008; PCI, 1992).

Under the initial prestressing force, a maximum 2.7 cm camber with a deflection to span ratio L/1100 occurs in the girder as shown in Fig. 7.

Following the placement of the prestressed girder between the piers, cast in place slab is placed, which is modeled as shown in Fig. 8.

After the prestressing losses and the added weight of the cast in place slab, camber is reduced to 0.9 cm with a ratio to girder span of L/3300.

Under the action of the axle loads shown in Fig. 9, the net deflection shown in Fig. 10 is 0.75 cm with a ratio to girder span of L/4000.

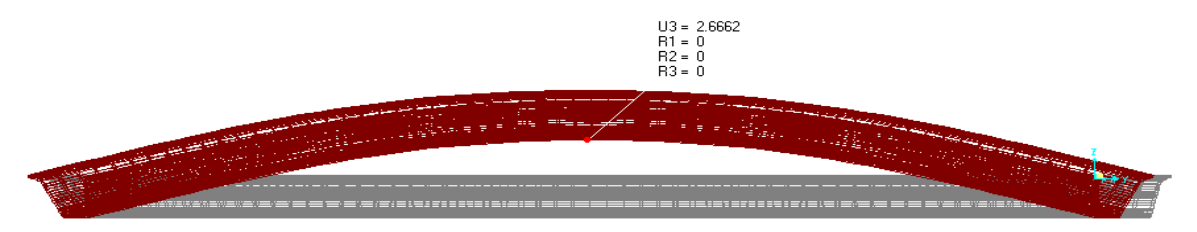


Fig. 7. Inverse camber due to prestressing (Bezgin, 2008).

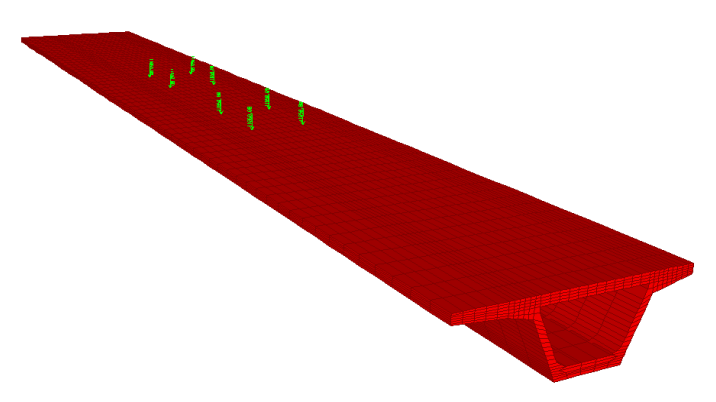


Fig. 8. Cast in place slab and the application of axle loads at the midspan (Bezgin, 2008).

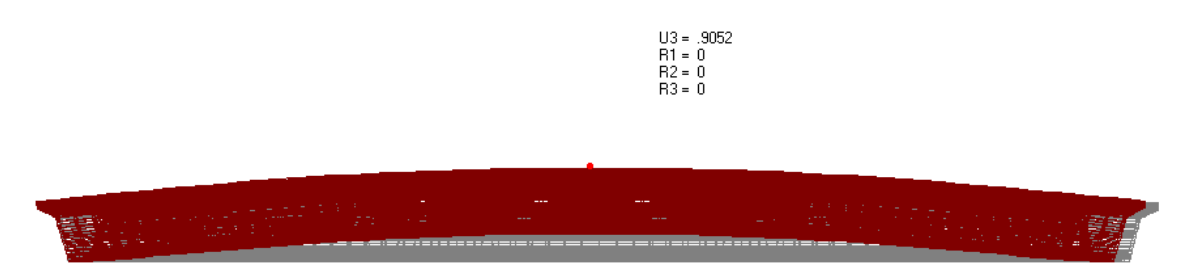


Fig. 9. Remaining inverse camber after the placement of cast in place slab and prestressing losses (Bezgin, 2008).

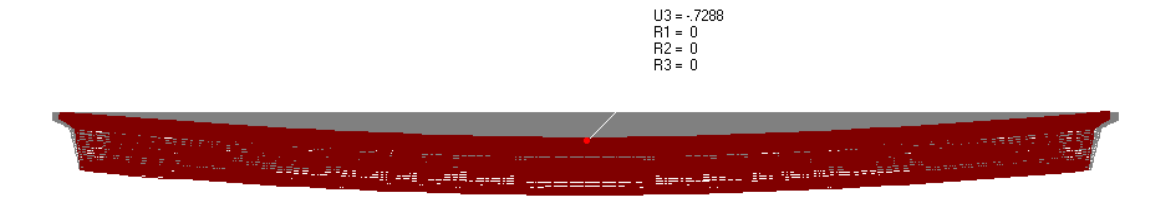


Fig. 10. Net deflection after the addition of the dynamic live loads due to wheel loads (Bezgin, 2008).

Fig. 11 shows the model under the application of the lateral loads that occur at the curvatures along the route in addition to the vertical loads shown in Fig. 8.

The induced torsion distorts the section as shown in Figs. 12-14 shows the distribution of torsional tensile stresses, maximum values of which can be as high as 5 MPa that can crack the C40 grade concrete section. The vertical displacement of the left and right sides of the section at mid-span are 1.3 cm and 0.5 cm respectively. However, since the section is likely to have cracked at these levels of stresses, the displacements and the accompanying torsional rotations are expected to be higher.

Diaphragms placed perpendicularly to the longitudinal axis of the girder can be used to limit the development of torsional distortions and thus the development of torsional stresses along the girder. With 30 cm thick count-4 diaphragms placed at the girder supports, at L/3 and 2L/3 of the span length (L) reduced the vertical

displacement at the left and right sides of the mid-span cross section to 0.13 cm and 0.05 cm respectively. Fig. 15 shows the perspective of the prestressed girder with the diaphragms. Fig. 16 shows that the torsional tensile stresses observed in Fig. 14 are drastically reduced due to the presence of the diaphragms resisting distortion due to torsion.

5. Conclusion

Following the tender stage, the owner of the project elected to apply the 25 m long posttensioned girder solution, the cross-section for which is shown in Fig. 17. The section that is fully prefabricated has a cross section area of 2.2 m 2 and a reduced moment inertia that is roughly 70% of the proposed section. Fig. 18 shows the double track cross section and Fig. 19 shows a perspective where the two tracks diverge.

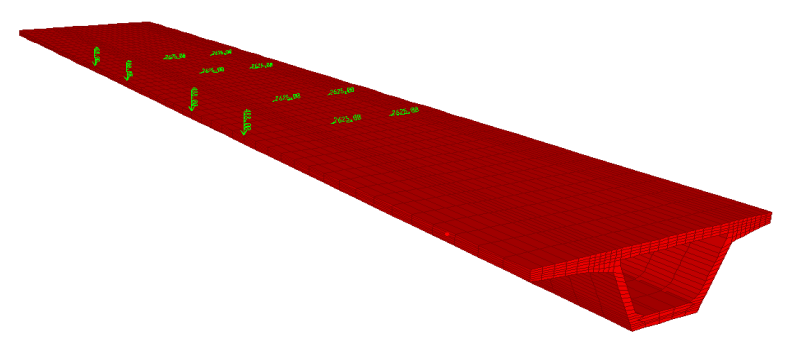


Fig. 11. Application of the lateral and torsional loads in addition to the vertical loads (Bezgin, 2008).

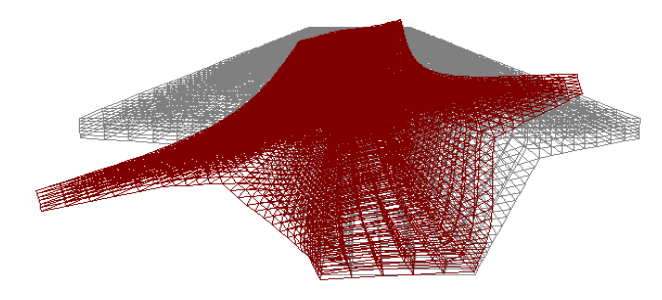


Fig. 12. Perspective view of torsional distortion along the girder (Bezgin, 2008).

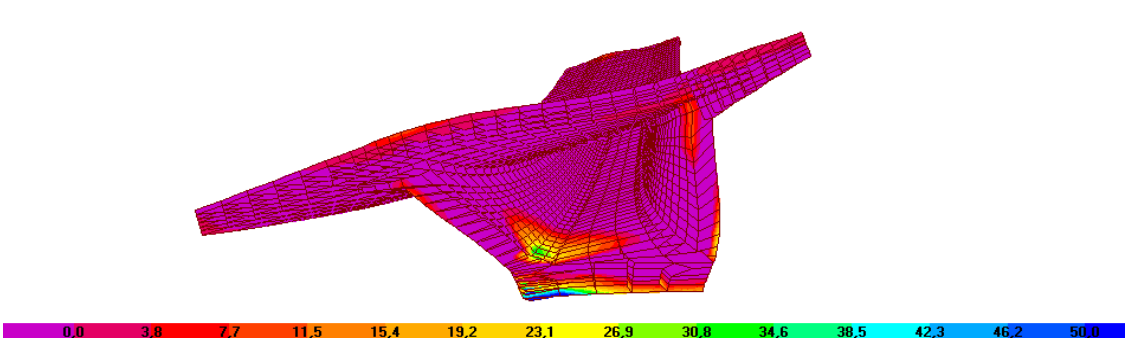


Fig. 13. Tensile stresses due to torsion at the ends of the girder (Bezgin, 2008).

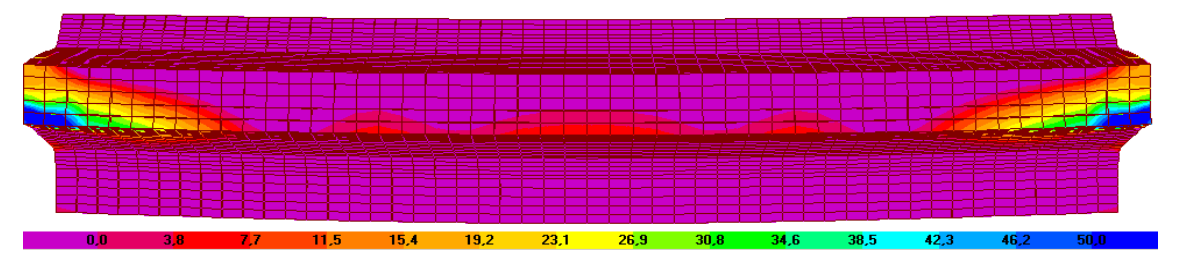


Fig. 14. Tensile stresses due to torsion along the bottom of the girder (Bezgin, 2008).

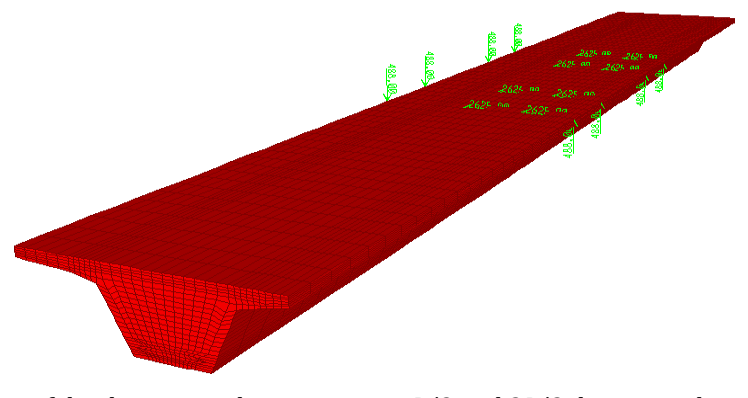


Fig. 15. Use of diaphragms at the supports, at L/3 and 2L/3 distances along the span (L).

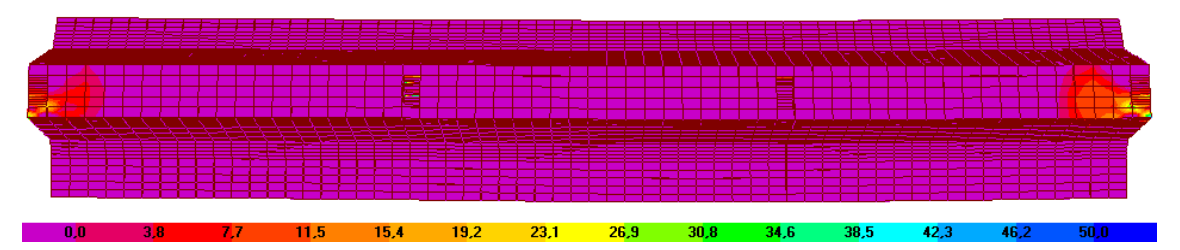


Fig. 16. Reduced torsional stresses with the use of diaphragms (Bezgin, 2008).

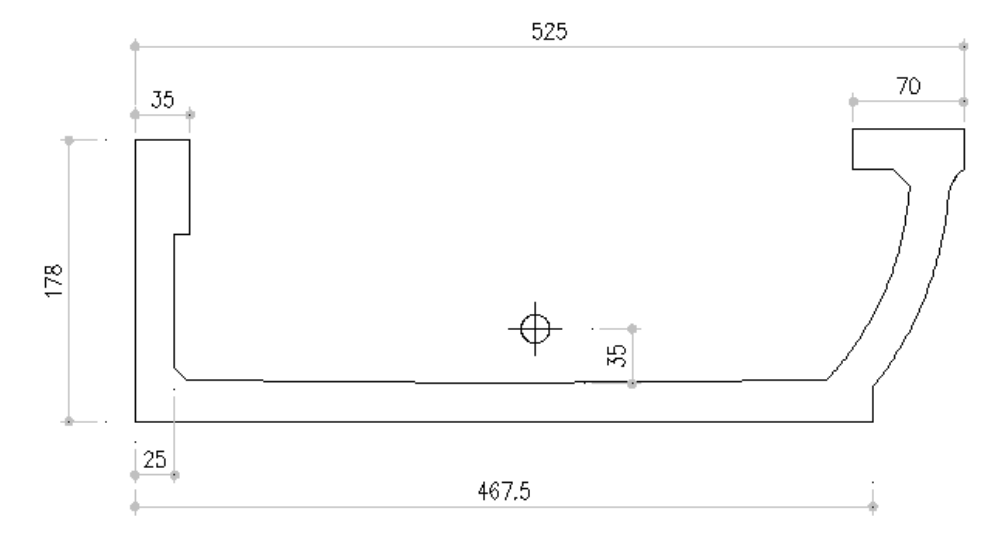


Fig. 17. Preferred section and its center of gravity (Bezgin, 2008).

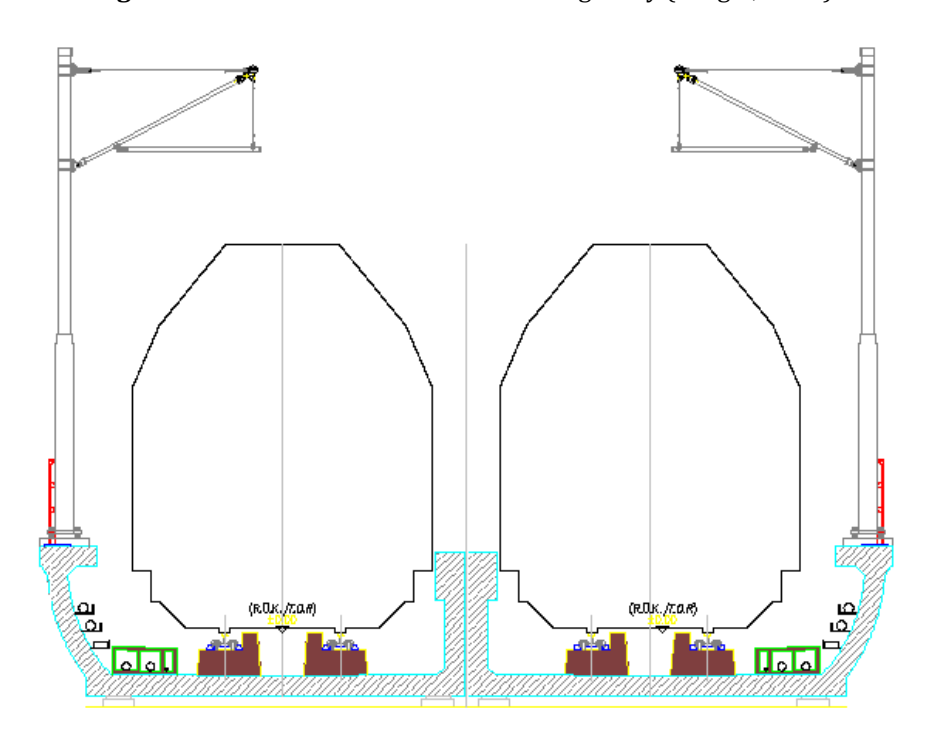


Fig. 18. Cross-section of the two-track railway with the preferred cross-section (PCI, 1992).

Although the elected cross section is heavier and has a lower bending stiffness with a need for increased number of spans along the route it has some significant benefits that the evaluated section does not have. Firstly, the elected solution encompasses the track structure thereby suppressing the emanation of noise due to wheel and track interaction.

Secondly, the elected section lowers the elevation of the tracks thereby reducing the height of the elevated stations from the ground level. Thirdly, the section is fully prefabricated including the rail beams, thereby eliminating the site work required for the cast in place operations, which would be particularly difficult under the high temperatures of the project site.



Fig. 19. A perspective view of the route (PCI, 1992).

Lastly, the problem of torsion is resolved within the geometry of the section. According to Fig. 17, the center of gravity of the section is 35 cm above the top face of the bottom part of the girder. The rail beams are also fabricated with the section such that the top elevation of the rails is also 35 cm above the top face of the bottom part of the girder. Therefore, the lateral forces applied at the railheads pass directly through the center of gravity of the section thus preventing torsion.

In Fig. 3 of the evaluated section, the lateral forces are transferred to the top of the slab via the rail beams at a location that is 50 cm above the center of gravity of the section. The generated torsion is resisted through the diaphragms. However, rather than generating and resisting torsion, it is better to use a design that prevents torsion in the first place.

REFERENCES

Bezgin NÖ (2008). Makah, Mina-Arafat Elevated Railway Track Design Report. Yapı Merkezi Prefabrication Inc., İstanbul, Turkey.

Lichtberger B (2011). Track Compendium. Eurail Press, Hamburg, Germany.

PCI (1992). PCI Design Handbook. Precast/Prestressed Concrete Institute, Chicago, Illinois, USA.

Railway Technology (2013). http://www.railway-technology.com/projects/al-mashaaer-al-mugad. Al Mashaaer Al Mugaddassah Metro Project, Saudi Arabia. Downloaded on 17-01-2013.

Redgage (2014). http://www.redgage.com/photos/mohamadi/mak-kah-mecca-metro-railway.html. Makkah (Mecca) Metro Railway. Downloaded on 6-11-2014.

Wikipedia (2015). http://en.wikipedia.org/wiki/Al_Mashaaer_Al_Mugaddassah_Metro. Al Mashaaer Al Mugaddassah Metro Project, Saudi Arabia. Downloaded on 20-03-2015.



Dynamic vibration analysis of ballastless track: Istanbul Aksaray-Airport LRT System

Veysel Arlı^a, Turgut Öztürk^{b,*}, Zübeyde Öztürk^b

- ^a Department of Track & Fixed Facilities, İstanbul Transportation Co., 34220 İstanbul, Turkey
- ^b Department of Civil Engineering, İstanbul Technical University, 34469 İstanbul, Turkey

ABSTRACT

In this study, ballastless superstructure with a steel base-plate of light metro track, which lies between Aksaray and the Airport in Istanbul, was analyzed with a numeric method using ANSYS 9.0 finite element software. Since the railroad superstructure has a symmetric structure with respect to the track axis, a rail system that consists of a single rail and a half sleeper was modeled to simplify the computations in this analysis. In the discrete supported track model, the rail was modeled as an Euler-Bernoulli beam and steel base-plate, and it was assumed to be a rigid mass. Dynamic computation results and graphs were determined by performing harmonic analysis with the aid of ANSYS software. A field vibration survey was conducted to determine the natural frequencies of the railroad and the dynamic receptance behavior, and to validate the finite element model according to the measurement results. The frequency receptance behavior of the rail and the support was measured by applying a hammer impact load on the rail head in the field, and the finite element model of the ballastless track with steel base-plate was verified.

ARTICLE INFO

Article history: Received 13 May 2015 Accepted 18 July 2015

Keywords:
Finite element method
Numeric analysis
Dynamic analysis
Ballastless track
Vibration analysis

1. Introduction

When all systems that contain potential and kinetic energy are disturbed with dynamic loads, they start to vibrate. Dynamic loads and vibration occur due to irregularity and roughness during the contact between the rail and the wheel on a track superstructure, and the vibrations are conveyed both to the vehicle and the superstructure in all three axial directions. When resonance occurs, undesirable degradations and deformations affect vehicle stability, passenger comfort, and road and vehicle components; thus, the excitation frequency, or the natural frequency, of the system should be altered to prevent resonance. Since changing the natural frequency of the system as an afterthought is technically and economically difficult, it is appropriate to do it during the design stage. Therefore, numerical analyses must be performed that use finite element models and determine the dynamic effects during the resonance. In addition, field vibration surveys should be conducted, and the natural

frequencies of the track should be measured to support and validate the dynamic analysis.

There are various excitation sources in the vehicles that cause oscillations, vibrations and noise on the railroad and in the environment. These include geometric defects, irregularities on the surface of rails and the wheel, fishplate rail joints, switch and crossing, and changing track rigidness. If the defect fits the sine curve, the excitation frequency of the defect, depending on the wave length (λ) and vehicle velocity (V), can be calculated using Eq. (1).

$$f = V/\lambda, \tag{1}$$

As seen in the equation above, frequency decreases as the wave length increases; geometric track defects with large wave lengths cause low frequency vibrations, and rail corrugations with short wave length cause high frequency vibrations. The relationship between railroad vehicles and the track is a very complicated system that includes many degrees of freedom. Lots of modeling, field surveying and laboratory work has examined dynamic vehicle-track interaction. Since, the vehicle-track system is an ambiguous one that displays variations; these studies were simplified by making basic assumptions. Thus, while the rail-wheel contact surface may change due to rail or wheel profile defects, and granular materials, such as ballast and soil, display plastic behavior, most of the research on railroad dynamics assumes that materials show linear elastic behavior, and material properties are obtained with field and laboratory tests.

The models should be as simple as possible and reliable enough to serve their purpose. Linear models, which produce quick solutions in frequency domain, are usually used for simplicity. The reliability of the model is dependent on disregarded, but important, effects: false loading or defect assumptions, or wrong system parameters. Methods should be applied to avoid these errors, and the model should be validated with experimental studies. In short, there is no model solely sufficient for a system, and as a result, various models are used for various purposes.

The first step in modeling complex dynamic systems is to establish discrete models for components such as the wheel, elastic layer or sleeper. These models are combined to define sub-systems, and then the entire vehicle-track system is modeled by combining the sub-systems. When modeling the railroad superstructure, generally the frequency interval 20-1500 Hz is used for vibration analyses. The primary cause of problems pertaining to track components and the rolling surfaces of wheel and rails is the vertical forces. Vertical forces are loads with high frequency, and they appear due to irregularities with short wave lengths; they become critical at frequencies below 1500 Hz.

The vehicle excitation load is usually modeled in four different ways (stationary load model, moving load model, moving irregularity model, moving mass model) (Diana et al., 1994). The most appropriate model for comparing the computed and measured values of excitation forces on the tracks, which are stimulated with a periodic (e.g., vibrator) or short-termed (impact hammer) force applied on a fixed point, is the stationary load model. While the railroad superstructure is usually modeled as a two-dimensional infinite beam on an elastic foundation that consists of separate rails, the wheel load is modeled as a force that moves discretely. This model is linear elastic, and the effect of neighboring wheels is computed with the superposition method. Supporting the rails is basically done with two approaches, which require either discrete or continuous support.

A track model with continuous support was first used by Timoshenko in 1926, followed by studies by Heteny (1946), Sato (1977), Grassie (1980), and Tassily (1988). On the other hand, discrete support track model was used by Inglis (1938), Grassie et al. (1982), Nielsen (1990), Ripke (1991), Knothe and Grassie (1993). The most commonly used method is to position the rails on parallel spring and damping elements. This spring-damping element models the elastic rail layer, as the supports sit on the elastic foundation, which is another spring-damping element system.

In this study, the dynamic computations of the ballastless superstructure of the Istanbul Aksaray-Airport light track were carried out with a numerical method and the use of ANSYS 9.0 finite element software, and graphical results were obtained. In modeling with finite elements methods, the wheel was applied both above and between two supports. A field vibration survey was conducted to determine the natural frequencies of the railroad and the dynamic receptance behavior and to verify the finite element model according to the measurement results. This study is different and unique compared to previous studies in terms of its approach and results. In this study, comparisons are made for a railroad using a finite elements method and field surveying results, along with a parametric study. The effect of different track parameters on dynamic behavior was analyzed as well. It is also important to investigate the effect of different track parameters on vibrations to achieve the most appropriate design in the vehicle-track-environment system in terms of vibration, particularly during the design stage (Dahlberg, 2002; Diana et al., 1994; Grassie, 1993, 1996; Popp and Schiehlen, 2003).

2. Dynamic Vibration Analyses with Using a Numerical Method

In this section, numerical dynamic vibration analysis is applied to selected track models; a ballastless (with concrete paving) superstructure with a steel base plate, which is used in rail systems in Istanbul downtown, was selected for the track model. Hence, the track model with discrete support was analyzed using ANSYS finite element software. In the track model with discrete support, rails are modeled as Euler-Bernoulli beams and steel base-plates as rigid masses, as seen in Fig. 1. Harmonic analysis was conducted using ANSYS software, and the results and graphs of dynamic computations were obtained. A harmonic load would cause harmonic receptance on the structural system. Harmonic receptance analysis enables the continuous dynamic behavior of the vehicle to be determined; as a result, the ability of the design to successfully withstand resonance, fatigue, and other harmless effects of constrained vibration is revealed. Harmonic receptance analysis is a technique that is used to determine steady-state receptance against sinusoidal (harmonically) changing loads of a linear structure. The purpose of this analysis is to estimate the receptance of the structure at various frequencies and plot it. Transient vibrations, which emerge at the start of stimulation, are not included in the harmonic receptance analysis, (Sato et al., 1998; Knothe and Grassie, 1993; Grassie and Kalousek, 1993).

The railroad superstructure is modeled with the elements contained in the elements library of ANSYS 9.0, which is finite elements software. Since railroad structure has a symmetrical structure compared to the track axis, a track system consisting of a single rail and half sleeper was modeled for ease during calculations. In the finite element track model, which is displayed in Fig. 1, rails are established as two-dimensional beam elements with finite length, and sleeper masses are connected to

the nodes of the beam element. Rails were modeled with BEAM3 elastic beam elements with two degrees of freedom (vertical displacement and rotation), sleepers were modeled with equivalent singular mass elements and elastic layers, and the ballast layer was modeled with COMBIN14 spring-damping elements. A total of 1863 elements were used for 30 sleeper intervals, and 152 nodes were formed in the model. Since there are two degrees of freedom for each node, this corresponds to 304 degrees of freedom, and the parameters of the model are presented in Table 1 (Arlı, 2009).

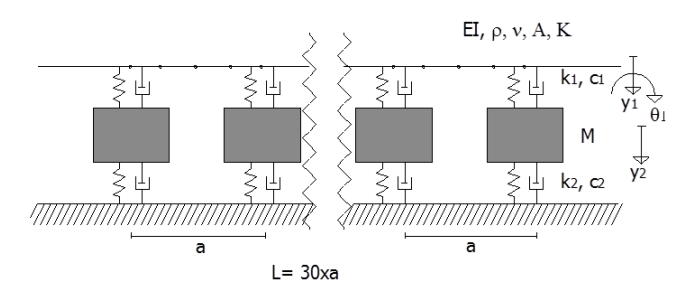


Fig. 1. Finite elements track model.

Table 1. Parameters of the track model used in the study.

Moment of inertia of the rail	I=1819e-8 (m ⁴)
Cross section of the rail	A=6297e-6 (m ²)
Shear factor of the rail	K=0.35
Modulus of Elasticity	E=2.1e11 (N/m ²)
Density	ρ =7850 (kg/m ³)
Poisson's ratio	v=0.3
Base-plate distance	<i>a</i> =0.75 (m)
Steel base-plate mass	m=8 (kg)
Stiffness coefficient of the elastic layer under rail	k _p =970e6 (N/m)
Damping coefficient of the elastic layer under rail	c_p =32e3 (Ns/m)
Stiffness coefficient of the elastic layer under base-plate	k₃=90 e6 (N/m)
Damping coefficient of the elastic layer under base-plate	cs=4.1e3 (Ns/m)

In the numerical analysis, the effects of various track parameters on dynamic behavior are computed for the frequency interval 0-1500 Hz, and dynamic receptance graphs were obtained. While modeling with the finite elements method, the wheel load was applied both above the support and between two supports. When the wheel was exactly on the sleeper, the dynamic receptances of the rail and sleeper were determined, and it was observed that their receptances were different for this case. The dynamic receptance graph of the track was obtained for the unit wheel load. In the dynamic receptance graph of the harmonic analysis, peak values show a resonance event and accordingly show the natural frequencies of the track. Track and support natural frequencies were calculated out of these graphs (Table 2).

Table 2. Natural frequencies of ballastless track model.

Track parameter	Track natural freq.	Support natural freq.
Ballastless track model	216Hz	756 Hz
Base-plate mass (10kg)	213 Hz	756 Hz
Base-plate distance (0.60m)	246 Hz	1161 Hz
Elastic layer type under baseplate (1403-N)	282 Hz	762 Hz

Since the harmonic analysis was carried out for every 500 points within the 0-1500 Hz frequency interval, graphic results have a frequency resolution of 3 Hz. The number of points could be increased for more precise analysis, but the analysis duration would also increase in this case.

According to the dynamic analysis, when the natural frequencies of the ballastless track are the same as the excitation load, the dynamic effects increase with resonance. Natural frequencies for the ballastless track models were obtained from frequency-dynamic receptance graphs. The first peak value on the dynamic receptance graph of a rail and support at the support point shows the track natural frequency, while the secondary peak values show the rail natural frequency. In the dynamic receptance graph of the rail between two supports, two peak values are observed, and the first value specifies the track natural frequency while the second one specifies the support natural frequency. Some vital results attained according to Table 1 are:

- The track natural frequency varies depending on baseplate distance and the elastic layer under the base-plate,
- The support natural frequency varies depending on the support interval and elastic layer type under the rail base plate and the base-plate mass has no effect.

In the dynamic receptance graphs of the ballastless track model, it is observed that the ballastless track model has a peak value, and the receptance curves of the rail and base-plate are the same. The dynamic receptance behavior of the rail and base-plate is not the same for the elastic layer under the base-plate, which is more rigid but has a higher damping coefficient (1403-N type, stiffness coefficient $k=171\times10^6$ N/m and damping coefficient $c=17,1x10^3$ Ns/m), and the receptance of the base-plate is less than the rail. In other words, the rail and base-plate do not move together under the wheel load, and the rail has greater vertical displacement than the base-plate. Because the damping coefficient of the elastic layer is greater, the dynamic receptance of rail and base-plate is less than the ballastless track model (Figs. 2-9).

In Figs. 2 and 3, dynamic receptance graphs of the ballastless track model at the support point and between two supports are displayed, respectively. These graphs show that the dynamic receptance of the rail between two supports is greater than the dynamic receptance of the rail in the ballastless track model; in other words, more rail displacement occurs. The effect of each parameter (the base-plate mass, base-plate distance and elastic layer type) on dynamic behavior was investigated. The most significant parameter is the elastic layer under the base-plate, and dynamic receptance is substantially reduced as the damping coefficient of the elastic layer increased. In addition, the dynamic receptance, or rail displacement, is also reduced when the support distance is changed from 0.75 m to 0.6 m. Increasing the baseplate mass slightly (10 kg instead of 8 kg) does not immediately affect the dynamic receptance, (Figs. 4-9).

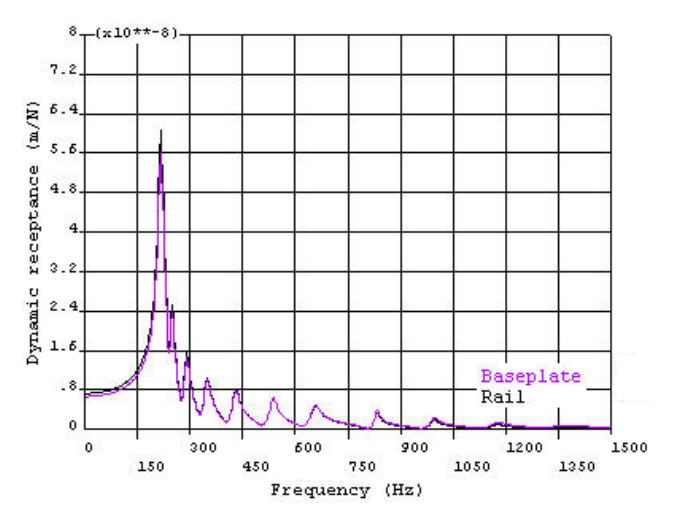


Fig. 2. Dynamic receptance-frequency graph of the rail and the base-plate at the support point.

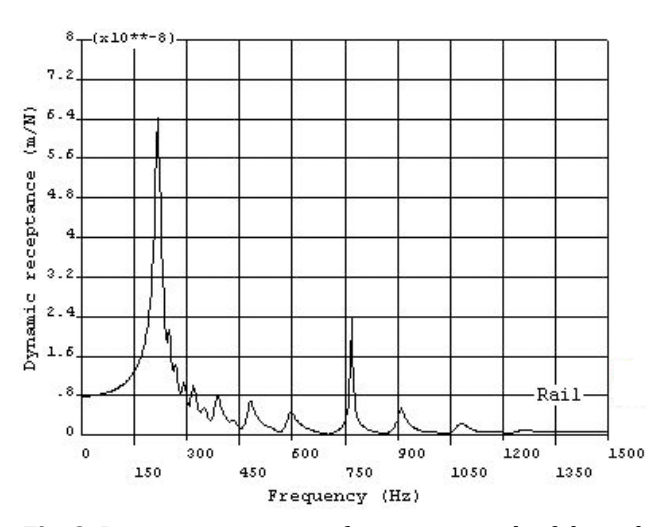


Fig. 3. Dynamic receptance-frequency graph of the rail between two supports.

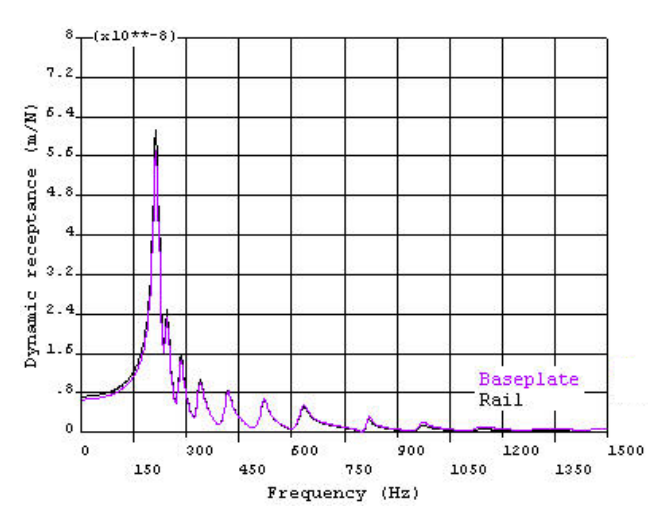


Fig. 4. Dynamic receptance-frequency graph of the rail and the base-plate (*m*=10 kg) at the support point.

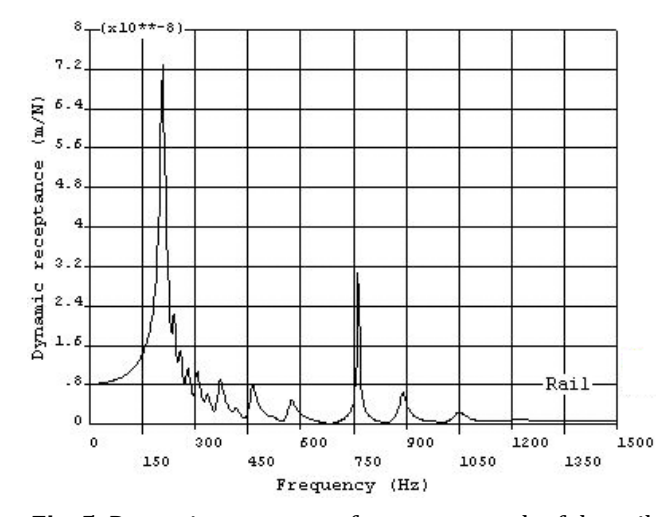


Fig. 5. Dynamic receptance-frequency graph of the rail between two supports base-plate (m=10 kg).

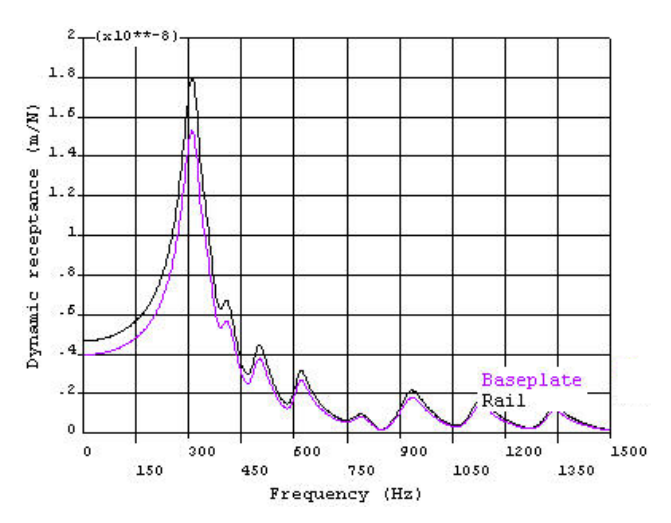


Fig. 6. Dynamic receptance-frequency graph of the rail and the base-plate at support point, 1403-N type.

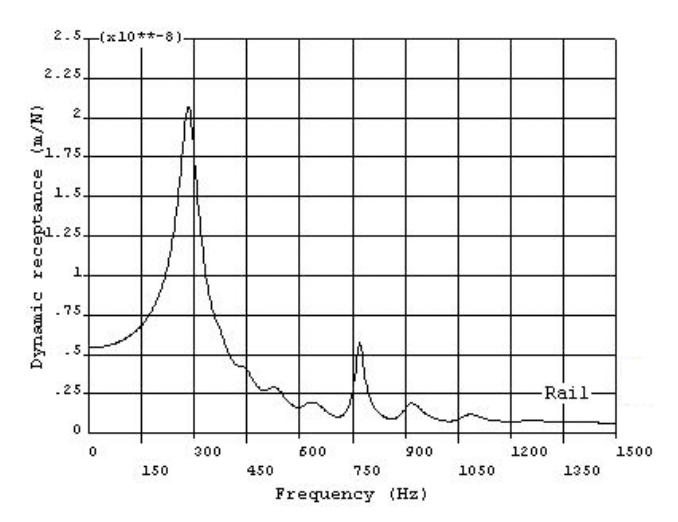


Fig. 7. Dynamic receptance-frequency graph of the rail between two supports elastic layer 1403-N type.

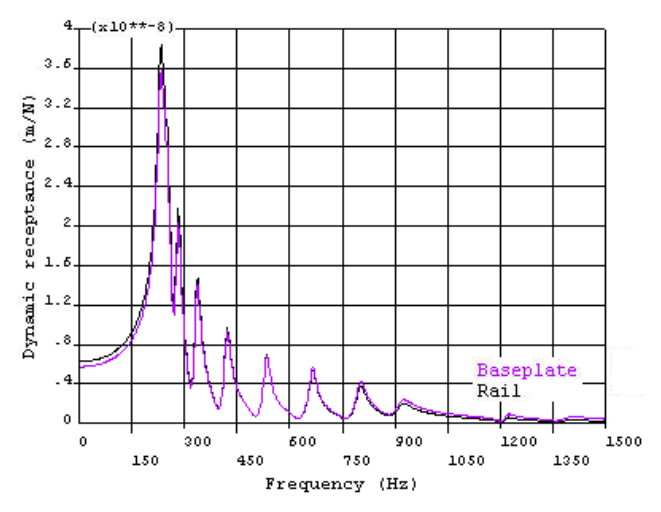


Fig. 8. Dynamic receptance-frequency graph of the rail and the base-plate at support point (a=0.60 m).

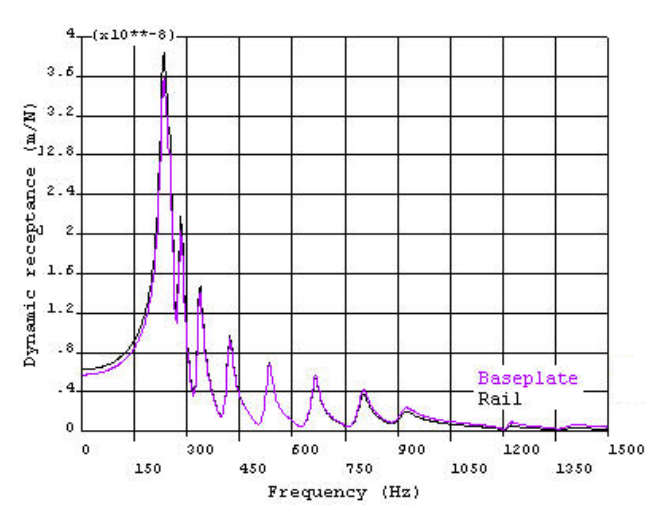


Fig. 9. Dynamic receptance-frequency graph of the rail between two supports, base-plate distance (a=0.60 m).

3. Vibration Measurements in the Track

Vibration measurements were performed to determine the natural frequency and dynamic receptance behavior of the railroad and validate the finite element model based on the survey results. The frequency receptance behavior of the rail and the support (steel baseplate) was measured by applying a hammer impact load on the rail head in the track. Since the dynamic properties of elastic layers in the ballastless track model are unknown, several assumptions were made.

The hammer impact test aims to vibrate the track structure or the specimen. The impact load applied towards a specific direction and at a specific location overbalances the structure briefly. The duration and size of the load defines the distribution of impact energy at all frequency intervals; the contact surface between the hammer and the structure has an effect on this distribution. The hammer impact triggers the data recording, which continues until the vibration stops and balance is achieved again; vibrations are recorded with one or more accelerometers. Normally, all the load and acceleration data are transformed into frequency impact

functions, namely, receptance functions with FFT (Fast Fourier Transform) analysis. While finding the receptance function of the railroad, it is assumed that it is independent from the vehicle load. In other words, it is assumed that the stiffness and damping properties of the track are independent from the vehicle load.

Coherence is used to estimate the repeatability and reliability of acceleration and load measurements. If this value is close to 1, strong coherence exists; if it is between 0 and 0.8, the coherence is not strong, and it is not appropriate to use the results. While resonance frequencies produce correlation values very close to 1, correlation values of anti-resonance frequencies are generally close to zero. The small hammer test generates insufficient correlation below 40 Hz, while the big hammer test generates insufficient correlation above 1400 Hz. For measurements, a Brüel&Kjaer PULSE multi-channel measuring system, Dytran-5803A sledge hammer and power sensor, and a Brüel&Kjaer Type 4396 accelerometer were used. Vibration signals were recorded and analyzed with the aid of a computer.

The measurements were recorded in the vertical direction with an accelerometer, which was magnetically attached under the rails and above the base-plate and sleeper, on the track specified at (km 10+190). A coherence graph was examined for each hammer hit (0-1600 Hz freq.), and the vibration receptance behavior was recorded when there was a proper coherence value. If the proper value was not attained, then impact trials were repeated. The measurements on 21.07.2007 were conducted between 0100 and 0500, which are non-operating hours, to avoid excitation vibrations due to the train. The frequency response and coherence graphs of the rail and the support (steel base-plate) on tracks with and without ballast were obtained. Usually, measurement results between 0 and 20 Hz are not accepted since they have low coherence values. Moreover, it is perceived that since coherence values for several frequency intervals are less than 0.8, they would not be accepted. The natural frequency of the track was obtained as 210 Hz from the graphs; the natural frequency of the support was not estimated. A single peak value is observed from the dynamic receptance graph based on measurement results, and this value indicates the track natural frequency. It is difficult to identify the natural frequency of the rail because there is no significant peak (Arlı 2009).

4. Conclusions

The ballastless superstructure with a steel base-plate of the light metro track, which lies between Aksaray and the Airport in Istanbul, was analyzed with a numeric method using ANSYS 9.0 finite element software in this study. Harmonic analysis was carried out with ANSYS software, and dynamic computation results and graphs were obtained, yielding the following findings:

• In the numerical analysis, the effect of various track parameters on dynamic behavior was estimated for the 0-1500 Hz frequency interval. The natural frequency of the ballastless track varies depending on base-plate distance and the type of elastic layer under the base-plate.

The support natural frequency changes depending on rail type, support distance, and type of elastic layer under the rail/base-plate; base-plate mass has no effect.

- When modeling with the finite elements method, the wheel load was applied both above the support and between two supports. The first peak value on the dynamic receptance graph of the rail and at the support point shows the track natural frequency, while the secondary peak values show the rail natural frequency. In the dynamic receptance graph of the rail between two supports, two peak values are observed, and the first value specifies the track natural frequency, while the second one specifies the support natural frequency.
- A field vibration survey was conducted to determine the natural frequencies of the railroad and the dynamic receptance behavior, and to verify the finite element model according to the measurement results. The frequency receptance behavior of the rail and the support (steel base-plate) was measured by applying a hammer impact load on the rail head in the track. A single peak value is observed on the dynamic receptance graph based on measurement results, and this value indicates the track natural frequency. But it is difficult to identify the natural frequency of the rail.

The finite elements model of the ballastless track with a steel base-plate was validated. Survey results for the ballastless track were remarkably consistent with the finite elements model, and the natural frequency and dynamic receptance values for both of them were found to be very close to each other. This is because there are not any granular materials that have unknown dynamic properties, like the ballast and soil in this superstructure; only elastic layers under rails and steel base-plate are present. Based on the above findings, it is possible to establish dynamic properties fully consistent with measurements, particularly for ballastless track models. Consequently, there is a good chance of precisely determining the dynamic behavior of the track for vehicle and track parameters.

This study is the first in Turkey that combines railroad dynamic analysis and modeling and surveying, and it can be considered as a significant development for urban railroad systems and high speed railroad projects, which have grown in the last several years. It is crucial to analyze the effect of various track parameters (rail type, elastic layer, support distance, etc.) on the dynamic behavior of the railroad, as the ballastless superstructure is preferred for urban rail systems (subway and tramway systems). It is possible to explicate with finite element models validated by field surveys. Deciding on the most fitting design in terms of vibration and determining the natural frequencies of the track during the planning stage is necessary to reduce the negative environmental effects of urban rail systems, which are located very close to areas sensitive to vibration and noise, such as historical structures, residences, hospitals, and schools. Furthermore, future studies should focus on determining the excitation frequencies caused by trains and natural frequencies of nearby buildings.

REFERENCES

Arlı V (2009). Demiryolu Titreşimlerinin Model Hat Üzerinde Çok Yönlü Analizi. *Ph.D. thesis*, İstanbul Technical University, İstanbul, Turkey (in Turkish).

Dahlberg T (2002). Dynamic interaction between train and non-linear track model. *Proceedings of the 4th International Conference on Structural Dynamics, EURODYN2002*, Munich.

Diana G, Cheli F, Bruni S, Collina A (1994). Interaction between railroad superstructure and track vehicles. *Vehicle System Dynamics*, 23, 75-86.

Grassie SL, Kalousek J (1993). Rail corrugation: characteristics, causes and treatments. Proceedings of the Institution of Mechanical Engineers, Part F, Journal of Rail and Rapid Transit, 207(F1), 57-68.

Grassie SL (1996). Models of track and train-track interaction at high frequencies: Results of benchmark test. Vehicle System Dynamics, 25, 243-262.

Knothe KL, Grassie SL (1993). Modelling of track and vehicle-track interaction at high frequencies. *Vehicle System Dynamics*, 22, 209-262.

Nielsen JCO (1993). Train Track Interaction: Coupling of Moving and Stationary Systems - Theoretical and Experimental Analysis of Track Structures Considering Wheel and Track Imperfections. *Ph.D. thesis*, Division of Solid Mechanics, Chalmers University of Technology, Gothenburg, Sweden.

Popp K, Schiehlen W (2003). System Dynamics and Long-Term Behavior of Track Vehicles, Track and Subgrade, Berlin.

Sato Y, Odaka T, Takai H (1988). Theoretical analyses on vibration of ballasted track. Quarterly Reports of Track Technical Reassuring Institute (Japan), 29(1), 30-32.



Seismic analysis of offshore wind turbine including fluid-structure-soil interaction

Kemal Hacıefendioğlu*, Fahri Birinci

Department of Civil Engineering, Ondokuz Mayıs University, 55139 Samsun, Turkey

ABSTRACT

This paper presents the seismic response analysis of offshore wind turbines subjected to multi-support seismic excitation by using a three dimensional numerical finite element model considering viscous boundaries. The sea water-offshore wind turbine-soil interaction system is modeled by the Lagrangian (displacement-based) fluid and solid-quadrilateral-isoparametric finite elements. The research conducts a parametric study to estimate the effects of different foundation soil types on the seismic behavior of the offshore wind turbine coupled interaction system. The results obtained for different cases are compared with each other.

ARTICLE INFO

Article history: Received 15 May 2015 Accepted 21 July 2015

Keywords:
Offshore wind turbine
Ice sheet
Fluid-structure interaction
Seismic analysis
Lagrangian approach

1. Introduction

In recent years, because of spending too much energy in the world, it needs additional energy. Therefore, the wind turbine industry has developed rapidly for sustainable energy production. In most regions of the world, wind turbines are built on the active earthquake zone. Therefore, in order to adequately design, operate, and maintain wind turbines, in particular, for sites with high peak ground acceleration, it seems necessary to take into account earthquakes.

Seismic analysis of wind turbine subjected to earth-quake ground motion has been studied and published by only a limited number of researchers. Bazeos et al. (2002) presented the load bearing capacity and the seismic behavior of a prototype steel tower for a 450 kW wind turbine with a horizontal power transmission axle. The structure was analyzed for static and seismic loads representing the effects of gravity, the operational and survival aerodynamic conditions, and possible site-dependent seismic motions by using the finite element method.

Witcher (2005) used an alternative approach to undertake the calculation of seismic response of wind turbine during earthquake ground motion by using the computer software. The software can be used to compute the

combined wind and earthquake loading of a wind turbine given a definition of the external conditions for an appropriate series of load cases. Maißer and Zhao (2006) investigated the dynamic responses of wind turbine towers to seismic excitations in time domain, considering soil structure interaction. The soil structure interaction was represented by a frequency-independent discrete parameter model approximately. The governing motion equations were derived by the application of Lagrange formalism including Lagrange multipliers.

The current research investigates the effects of different soil properties on the stochastic response of offshore wind turbine for random seismic excitation. All the numerical analyses are performed using computer program ANSYS (2003).

2. Lagrange Approach for Fluid Systems

The formulation of the fluid system is presented according to the Lagrangian approach (Wilson and Khalvati, 1983). In this approach, fluid is assumed to be linearly elastic and irrotational. Also, the fluid is assumed to be non-flowing and inviscid (that is, viscosity causes no dissipative effects). For this fluid, the relation between pressure and volumetric strain is given by

$$\begin{pmatrix}
P \\
P_x \\
P_y \\
P_z
\end{pmatrix} = \begin{bmatrix}
C_{11} & 0 & 0 & 0 \\
0 & C_{22} & 0 & 0 \\
0 & 0 & C_{33} & 0 \\
0 & 0 & 0 & C_{44}
\end{bmatrix} x \begin{pmatrix}
\varepsilon_v \\
W_x \\
W_y \\
W_z
\end{pmatrix},$$
(1)

where P, C_{11} and ε_v are the pressures which are equal to mean stresses, the bulk modulus and volumetric strains of fluid, respectively. In Eq. (1), P_x , P_y , P_z are the rotational stresses; C_{22} , C_{33} , C_{44} are the constraint parameters and w_x , w_y and w_z are the rotations about the Cartesian axis x, y and z, respectively.

In this study, the equations of motion of the fluid system are obtained using energy principles. Using the finite element approximation, the total strain energy of the fluid system may be written as,

$$\pi = \frac{1}{2} u_f^T K_f u_f \,, \tag{2}$$

where K_f and u_f are the stiffness matrix and the nodal displacement vector of fluid system, respectively. K_f is derived by summing stiffness matrices of the fluid elements as follows:

$$K_f = \sum K_f^e$$
 , $K_f^e = \int_{\mathcal{V}} B_f^{eT} C_f B_f^e dV^e$, (3)

where C_f is elasticity matrix consisting of diagonal terms in Eq. (1). B_f^e is strain-displacement matrix of the fluid element.

An important behavior of fluid systems is the ability to displace without a change in volume. The increase in the potential energy of the system due to the free surface motion can be written as,

$$\pi_s = \frac{1}{2} u_{sf}^T S_f u_{sf} , \qquad (4)$$

where u_{sf} and S_f are vertical nodal displacement vector and stiffness matrix of the free surface of the fluid system, respectively.

$$S_f = \sum S_f^e$$
 , $S_f^e = \rho_f g \int_A \overline{h}_s^T \overline{h}_s dA^e$, (5)

where \overline{h}_s is a vector consisting of interpolation functions of the free surface fluid element, ρ_f and g are mass density of the fluid and acceleration due to gravity, respectively.

Finally, the kinetic energy of the fluid system must be considered to complete the energy contributions. This energy is given by,

$$T = \frac{1}{2}\dot{u}_f^T M_f \dot{u}_f \,, \tag{6}$$

where M_f and \dot{u}_f are the mass matrix and the nodal velocity vector of the fluid system, respectively (Clough and Penzien, 1993). M_f is also obtained by summing the mass matrices of the fluid elements in the following:

$$M_f = \sum M_f^e$$
 , $M_f^e = \rho_f \int_V \overline{H}^T \overline{H} dV^e$, (7)

where \overline{H} is a matrix consisting of interpolation functions of the fluid element.

If Eqs. (2), (4) and (6) are substituted into Lagrange's equations, the equation of motion of the fluid system can be obtained as follows,

$$M_f \ddot{u}_f + K_f^* u_f = R_f \,, \tag{8}$$

where K_f^* , \ddot{u}_f , and R_f are system stiffness matrix including the free surface stiffness, nodal acceleration vector and nodal force vector, respectively (Bathe, 1996).

3. Stochastic Formulation

Since the formulation of the stochastic dynamic analysis of structural systems has been well known for many years, only the final equations will be given in this study. Detailed formulations for stochastic dynamic analysis are given in references (Lin, 1967; Yang, 1986; Manolis and Koliopoulas, 2001). One of the most important factors in stochastic analysis is the power spectral density function. If the power spectral density function of input process is known, the power spectral density function of output process can be determined easily. Filtered white noise model is generally used as power spectral density function for the modeling of ground motion simulation. Cross power spectral density function can be determined by using the equation of motion of the system under the ground motion as;

$$S_{ij}(\omega) = S_{iig}(\omega) \sum_{r=1}^{N} \sum_{s=1}^{N} \psi_{ir} \psi_{js} H_{ir}(\omega) H_{js}^{*}(\omega), \qquad (9)$$

where $S_{iig}(\omega)$ represents the power spectral density function of ground motion, ω represents the frequency, $H(\omega)$ represents the frequency response function, N is the number of modes which are considered to contribute to the response, ψ_{ir} is the contribution of the rth mode to $u_i(t)$ displacement and * denotes the complex conjugate. For i=j, Eq. (9) gives the power spectral density function of the ith displacement.

4. Ground Motion Model

Ground motions are known to highly nonstationary in nature (both in amplitude and frequency content) and this has a huge impact on the stochastic response. Since the primary objective of this study is to perform a parametrical study with the ice cover effects on the response of offshore wind turbine subjected to stochastic seismic excitation, the non-stationary ground motion is not considered.

The power spectral density function of ground acceleration for stationary ground motion is assumed to be of the form of filtered white noise ground motion model originally proposed by Kanai (1957)–Tajimi (1960) and modified by Clough and Penzien (1993),

$$S_{\ddot{u}_g}(\omega) = S_0 \left(\frac{\omega_g^4 + 4\xi_g^2 \omega_g^2 \omega^2}{(\omega_g^4 - \omega^2)^2 + 4\xi_g^2 \omega_g^2 \omega^2} \right) \cdot \left(\frac{\omega^4}{(\omega_f^4 - \omega^2)^2 + 4\xi_f^2 \omega_f^2 \omega^2} \right), \quad (10)$$

where, ω_g and ξ_g are the resonant frequency and damping ratio of the first filter; ω_f and ξ_f are those of the second filter; and S_0 is the spectrum of the white-noise bedrock acceleration.

Power spectral density function of the Kocaeli earthquake for firm soil type is shown in Fig. 1. The calculated intensity parameter value for firm soil type is, S_0 (firm)=0.00103 m²/s³. Filter parameter values (ω_g , ξ_g , ω_f , ξ_f) proposed by Der Kiureghian and Nevenhofer (1991) are utilized as ω_g =15.0 rad/s, ξ_g =0.6, ω_f =1.5 rad/s, and ξ_f =0.6.

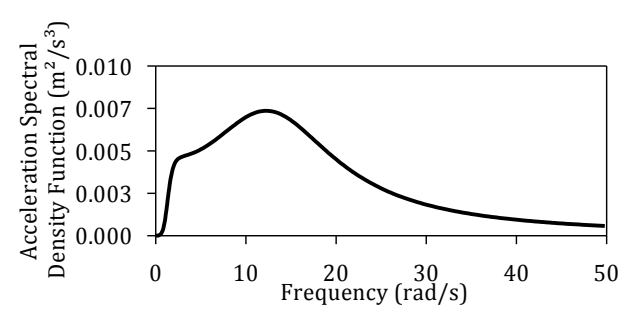


Fig. 1. Power spectral density function for the Kocaeli earthquake.

5. Application

The offshore wind turbine, water in the sea and soil was assumed to behave linear elastic, isotropic and homogeneous. Therefore, a non-linear phenomenon such as water cavitation was not included in the study. To evaluate the stochastic response of the coupled system, the material properties of the wind turbine body, sea water and soil media used in the analyses are given in Table 1. In addition, the average thicknesses of the wind turbine are shown in Fig. 2. The mass of the nacelle was taken into account as 130,000 kg.

Table 1. Material properties of considered coupled system.

Material	Elasticity Modulus (kN/m²)	Poisson's Ratio	Mass per unit Vol. (kg/m³)
Turbine	2.06x10 ⁷	0.30	7800
Soil type (S1)	2.00x10 ⁶	0.30	2000
Soil type (S2)	3.00x10 ⁵	0.35	1900
Soil type (S3)	5.00x10 ⁴	0.40	1800
Sea water	2.07x10 ⁶	-	1000

In this research, the stochastic responses of the fluid-structure-soil interaction system of the offshore wind turbine are estimated by using a three dimensional finite element model based on Lagrangian approach (Fig. 3). In the Lagrangian approach, displacements are selected as the variables in both fluid and structure domains (Calayır et al., 1996; Olson et al., 1983). The formulation of the fluid system is presented according to the Lagrangian approach (Wilson and Khalvati, 1983). In this approach, fluid is assumed to be linearly elastic, inviscid

and irrotational. The soil media is represented by solid elements; the wind tower and sea water are represented by shell and fluid elements in the finite element model, respectively. While SHELL63 element is used to model the wind turbine, soil media is modeled using SOLID45 elements; FLUID80 element is used to model the sea water media. At the sea water-wind turbine and sea water-soil, the length of the coupling element is chosen as 0.001 m. The main objective of the couplings is to hold equal the displacements between two reciprocal nodes. In this study, viscous boundary method developed by Lysmer and Kuhlemeyer (1969) is considered in three dimensions. These viscous boundaries can be used with the finite element mesh as shown in Fig. 3.

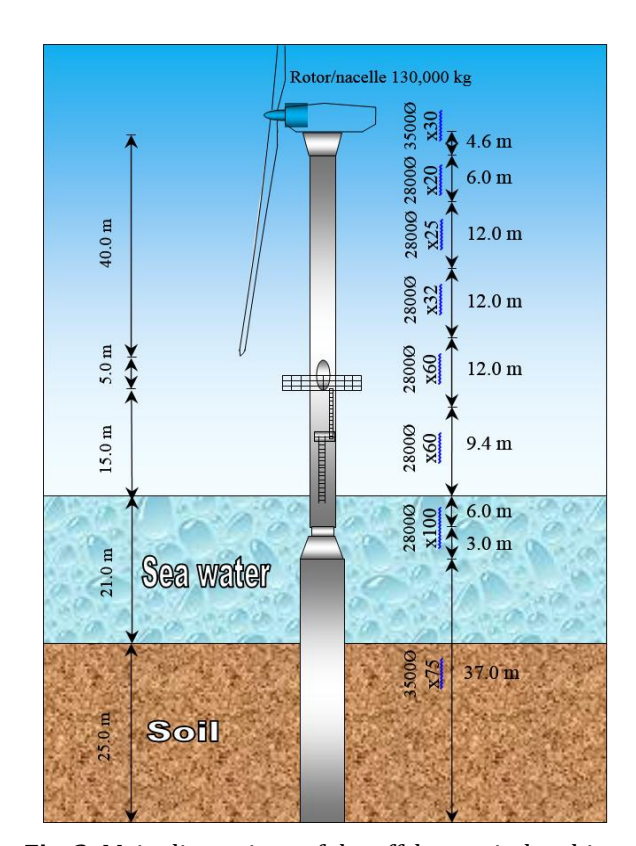


Fig. 2. Main dimensions of the offshore wind turbine.

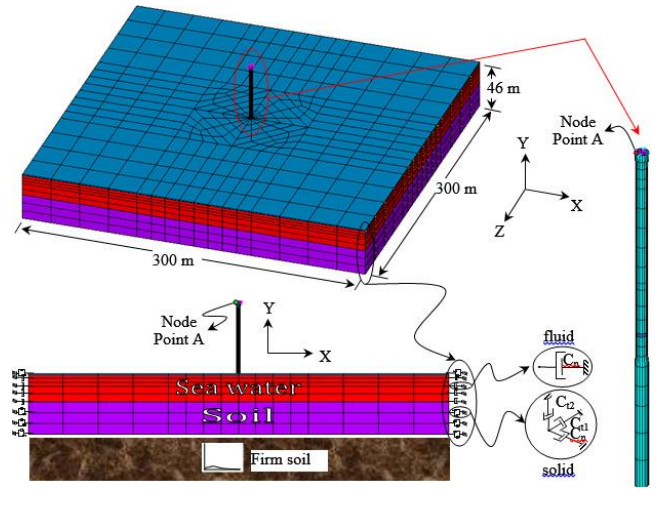


Fig. 3. Finite element model of the sea water-wind turbine-soil interaction system for different soil conditions.

6. Results

The effects of the foundation soil properties on the stochastic response of the offshore wind turbine are illustrated in Figs. 4-5 by using three soil types (Table 1). In this section, all the support site conditions have firm soil (FF). For this purpose, the displacement power spectral density (PSD) values for these soil types, at point A, depending on the frequency ranging from 0.0 to 1.4 Hz, is shown in Fig. 4. It is concluded from the figure that the displacement values increase as the soil gets softer. The same comments can be made for the one standard deviation (1 σ) of the Von Misses stress responses (N/m²) due to the different soil types on the offshore wind turbine as illustrated in Fig. 5. The maximum stresses for S1 and S3 soil types occur in the same regions on the offshore wind turbine. Whereas the maximum stress values due to S2 soil type occur in the different region on the offshore wind turbine.

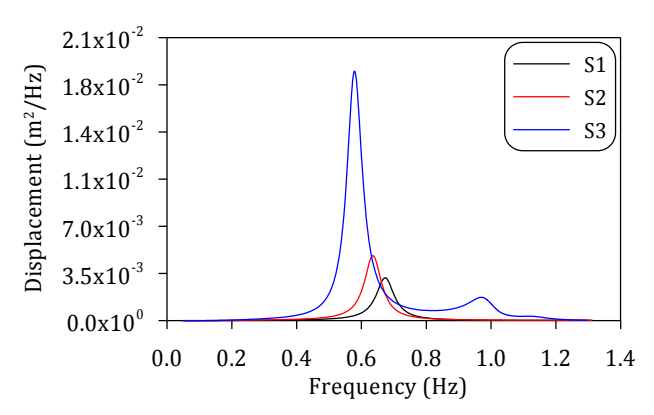


Fig. 4. The displacement power spectral density values at point A for the different soil types.

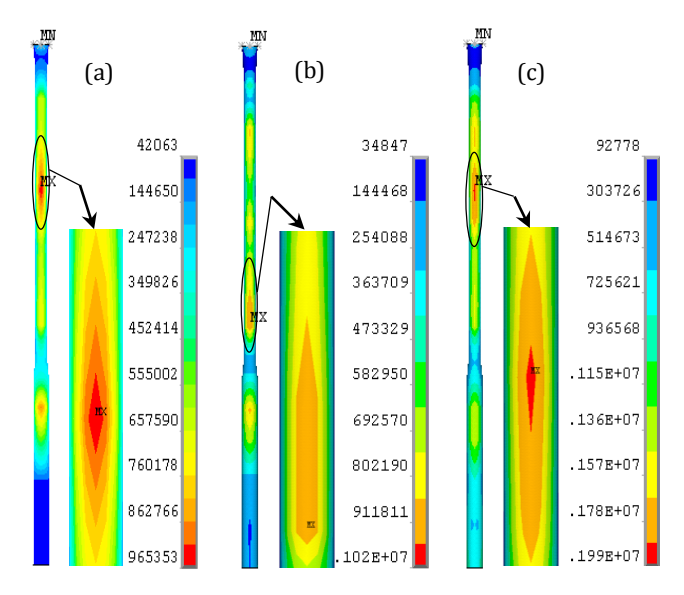


Fig. 5. 1σ Von Misses stress contours for (a) S1, (b) S2 and S3 soil types.

7. Conclusions

This study investigates the stochastic response of an offshore wind turbine under the random seismic excitation. The parametric analyses were carried out by considering the structure-sea water-soil interaction. The results for the coupled interaction finite element system have been modeled by using the computer software called ANSYS.

The stochastic response of the offshore wind turbine including the structure-sea water-soil interaction during random seismic excitation is considerably affected by the different foundation soil properties. The results show that the values of the stochastic response of the coupled system increases as soil gets softer.

REFERENCES

ANSYS (2003). Swanson Analysis System, USA.

Bathe KJ (1996). Finite Element Procedures in Engineering Analysis. Prentice-Hall Inc., Englewood Cliffs, NJ.

Bazeos N, Hatzigeorgiou GD, Hondros ID, Karamaneas H, Karabalis DL, Beskos DE (2002). Static seismic and stability analyses of a prototype wind turbine steel tower. *Engineering structures*, 24(8), 1015-1025.

Calayır Y, Dumanoğlu AA, Bayraktar A (1996). Earthquake analysis of gravity dam–reservoir systems using the Eulerian and Lagrangian approaches. *Computer and* Structures, 59(5), 877–90.

Clough RW, Penzien J (1993). Dynamics of Structures. 2nd edition, McGraw-Hill, Singapore.

Der Kiureghian A, Neuenhofer A (1991). A response spectrum method for multiple-support seismic excitations. Report No. UCB/EERC-91/08, Berkeley (CA): Earthquake Engineering Research Center, College of Engineering, University of California, California.

Kanai K (1957). Semi-empirical formula for the seismic characteristics of the ground. Bulletin of the Earthquake Research Institute, 35, 307-325.

Lin YK (1967). Probabilistic Theory of Structural Dynamics. McGraw Hill. New York.

Lysmer J, Kuhlemeyer RL (1969). Finite dynamic model for infinite media. ASCE Journal of the Engineering Mechanics Division, 95, 859-877.

Maißer P, Zhao X (2006). Seismic response analysis of wind turbine towers including soil-structure interaction. Proceedings of the Institution of Mechanical Engineers, Part K, Journal of Multi-body Dynamics. 220(1), 53-61.

Manolis GD, Koliopoulos PK (2001). Stochastic Structural Dynamics in Earthquake Engineering. WIT Press, Southampton.

Olson LG, Bathe KJ (1983). A study of displacement-based fluid finite elements for calculating frequencies of fluid and fluid-structure systems. *Nuclear Engineering and Design*, 76(2), 137–51.

Tajimi H (1960). A statistical method for determining the maximum response of a building structure during an earthquake. *Proceedings* 2nd World Conference Earthquake Engineering, Tokyo and Kyoto, Japan.

Wilson EL, Khalvati M (1983). Finite elements for the dynamic analysis of fluid-solid systems. *International Journal for Numerical Methods in Engineering*, 19(11), 1657-1668.

Witcher D (2005). Seismic analysis of wind turbines in the time domain. Wind Energy, 8(1), 81-91.

Yang CY (1986). Random Vibration of Structures. John Wiley and Sons Inc., New York.



Effects of shape factor on the behaviour of elastomeric roadway bridge bearings and benefits of circular bearing cross section

Niyazi Özgür Bezgin*

Deparment of Civil Engineering, İstanbul University, 34320 İstanbul, Turkey

ABSTRACT

Elastomeric bearings can support steel and concrete bridge girders. Layered bearings with steel plates are typical and they provide the lateral flexibility to accommodate longitudinal girder movement and the necessary vertical stiffness to vertical support reactions. Elastomeric bearings also replace existing roadway bridge girder supports. Mechanical behaviour of elastomeric bearings strongly relates to the incompressible character of the elastomer material. Incompressible character of elastomers, allows elastomer-bearing design through confining unbound surfaces and limiting surface deformations. A particular character of elastomeric bearings known as the shape factor (*S*) represents the difference in stiffness of two elastomeric bearings that have same cross sectional areas but different cross sectional shapes. Through an advanced finite element-modeling program, this study evaluates and compares the behaviours of rectangular and circular steel layered elastomeric bridge bearings under the application of vertical and lateral loads.

ARTICLE INFO

Article history:
Received 2 September 2015
Accepted 30 October 2015

Keywords: Roadway bridges Elastomers Bridge bearings Shape factor Skew

1. Introduction

Elastomeric bridge bearings are in use since 1960's. Square, rectangular or circular bearings come in different cross-sectional areas, thicknesses and with different number of layers of steel or composite plates.

They accommodate the required longitudinal motion for bridge girders due to temperature dependent elongations and contractions. They also accommodate the necessary rotation at the supports due to bending and maintain the required bearing stress on the element supporting the girder. Therefore, correct positioning of the bearings with respect to the longitudinal axis of the girder is an important application issue. Curved girders and skewed bridge girders necessitate extra care in rectangular bearing positioning on the supporting pier for correctly aligning the principal bending axis of the bearings with the expected rotation and the expected longitudinal movement at the girder support. Unlike circular bearings that have the same rotational inertia around any central axis, the rotational inertia of square and

rectangular bearing varies, being at their limits around their principal axis.

A conducted survey in 2001 among the transportation departments of the states in the USA, collected information about the use of elastomeric bridge bearing types and the experienced difficulties in the field with respect to the use of square and rectangular bearings. One of the stated problems was lateral movement of square and rectangular bearings in unexpected directions other than their principal axis. Another stated problem was delayering of the composite square and rectangular bearing. The final stated problem was crushing of elastomeric material due to bearing rotation around axis other than their principal axis. Table 1 shows responses from states that use circular elastomeric bearings. Fig. 1 shows an application case of circular elastomeric bearing.

Due to alignment difficulties of square and rectangular bearings on the piers in the field, use of circular bearings is increasing. This study analytically evaluates and compares the behaviours of bearings under vertical and lateral loads in terms of displacement and stress distributions.

State	Diameter (cm)	Thickness (cm)	Type of elastomer	Type of bridge
Connecticut	60	5 - 7.5	Neoprene	Medium and high skew; 30 – 45 m span
Idaho	30 - 60	Not stated	Neoprene	High skew
Maine	30 - 60	2.5 - 10	Neoprene	High skew or curved, spans smaller than 30 m
Massachusetts	30 - 60	7.5 – 7.5	Polychloroprene	High skew or curved, spans smaller than 30 m
New Hampshire	30 - 90	5 – 10	Natural rubber	High skew or curved, spans smaller than 30 m
New York	30 - 60	Not stated	Neoprene and natural rubber	High skew or curved
Texas	30 - 60	2.5 - 7.5	Neoprene and	High skew or curved, bridges shorter than 45 m

Table 1. States declaring circular elastomeric bridge bearing use in 2001 (Najm et al., 2002).



Fig. 1. Use of circular elastomeric bridge bearing (Najm et al., 2002).

2. Elastomers

Elastomers are polymeric materials composed of carbon and hydrogen atoms and filler elements. Through a process known as vulcanization, bonds form between the polymeric chains through sulfur atoms thereby preventing relative slip between the polymeric chains and providing elasticity to the elastomeric element under loads.

Deformation characteristics of the polymeric material are dependent on ambient temperature. Ductility and the elasticity of the material diminish with reduced temperatures and the material becomes brittle. In order to categorize the polymeric material as an elastomer, the polymeric chains must preserve their ductility and elasticity.

Elastomers differ from other solid elements with their incompressible quality. In other words, the incompressible material cannot collapse onto itself under compression and always maintains its volumetric stability and density. Under the application of load, the elastomer body deforms through its unbound surfaces. Through its

incompressible character, it is possible to change the stiffness of an elastomeric element by bounding and limiting its deformation through its free surfaces. On the other hand, elastomeric elements with the same cross sectional area but different cross sectional shapes have different unbound deformable surface areas. Because of this difference, a unique property known as the shape factor (*S*) develops, which affects the deformation value of the elastomeric bearing element under loads.

3. Shape Factor

Shape factor is the ratio of element cross section to the freely deformable surface area of the element. Fig. 2 shows a square elastomer with thickness (t) and side distance (a) under the application of a force (P). The cross section area effective in resisting this force is a^2 and the free surface area deforming because of this force is $4 \cdot a \cdot t$. The shape factor of this section is therefore $S = a^2/4at = a/4t$.

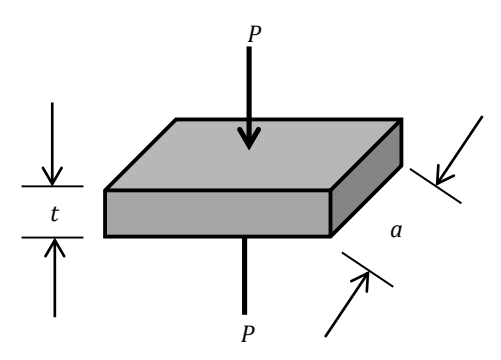


Fig. 2. A square elastomer bearing under load P.

Performing the same deduction for a circular elastomeric bearing with a diameter (D) and a thickness (t), one determines the shape factor as: $S = (\pi D^2/4) / (\pi D \cdot t) = D/4t$.

Effect of the geometric shape on the shape factor becomes apparent when the perimeters of a square and circular elastomeric bearing with the same cross section area (A) are compared. From Eqs. (1) and (2), the perimeter of a circle is 88.6% of the perimeter of a square with the same area. This finding agrees with the geometric definition of a circle, which states that a circle is the curve of a given length that encloses the greatest area (Falconer, 2013).

Area of a circle = Area of a square
$$\rightarrow$$

$$a^2 = \pi D^2/_4 \rightarrow a = \frac{D\sqrt{\pi}}{2}, \qquad (1)$$

Perimeter of a circle/ $_{Perimeter\ of\ a\ square} = \frac{\pi D}{4a} = \frac{\pi D}{2D\sqrt{\pi}} = 0.886$. (2)

This geometric difference provides the shape factor of an elastomeric element. Eq. (3) qualitatively states the shape factor.

Shape factor =
$$\frac{Loaded\ area}{Deformable\ area} = \frac{Loaded\ area}{Perimeter\ \times Thickness}$$
 (3)

The thickness (t) term represents the smallest thickness representing the free deformable surface of the elastomeric bearing element. The thickness values of the unlayered and layered elastomeric bearing presented in Fig. 3 are different. Because of this difference, the shape factors of the two bearings are also different. Primary benefit of layering is to confine the freely deformable surfaces and limit the deformations to increase the stiffness. Theoretically, the stiffness of a fully confined elastomeric element would be infinite since the material is incompressible.

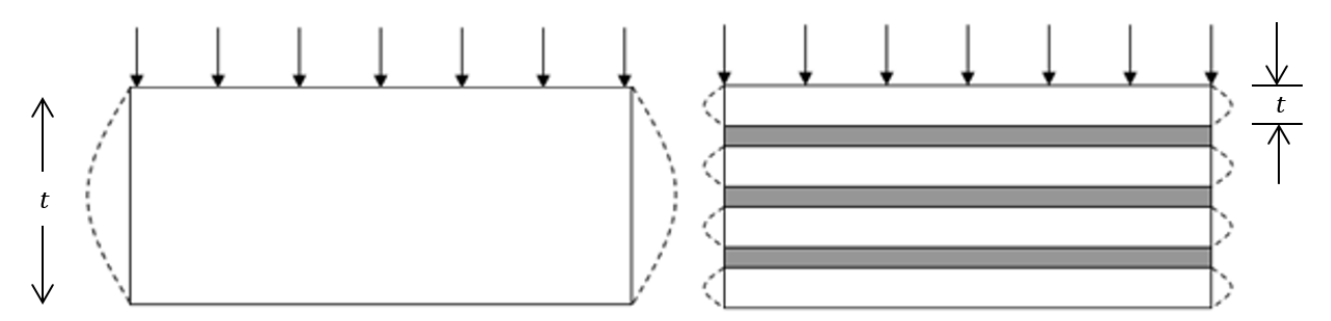


Fig. 3. Unlayered and layered elastomeric bearings with plates (Bezgin, 2002).

Eqs. (4), (5) and (6) develop and compare the shape factors of a square and circular bearing with the same cross sectional area. The perimeter of a circle relates to that of a square with the finding in Eq. (2).

$$S_{square} = \frac{Area\ of\ square}{Perimeter\ of\ square \times Thickness},\tag{4}$$

$$S_{circular} = \frac{Area\ of\ circular}{0.886 \times Perimeter\ of\ square \times Thickness}, \quad (5)$$

$$S_{circular}/S_{square} = 1/0.886 = 1.13.$$
 (6)

The difference in the perimeters reflects on to the area of freely deformable surfaces and thus the shape factors of the two geometries.

The modulus of elasticity (E) of elastomers relates to the shear modulus (G), hardness (k) and the shape factor (S) as shown in Eq. (7) that has also been used by AASHTO (Bezgin, 2002; Fediuc et al., 2013).

$$E = 3 \cdot G \cdot (1 + 2 \cdot k \cdot S^2). \tag{7}$$

Other such equations presented in literature (Bauman, 2008; Fediuc et al., 2013) show the direct relationship between elasticity modulus (*E*) and the shape factor (*S*). Thus, the shape factor is an influential parameter on the stiffness of an elastomeric bearing.

4. Layered Elastomers

In order to increase the stiffness of elastomeric bridge bearings and maintain the lateral flexibility, steel or composite plates strengthen bearings. Fig. 4 shows the variation of shear modulus of Shore-A 55 hardness neoprene elastomer with temperature used within the finite element models presented in this section. The finite element models developed for the steel-layered neoprene bearings have plates with 240 MPa yield strength. The analysis conditions are set at -10°C and the corresponding shear modulus of the elastomer at 1150 kPa.

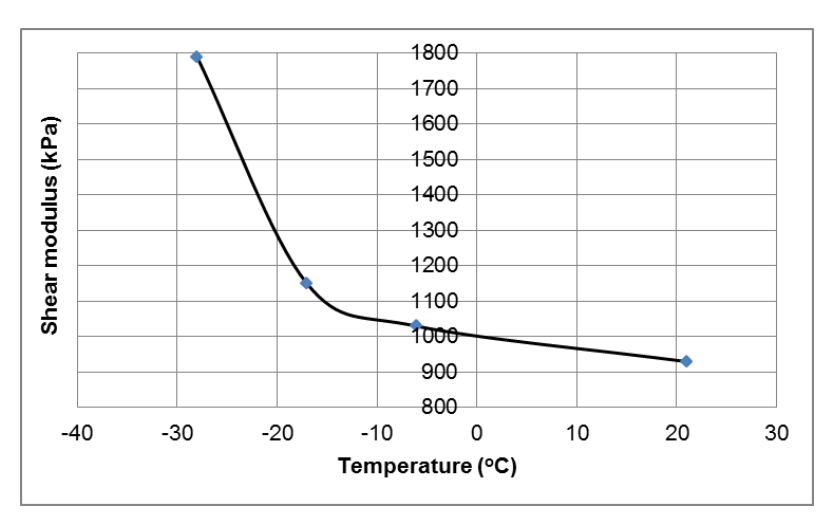


Fig. 4. Variation of shear modulus with temperature (Bezgin, 2002).

Thicknesses of the 3-layered, 5-layered and 7-layered square and circular bearings shown in Fig. 5 are 4.5 cm, 7.6 cm and 10.7 cm respectively. The length and the width of the square bearing is 40.6 cm and the diameter of the circular bearing is 45.8 cm. The bearings are analyzed under the action of 1150 kN vertical force through

a rigid plate, generating 7 MPa compressive stress in the bearings.

The elastomeric layer thicknesses are 13.5 mm. Table 2 and Fig. 6 present the shortening values of the analyzed bearings. Eqs. (8) and (9) show the shape factors of the square and circular bearings.

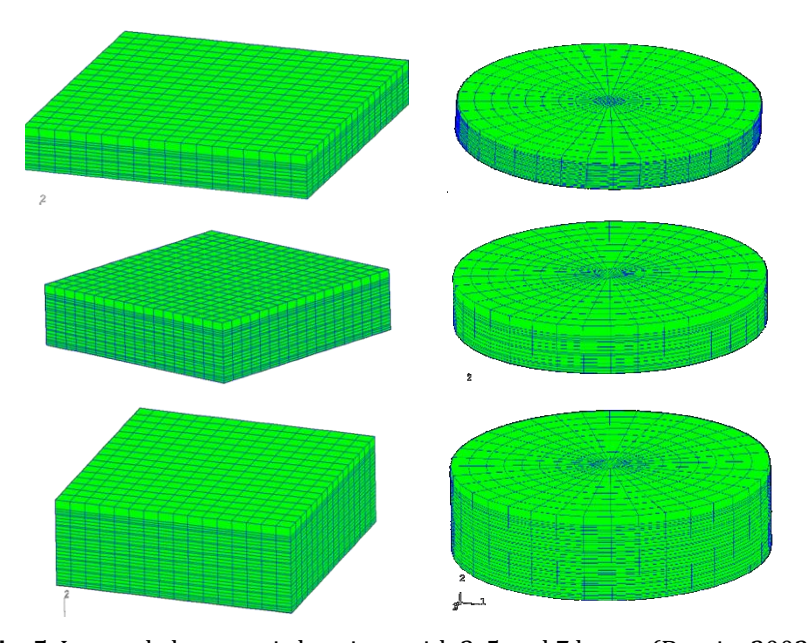


Fig. 5. Layered elastomeric bearings with 3, 5 and 7 layers (Bezgin, 2002).

$$S_{square} = \frac{40.6^2}{4 \cdot 40.6 \cdot 1.35} = 7.5,$$
 (8)

$$S_{circular} = {\pi \cdot 45.8^2 / 4} / {\pi \cdot 45.8 \cdot 1.35} = 8.5.$$
 (9)

Due to higher shape factor of the circular bearing, the contraction values are approximately 10% lower than the values obtained for the square bearing.

5. Elastomer Behaviour under Lateral Loads

Bridge girders longitudinally move to accommodate the elongations and contractions due to temperature differences. The bearings are also bent by the rotations at the ends of the girders they support. Determination of the direction and the axis of these movements and proper alignment of the bearings with respect to the expected movements is an important on-site matter due to its effects on the internal stress values and internal stress distributions within the elastomer. The primary rotational axis of a circular section is any axis that passes through its geometric center. However, rotational inertia values of square and rectangular shapes depend on the particular axis that pass through the geometric centers of the square and rectangular shapes. Therefore, if the square and rectangular shapes are so placed that they are bent under the deflecting girder they support around

an axis that is not primary, unexpected stress values and distributions may arise. On the other hand, if the expected lateral movement is not aligned perpendicular to the primary rotational axis, the resulting stress distribution pattern can also have discontinuities of concentrations.

Table 2. Shortening values determined under the application of 7 MPa compressive stress (Bezgin, 2002).

		Shortening (mm)		
Number of layers	Bearing thickness (cm)	Square	Circular	
3	4.6	0.34	0.31	
5	7.6	0.65	0.59	
7	10.7	0.86	0.80	

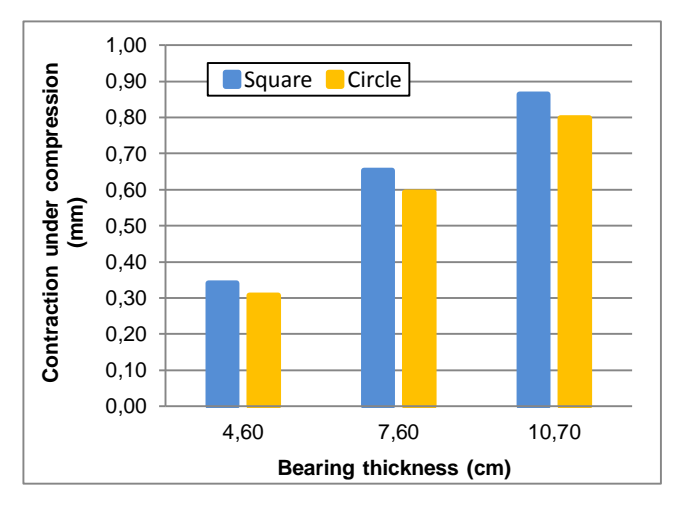


Fig. 6. Contraction values of square and circular bearings (Bezgin, 2002).

Figs. 7 and 8 show laterally deformed bearings under the action of 1150 kN vertical and 230 kN lateral forces going through the center of the bearings. The bearings are 7.6 cm thick and composed of 5-steel layers. All the bearings have an area of 1648 cm². The size of the square bearing is 40.6 cm by 40.6 cm and the circular bearing diameter is 45.8 cm. The lateral load is applied diagonally to the square bearing.

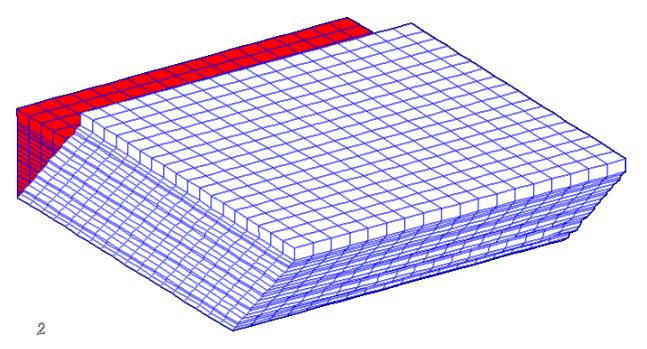


Fig. 7. Square bearing under diagonally applied lateral load (Bezgin, 2002).

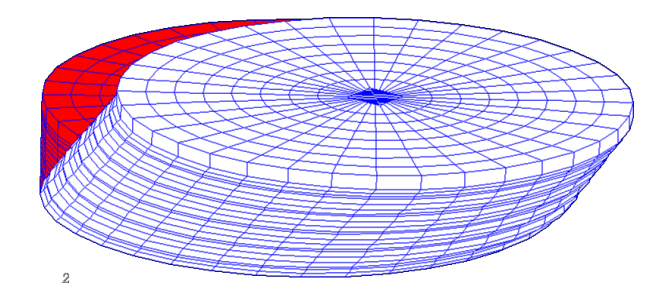


Fig. 8. Circular bearing under lateral load (Bezgin, 2002).

The lateral displacement of the bearings is 6.7 cm. Fig. 9 shows the vertical stress distribution in the elastomer layers of the bearings where the stress discontinuities and concentrations in the square bearing become apparent.

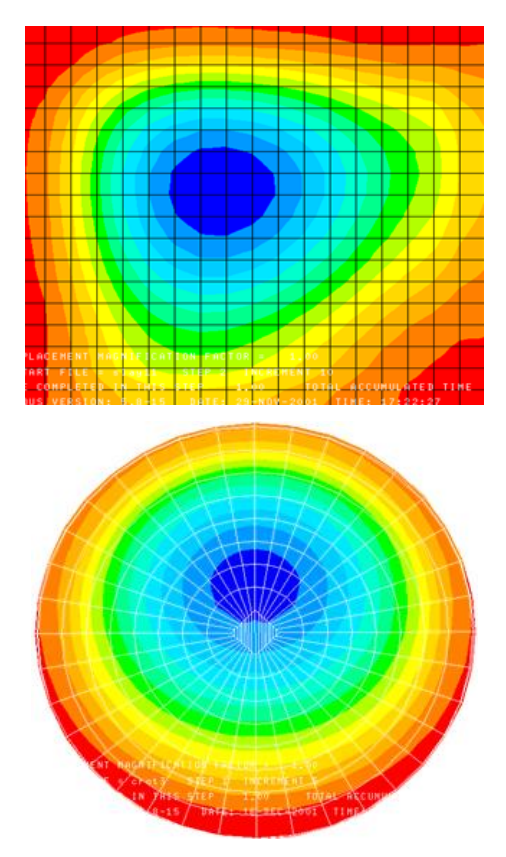


Fig. 9. Distribution of vertical stresses in bearings under lateral loads (Bezgin, 2002).

6. Conclusions

Cross sectional geometry affects the structural behaviour of elastomeric bearings. The shape factor represents this effect and it relates to the incompressibility of the elastomer and therefore relates to the influence of the freely deformable surface area on the bearing behaviour. The stiffness of elastomeric bearings can change by modifying the freely deformable surface area. This analytical study showed that circular bearings provide 10% higher stiffness than square bearings with the same area. The study also showed that distribution of interlayer vertical stresses under lateral loads is uniform in circular bearings compared to square bearings.

REFERENCES

- Bauman JT (2008). Fatigue, Stress and Strain of Rubber Components Guide for Design Engineer. Hanser, Munich.
- Bezgin NÖ (2002). Geometric Effects on the Behavior of Elastomeric Bridge Bearings. *M.Sc. thesis*, Rutgers, The State University of New Jersey, UK.
- Falconer K (2013). Fractals: A Very Short Introduction. Oxford University Press, Oxford.
- Fediuc OD, Budescu M, Fediuc V, Venghiac VM (2013). Compression modulus of elastomers. *Buletinul Institutului Politehnic din Iași*, LIX (LXIII), f.2.
- Najm H, Nassif H, Bezgin NÖ (2002). Circular Elastomeric Bearings. *Technical Report, FHWA-NJ-2002-005*.